PADÉ APPROXIMANTS TECHNIQUE FOR THE ANALYSIS OF WAVEGUIDE JUNCTIONS AND BEAM SPLITTERS

By

MOHAMMED AMEERUDDIN

A Thesis Presented To The

DEANSHIP OF GRADUATE STUDIES

In Partial Fulfillment Of The Requirements
For The Degree

MASTER OF SCIENCE

IN

ELECTRICAL ENGINEERING

KING FAHD UNIVERSITY
OF PETROLEUM & MINERALS

May 2004

KING FAHD UNIVERSITY OF PETROLEUM & MINERALS
DHAHRAN 31261, SAUDI ARABIA

DEANSHIP OF GRADUATE STUDIES

This thesis, written by **MOHAMMED AMEERUDDIN** under the direction of his thesis advisor and approved by his thesis committee, has been presented to and accepted by Dean of Graduate Studies, in partial fulfillment of the requirements for the degree of

MASTER OF SCIENCE IN <u>ELECTRICAL ENGINEERING</u>.

<u>Thesis Committee</u>

_____
Dr. Hussain Ali Al-Jamid
(Thesis Advisor)

_____
Dr. Husain M. Masoudi
(Member)

_____
Dr. Mohammad A. Al-Sunaidi
(Member)

_____
Dr. Jamil M. Bakhashwain
(Department Chairman)

_____
Dr. Mohammad A. Al-Ohali
(Dean of Graduate Studies)

_____
May 2004

Dedicated to Pappa, ammi, my brother and sisters.

ACKNOWLEDGEMENTS

At the outset, I thank Almighty ALLAH for His innumerable blessings which indeed are helping me in the course of my life. Acknowledgement is due to the King Fahd University of Petroleum and Minerals for all the support and facilities provided for my M.S. and this thesis work.

I am extremely obliged to my advisor, Dr. Hussain A. Al-Jamid, for guiding and supporting me throughout this thesis work. I thank him for being so patient and tolerant with me, and more importantly for being like a friend to me. I also would like to thank him for his strenuous efforts in refining this thesis work.

I am thankful to my committee members Dr. Husain M. Masoudi and Dr. Mohammad A. Al-Sunaidi for their encouragement and appreciation. Their comments and positive feedback helped me improve my thesis.

I am grateful to my father, mother, brother and sisters, for their unconditional support and sacrifice, which helped me achieve this mark. I am thankful to all my family members and especially my grandmother for being very affectionate to me.

Contents

LIST OF TABLES

LIST OF FIGURES

xi

THESIS ABSTRACT

Name: MOHAMMED AMEERUDDIN

Title: PADÉ APPROXIMANTS TECHNIQUE FOR THE ANALYSIS OF WAVEGUIDE JUNCTIONS AND BEAM SPLITTERS

Major Field: ELECTRICAL ENGINEERING

Date of Degree: MAY 2004

ABSTRACT

In this thesis work, the Method of Lines (MOL) *which is based on eigenpair calculation is modified using Padé approximants* $(PBPM)$. *Because the use of Padé approximants decreases the numerical demand of the* MOL *from* N^3 *to* N, *where* N *is the number of discretizations, the* $PBPM$ *is far more efficient than the* MOL. *Various numerical experiments which are reported in this thesis work confirm that the* $PBPM$ *is much more efficient than the* MOL *when the number of transverse mesh points is large. The* $PBPM$ *has been applied in the analysis of a variety of integrated optical devices. This includes a beam expander, which connects two waveguides of different core widths, using a linearly tapered junction. In addition, a waveguide crossing with a resonant cavity at the center has been studied. Finally a novel three-way* 90^0 *beam splitter is proposed and its operation has been verified using the developed* $PBPM$ *approach. This type of beam splitter utilizes a rectangular cavity at the center.*

ملخص الرسال

الاســـــــم: محمد أمير الدين

عنوان الرسالة: طريقة تقريبات باديه واستخداماها في تحليل تقاطعات قائد الموجة و مقسمات الحزم الضوئية

التخصـــــص: هندسة كهربائية

تاريخ التخـرج: مايو 2004م

الملخص:

في هذه الرسالة تم تغيير طريقة الخطوط وذلك بإدخال تقريبات باديه عليها. إن استخدام تقريبات باديه تقلل من الجهد الحسابي للحاسوب حيث يتناسب هذا الجهد مع ن (عدد النقاط المستعملة في الحل) بدلاً من تناسبه مع مكعب ن قبل استخدام تقريبات باديه على طريقة الخطوط. وتوجد العديد من التجارب الحسابية في هذه الرسالة والتي تؤكد بأن الطريقة المتبعة في هذه الرسالة أكثر فعالية بكثير من الطريقة المستخدمة من قبل. وقد استخدمت طريقة الحساب الجديدة والمبنية على تقريبات باديه لدراسة وتحليل أنواع عديدة من الدوائر الضوئية المدمجة، مثل دائرة توسيع الشعاع والتي تكون حلقة وصل بين موجها موجة ذا عرضين مختلفين. كما تمت دراسة منطقة التقاطع بين موجها موجة متعامدان، حيث تحتوي هذه المنطقة على فجوة رنين في وسطها. وأخيراً تمت دراسة قاسم جديد أشعة ثلاثي الحزم ذا أقسام متعامدة وقد تمت محاكاة عمل هذا القاسم باستخدام طريقة الحساب الجديدة، مع العلم بأن هذا القاسم الجديد يعتمد على استخدام فجوة رنين مستطيلة الشكل والتي توجد في مركز القاسم.

CHAPTER 1

INTRODUCTION

1.1. INTEGRATED OPTICS

Integrated optics or *integrated photonics* [1-5] is a branch of optics that combines various technologies such as electro-optics, non-linear optics, opto-electronics waveguide technology etc. In 1969 S.E. Miller [2], introduced the term "integrated optics" which emphasized the similarity between the planar optical circuits technology and the integrated micro-electronic circuits technology. His idea was to fabricate integrated optical circuits in which various optical elements, passive as well as active, were integrated in a single substrate, combining and interconnecting them via small optical transmission lines called optical waveguides. Thus, resulting in devices which are compact and low weight, robust, faster operational capability, stability with regards to alignment, high optical power density and low cost.

When the refractive index contrast between the waveguide core and the outside regions is high, the waveguide core can be made sufficiently small while maintaining strong confinement of the field. This leads to the concept of the so called photonic wire, which results in improved utilization of space in integrated optical circuits, leading potentially to high density integrated optics.

1

Also, because of the strong light confinement in high contrast optical waveguides, new and interesting device operations are possible, which do not exist in low contrast waveguides.

1.2. PROPOSED THESIS WORK

In this thesis work, we will consider only high index contrast waveguides and study various *IO* structures based on them. This includes a waveguide junction between two waveguides of different core widths. This type of junction is termed beam expander. In addition, we will analyze a waveguide junction in which two waveguides cross each other at a 90^0 angle. In reality, this later case can give rise to a multitude of possibilities. We will consider two of those possibilities. The first is when the junction is designed to prevent optical power from leaking from one waveguide into the other leading to minimum cross-talk and the bulk of optical power remaining in the same waveguide. In this thesis, this type of junction is termed as waveguide crossing. The second possibility considered in this thesis is when the junction is designed as a 90^0 three-way beam splitter. In this later case, we are interested in controlling the amount of optical power that is channeled into the various arms of this 90^0 three-way beam splitter. For simplicity this type of junction will be termed as a beam splitter.

Thus in summary, our purpose is to analyze a simple waveguide junction, a waveguide crossing and a beam splitter.

1.3. CALCULATION METHOD

In general, analytical solutions of the electromagnetic field in IO structures are not available which makes numerical methods indispensable for analysis of these structures. Various numerical tools are available for this purpose, which includes the Method of Lines (MOL) [6-23], the finite-difference time-domain method $(FDTD)$ [24-28], the finite-element method (FEM) [29-32], and the beam propagation method (BPM) [33-45].

In this thesis work, we will utilize the MOL for the analysis of the proposed structures. However, the MOL relies on the calculation of the eigenvalues and eigenvectors (eigenpairs) of the system matrix. Although the MOL is accurate, it is very demanding numerically when the matrix dimension exceeds few hundreds in value. In this thesis work, therefore, the computation of the eigenpairs will be avoided. Instead, we will incorporate Padé approximants in the Method of Lines $(PMOL)$ in order to enhance the CPU memory and time requirements. Due to the similarities in the formulation of the $PMOL$ and the Matrix formulation of BPM with Padé approximants, $PMOL$ will be referred to as $PBPM$ so as to credit the initial work done in the BPM Framework.

1.4. THESIS ORGANIZATION

The thesis work is organized in seven chapters. The first chapter is an introductory which includes introduction to integrated optics. The second chapter introduces the basic Method of Lines and describes how the eigenpairs are utilized in the field calculations. The third chapter introduces Padé approximants with sufficient details. This chapter also contains a general procedure for deriving Padé primes for arbitrary functions. It also discusses a general iterative approach for analyzing multiple longitudinal discontinuities in planar waveguide structures. Chapters four, five and six are dedicated respectively to the analysis of the beam expander, the waveguide crossing, and the three-way beam splitter mentioned earlier. The final chapter (chapter 7) concludes this thesis work.

CHAPTER 2

METHOD OF LINES

2.1.   INTRODUCTION

The Method of Lines (*MOL*) [6-23] is a semi analytical technique for solving partial differential equations (*PDE*). The *PDE* is transformed into an ordinary differential equation (*ODE*) by discretizing all the independent variables except one. If there are n independent variables then $(n-1)$ variables are discretized resulting in an *ODE* which can then be solved analytically in terms of the remaining variable [46]. The *MOL* has been applied to several types of planar longitudinally uniform optical and microwave waveguide problems. It has been used to analyze single [47] and multiple discontinuities in optical waveguides [7, 48] and to solve non-linear waveguide problems [9] as well as diffraction problems from waveguide ends [8]. It has been successfully used to model $3-D$ problems [14-16] for both optical and microwave waveguides. This procedure guarantees a high numerical precision and an acceptable computational expense [6]. However, the *MOL* relies on the computation of eigenvalues and eigenvectors (eigenpairs) of the system matrix. If the size of the problem is exceedingly large, the computation of the eigenpairs becomes computationally demanding and even prohibitive in some cases. This is due to the fact that the eigenpairs calculation requires a numerical

effort proportional to M^3, where M is the number of discrete points used in the field representation.

Consequently, in the simulation of two-dimensional optical waveguide problems using a relatively large value of M, the method of lines (MOL) approach (based on eigenpair calculation) becomes unpractical. A similar situation occurs in the simulation of three-dimensional problems, in which case M can easily become large, prohibiting the MOL approach. Part of the objectives of the present thesis work is to implement a new numerical approach [49, 50] that does not require calculation of the eigenpairs of the system matrix. The new approach is based on Padé approximants for the solution of the Helmholtz equation. This approach which will be discussed in detail in the next chapter, reduces the numerical effort significantly making it proportional to M, rather than the M^3 as in the case of the MOL. In the present chapter, however, the basic MOL formulation will be introduced including its use in the conventional manner. Extensions to the basic MOL will be discussed in this chapter as well. This includes:

1. Incorporation of a perfectly matched layer (PML).

2. The use of a higher order approximation of the second derivative operator in the transverse direction.

Finally, application of the MOL to calculate the reflected and transmitted fields due to a single and to a double longitudinal waveguide discontinuities will be discussed.

2.2.   BASIC MOL FORMULATION

One of the simplest optical waveguide structures is the dielectric slab waveguide. Because of longitudinal uniformity in its geometry, the guided modes and the radiation modes of the slab waveguide retain their basic shape as the field propagates within this waveguide and can thus be described by simple mathematical expressions. A schematic diagram of a three layer planar waveguide is shown in Figure 2-1. It consists of the superstrate, the core and the substrate with refractive indices n_3, n_1 and n_2, respectively, where $n_1 > (n_2,\ n_3)$ in order to ensure total internal reflection in the core. In order to simplify the numerical analysis, the structure is assumed to be uniform and infinitely stretched along the y direction, so that the field does not vary along the $y-$axis, which means $\frac{\partial}{\partial y} = 0$. The direction of propagation is assumed to be the $z-$direction and the time dependence is assumed to be $e^{-j\omega t}$. For this waveguide structure, the waveguide geometry is discretized in the x-direction and the boundary layers are parallel to the y-z plane. The computational window is bounded by an electric wall $(E_y = 0)$ or a magnetic wall $(H_y = 0)$. Under this assumption, the three-dimensional wave equation is reduced to a two-dimensional equation. The two dimensional wave equation is given by

$$\frac{\partial^2 \psi(x,z)}{\partial z^2} + \frac{\partial^2 \psi(x,z)}{\partial x^2} + k_0^2 n^2 \psi(x,z) = 0 \qquad (2.1)$$
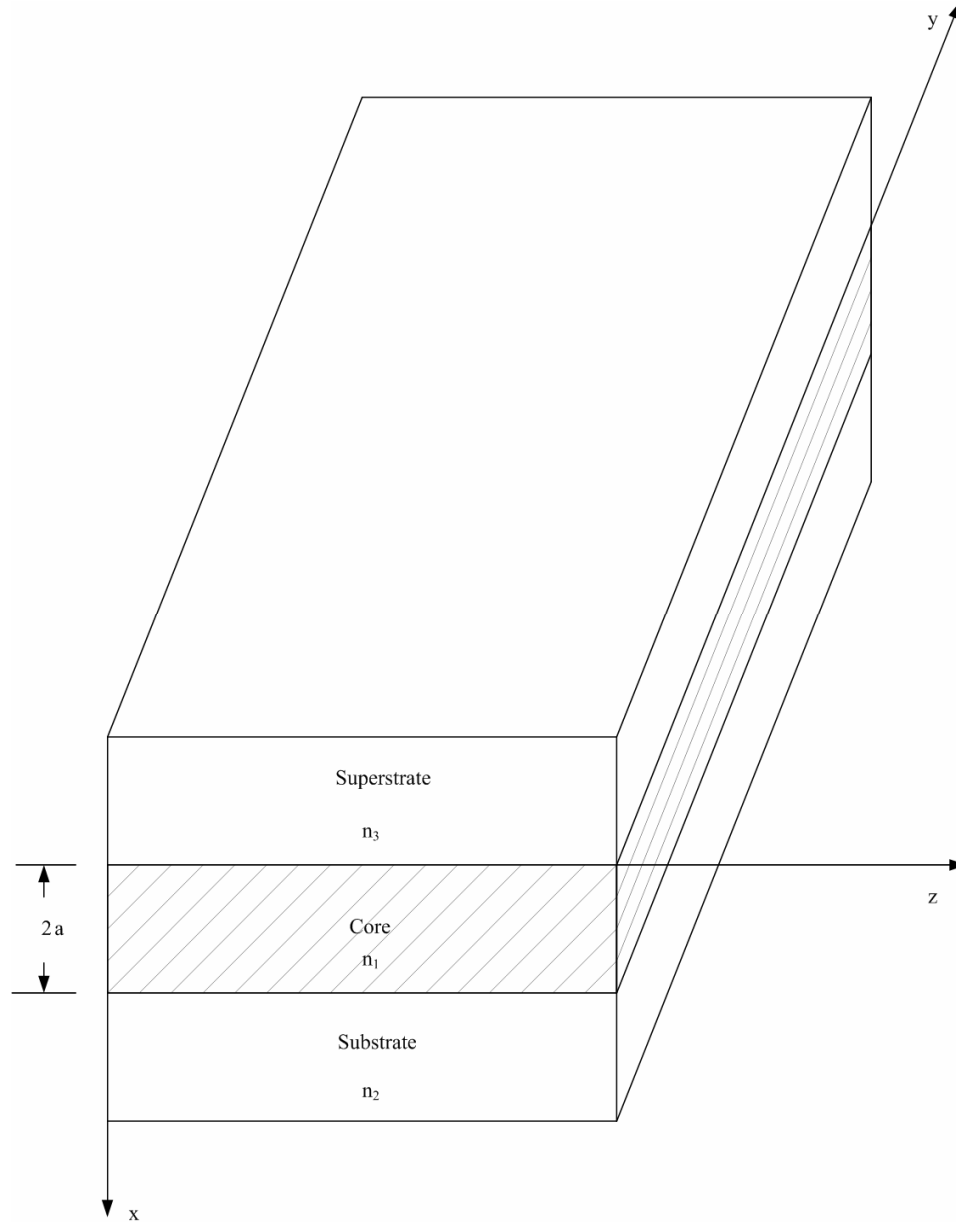
Figure 2-1 A dielectric slab waveguide

where ψ represents either E_y or H_y depending on whether we have *TE* or *TM*

polarized waves, respectively. k_0 is the free space wave number and n is the refractive

index. Upon discretization, the $\frac{\partial^2}{\partial x^2}$ term in equation (2.1) is replaced by the three-point

central difference approximation:

$$\frac{\partial^2 \psi_i}{\partial x^2} = \frac{\psi_{i+1} - 2\psi_i + \psi_{i-1}}{(\Delta x)^2} \qquad (2.2)$$

where the subscript i refers to the field at the ith mesh line in the discretized space, as

shown in Figure 2-2.
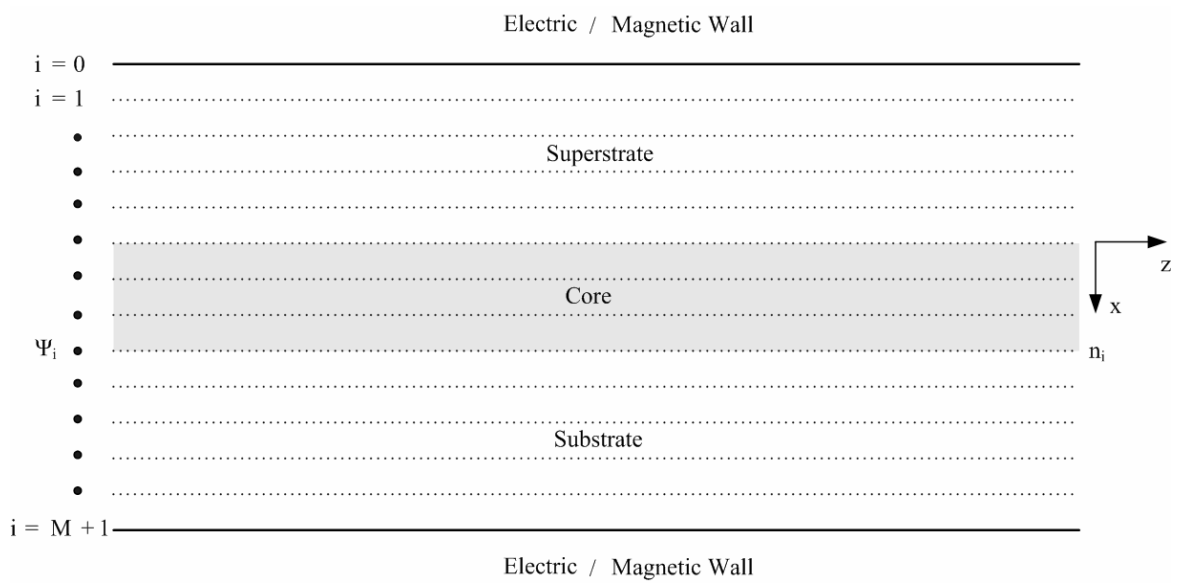
Figure 2-2 Discretization of space in the x-direction

Using equation (2.2), equation (2.1) can then be written in the form:

$$\frac{d^2 \psi_i(x,z)}{dz^2} + \frac{\psi_{i+1}(x,z) - 2\psi_i(x,z) + \psi_{i-1}(x,z)}{(\Delta x)^2} + k_o^2 n_i^2 \; \psi_i(x,z) = 0 \qquad (2.3)$$

If M is the total number of transverse discretization points, then equation (2.3) leads to the following matrix equation:

$$
\frac{d^2}{dz^2}
\begin{pmatrix}
\psi_1(z) \\
\psi_2(z) \\
\psi_3(z) \\
\vdots \\
\vdots \\
\vdots \\
\vdots \\
\psi_M(z)
\end{pmatrix}
+ \frac{1}{(\Delta x)^2}
\begin{pmatrix}
-2 & 1 & & & & & & \\
1 & -2 & 1 & & & & O & \\
 & 1 & -2 & 1 & & & & \\
 & & \ddots & \ddots & \ddots & & & \\
 & & & \ddots & \ddots & \ddots & & \\
 & & & & 1 & -2 & 1 & \\
 & O & & & & 1 & -2 & 1 \\
 & & & & & & 1 & -2
\end{pmatrix}
\begin{pmatrix}
\psi_1(z) \\
\psi_2(z) \\
\psi_3(z) \\
\vdots \\
\vdots \\
\vdots \\
\vdots \\
\psi_M(z)
\end{pmatrix}
+
$$

$$
+ k_0^2
\begin{pmatrix}
n_1^2 & & & & & & \\
 & n_2^2 & & & & O & \\
 & & n_3^2 & & & & \\
 & & & \ddots & & & \\
 & & & & \ddots & & \\
 & & & & & \ddots & \\
 O & & & & & & \ddots \\
 & & & & & & n_M^2
\end{pmatrix}
\begin{pmatrix}
\psi_1(z) \\
\psi_2(z) \\
\psi_3(z) \\
\vdots \\
\vdots \\
\vdots \\
\vdots \\
\psi_M(z)
\end{pmatrix}
=
\begin{pmatrix}
0 \\
0 \\
0 \\
\vdots \\
\vdots \\
\vdots \\
\vdots \\
0
\end{pmatrix}
\qquad (2.4)
$$

or, equivalently:

$$
\frac{d^2}{dz^2}\Psi + C\Psi + k_o^2 N\,\Psi = 0 \qquad (2.5)
$$

where C is a tri-diagonal matrix, N is a diagonal matrix with elements being the square of the refractive indices $(n_1^2\ n_2^2\ n_3^2\ \ldots\ldots)$ at the mesh points and $\Psi = [\psi_1(z)\ \ \psi_2(z)\ \ \psi_3(z)\ \ \cdots\ \ \psi_M(z)]^t$ is a column vector that represents the discretized field. Finally, equation (2.5) can be written as:

$$\frac{d^2\Psi}{dz^2} + Q\Psi = 0 \tag{2.6}$$

where $Q = C + k_0^2 N$.

Equation (2.6) is an ordinary second order matrix differential equation whose general solution is given by [10]

$$\Psi = e^{j\sqrt{Q}z}A + e^{-j\sqrt{Q}z}B \tag{2.7}$$

The first term on the right hand side of equation (2.7) represents field propagation in the $+z$ direction and the second term represents field propagation in the $-z$ direction. A and B represent the $\pm z$ propagating fields at $z = 0$, respectively. Both A and B are column vectors of size $M \times 1$, and $e^{+j\sqrt{Q}z}$ $\left(\text{or } e^{-j\sqrt{Q}z}\right)$ is a matrix of size $M \times M$ and is evaluated using eigenvalue decomposition. The square matrix Q is first expressed in terms of its eigenpairs in the form:

$$Q = UVU^{-1} \tag{2.8}$$

and

$$\sqrt{Q} = U\sqrt{V}U^{-1} \tag{2.9}$$

where U is the eigenvector matrix and V is a diagonal matrix containing the eigenvalues of Q. The matrix exponentials $e^{\pm j\sqrt{Q}z}$ can then be found using the following relation:

$$e^{\pm j\sqrt{Q}z} = Ue^{\pm j\sqrt{V}z}U^{-1} \tag{2.10}$$

The above procedure, which relies on eigenpair calculation for the evaluation of

$\sqrt{Q}$ and $e^{\pm j\sqrt{Q}z}$, is a fundamental feature of the MOL.

2.3. IMPROVEMENT TO THE BASIC MOL SCHEME

In the previous section, the basic MOL has been presented, however, important improvement and extensions are required to enhance the MOL performance. This includes the introduction of a suitable perfectly matched layer (PML) in order to absorb the radiative part of the field. In addition, the central difference approximation used to approximate $\frac{\partial^2}{\partial x^2}$ can be replaced with a much more accurate approximation using higher order approximation. The above extensions have been made to the basic MOL and the results will be presented next.

2.3.1. Perfectly Matched Layer

The field samples $\psi_0(z)$ and $\psi_{M+1}(z)$ are not included in equation (2.4) which implies that the computational window is terminated by either an electric or a magnetic wall $\left[\psi_0(z)=\psi_{M+1}(z)=0\right]$. The presence of these walls on the extreme end of the computational window causes the radiative field to experience complete reflection and causing it to return to the computational window and thus resulting in large errors in the calculated field. Because the problems under consideration in this thesis are unbounded,

there is a need for absorbing the radiated field. This can be done using the well known

Perfectly Matched Layer (PML) [11, 51-53]. PML layers are added on the top as well as

on the bottom of the computational window as shown in Figure 2-3. The PML that will

be used in this work is based on the transformation of the real space into the complex

space [52], so that the field is substantially attenuated before it reaches the electric wall

(magnetic wall) of the computational window. The real space is transformed to a complex

one according to:

$$x \rightarrow x(1 + j\sigma) \tag{2.11}$$

$$\Delta x \rightarrow \Delta x(1 + j\sigma) \tag{2.12}$$

where σ is the attenuation or the decay factor of the PML region. Under this type of

transformation, a wave $\left(e^{+jkx}\right)$ propagating in $+x$ direction becomes:

$$e^{+jkx(1+j\sigma)} = e^{+jkx}e^{-k\sigma x} \tag{2.13}$$

in the complex space. The resulting exponential decay factor causes the field to attenuate

in the $+x$ direction. The value of σ and the number of points in the PML are chosen so

that the field becomes significantly low when it reaches the electric or the magnetic wall

at the extreme end of the computational window.
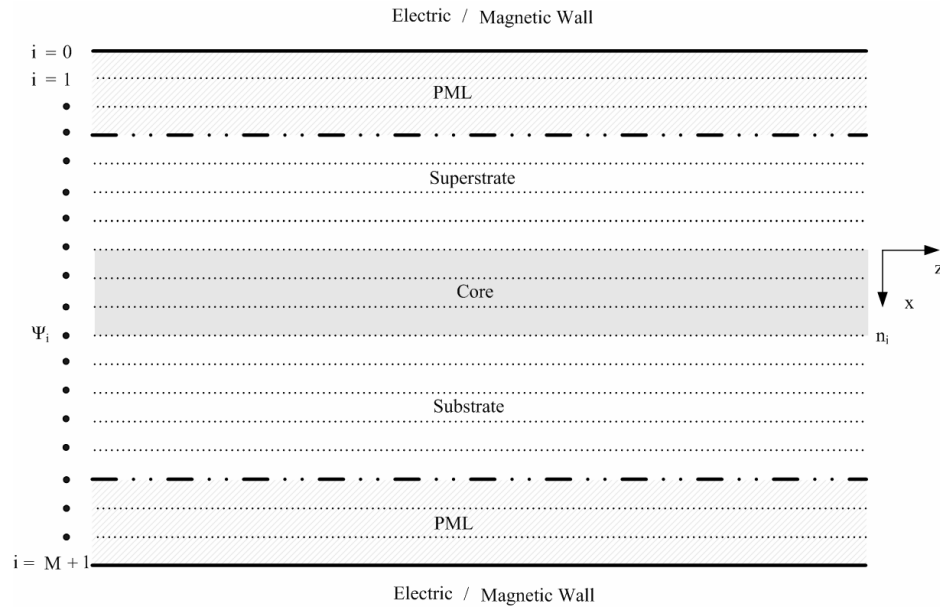
Figure 2-3 Discretization of space in the x-direction including the PML layers

There are various ways of selecting appropriate values of σ [54]. The value of σ may be assumed to be uniform throughout the *PML* region or else it can be taken as non-uniform. In general

$$(\sigma\Delta x)_i = \left(\frac{\eta}{P}\right) f(x_i) \tag{2.14}$$

where $(\sigma\Delta x)_i$ represents the value of the imaginary part of the mesh size σ at the ith mesh point in the *PML*, η is the *PML* strength parameter and P represents the number of mesh points in the *PML* layer. The parameter x_i is chosen as $x_i = \dfrac{i\pi}{2(P+1)}$ and $f(x_i)$ is an arbitrary increasing function of x_i, which can be linear $f(x_i) = x_i$, tangent $f(x_i) = \tan(x_i)$, parabolic $f(x_i) = x_i^2$ or any other suitable increasing function of x_i. In

this thesis work $f(x_i)$ is chosen to be tangent which has a superior performance compared to other functions.

In order to test the PML performance, a $TE-$polarized Gaussian beam is used as excitation at the input of a planar single mode three layer waveguide (see Figure 2-4). Because the Gaussian beam is not completely guided by the planar waveguide, the excess energy is radiated away from the waveguide core and effectively absorbed by the PML. After a sufficiently long distance in the $z-$direction the remaining field (guided) has a transverse pattern identical to the TE_0 mode pattern, as seen in the same figure.
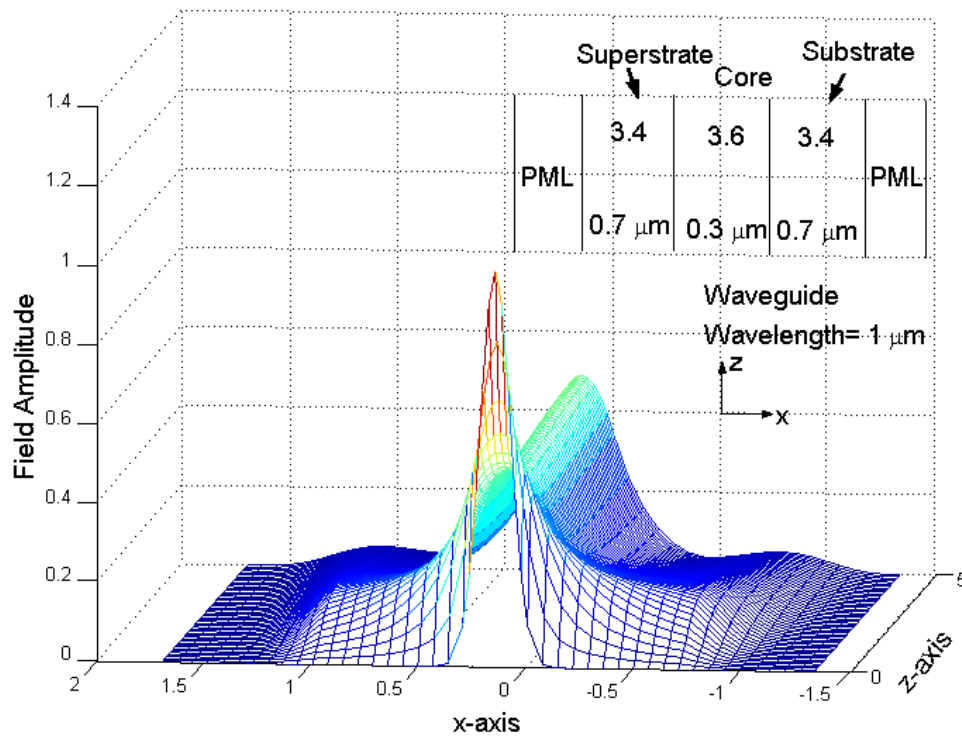
Figure 2-4 Gaussian beam propagation in single mode waveguide.

2.3.2. <u>Improvement to the Basic MOL Scheme</u>

In section 2 of this chapter, the $\frac{\partial^2}{\partial x^2}$ term was approximated by a three-point central difference approximation given by equation (2.2). This approximation is inaccurate as it does not incorporate the interface conditions at the superstrate/core and the core/substrate interfaces. It is also inefficient, because it utilizes a uniform meshing scheme. In order to efficiently model the field a three-point, five-point and seven-point approximation schemes that accounts for the boundary condition and that utilizes a non-uniform mesh size will be used in our work [55]. The use of higher order schemes reduces the numerical error due to the field discretization.

Consider the planar waveguide structure shown in Figure 2-5. The refractive indices of the superstrate, the substrate and the core are respectively taken as $n_3 = 1$, $n_2 = 3.4$, $n_1 = 3.6$. The width of the core is taken to be 0.3 μm. The widths of superstrate and the substrate are taken sufficiently wide in order for the TE_0 modal field to decay substantially before reaching the electric wall of the computational window. The wavelength of operation is 1 μm. This structure has been numerically simulated for evaluating the modal effective refractive index using the three, the five and the seven point approximation schemes with different number of discretization points. The 3, 5 and 7 point approximation schemes considered here have been reported in reference [17, 55] in detail and will not be shown in this thesis. The results are shown in Figure 2-6.
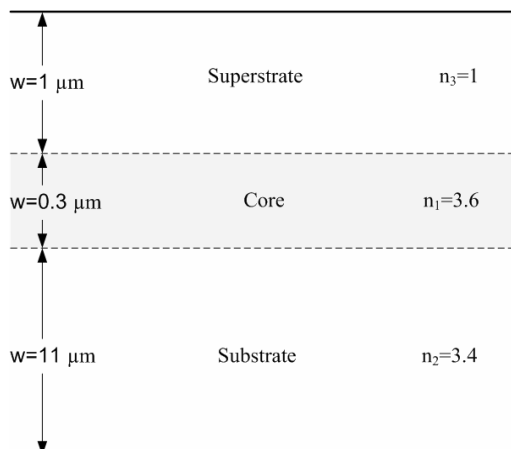
Figure 2-5 A three-layer waveguide
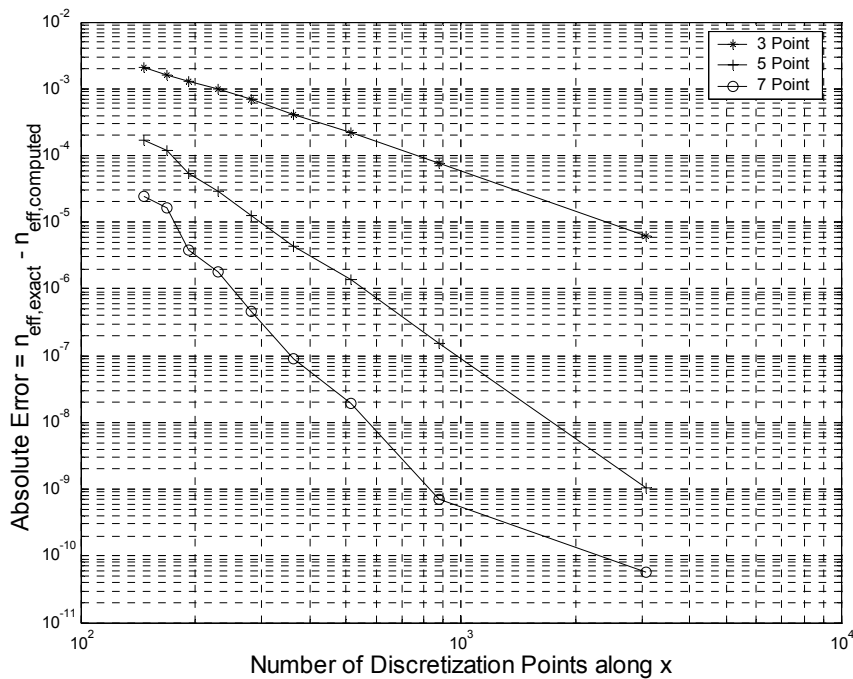
Figure 2-6 Absolute Error in the Effective Refractive Index for the 3-point, the 5-point and the 7-point approximation schemes versus the Number of Discretization Points.

The results shown in Figure 2-6 correspond to the TE_0 mode. For the TM_0 mode, the results are similar to those shown in Figure 2-6 and therefore, they will not be presented here. Figure 2-6 clearly shows a decrease in the absolute error $\left(\left|n_{eff, exact} - n_{eff, calculated}\right|\right)$ as the order of approximation increases and as the number of transverse discretization points increases. Accuracy and computational expense are the two major criteria for the selection of the approximation scheme. However, the five point approximation scheme provides significant accuracy and smaller computational expense when compared with the seven point approximation scheme. Therefore, the five point approximation scheme will be used throughout this thesis work.

2.4. ANALYSIS OF WAVEGUIDE DISCONTINUITIES

Longitudinal waveguide discontinuities can be modeled effectively by use of the MOL. Consider the simple case of a waveguide with a single longitudinal discontinuity as shown in Figure 2-7. The discontinuity is assumed to be located at $z = 0$. The problem space is divided into two regions namely region 0 and region 1. The field is assumed to be incident from region 0. Due to the discontinuity, part of the field is reflected back into region 0 and the remaining part of the field is transmitted to region 1.
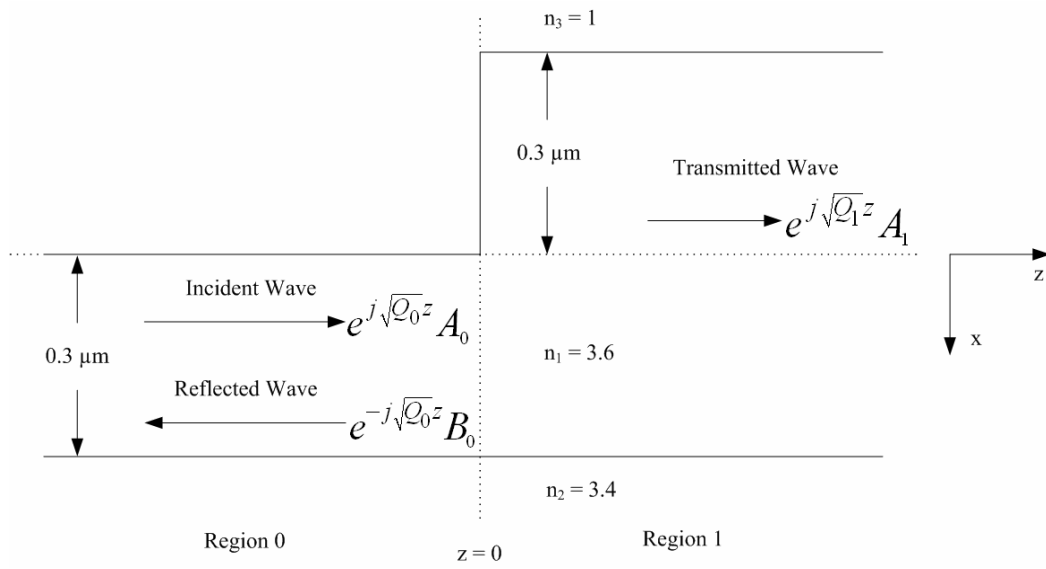
Figure 2-7 A single longitudinal waveguide discontinuity

The mathematical expressions for the transmitted and the reflected fields derived from the interface conditions at $z = 0$ are given as [12]:

$$B_0 = RA_0 \qquad (2.15)$$

and

$$A_1 = TA_0 \qquad (2.16)$$

where A_0 is the incident field in region 0 at $z = 0$, B_0 is the reflected field at $z = 0$ in region 0, and A_1 is the transmitted field at $z = 0$ in region 1. R and T are respectively, the reflection and the transmission matrices, which are given by:

$$R = \begin{cases} \left(I + S_0^{-1} S_1\right)^{-1} \left(I - S_0^{-1} S_1\right) & \text{For TE Polarization} \\ \left(I + S_0^{-1} N_0 N_1^{-1} S_1\right)^{-1} \left(I - S_0^{-1} N_0 N_1^{-1} S_1\right) & \text{For TM Polarization} \end{cases}$$

$$T = \begin{cases} 2\left(I + S_0^{-1} S_1\right)^{-1} & \text{For TE Polarization} \\ 2\left(I + S_0^{-1} N_0 N_1^{-1} S_1\right)^{-1} & \text{For TM Polarization} \end{cases}$$

where N_0 and N_1 are diagonal matrix containing the square of the refractive index distribution of region (0) and (1) respectively. I is the identity matrix having the same size as Q. In the above expressions S and S^{-1} are to be computed. Here $S = \sqrt{Q}$ where Q has been defined in section 2 and the subscripts 0 and 1 represent the respective region. S is evaluated by first decomposing Q in terms of its eigenpair, V and U. Where V is a diagonal matrix containing the eigenvalues of Q and U is a square matrix containing the corresponding eigenvectors of Q as column vectors. S is then evaluated using:

$$S = U V^{\frac{1}{2}} U^{-1} \tag{2.17}$$

Let us next consider the case of a planar waveguide structure with two longitudinal discontinuities one located at $z = 0$ and the other located at $z = d$ as shown in Figure 2-8. The problem space in this case is divided into three regions. The field within each region is the sum of the forward and the backward fields. Using the layer by layer algorithm [23, 56], the reflected and the transmitted fields are given as:

$$B_0 = \Gamma_0 A_0 \tag{2.18}$$

and

$$A_2 = 0.5\left[\left(I + S_2^{-1}S_1\right)D_1A_1 + \left(I - S_2^{-1}S_1\right)B_1\right] \tag{2.19}$$

where A_0 is the incident field in Region 0 and

$$\Gamma_0 = \left[\left(I - S_0^{-1}S_1\right) + \left(I + S_0^{-1}S_1\right)D_1\Gamma_1D_1\right]x$$
$$\left[\left(I + S_0^{-1}S_1\right) + \left(I - S_0^{-1}S_1\right)D_1\Gamma_1D_1\right]^{-1} \tag{2.20}$$

$$D_1 = e^{+jS_1d_1} \tag{2.21}$$

$$\Gamma_1 = \left[I - S_1^{-1}S_2\right]\left[I + S_0^{-1}S_1\right]^{-1} \tag{2.22}$$

$$B_1 = \Gamma_1D_1A_1 \tag{2.23}$$

$$A_1 = 0.5\left[\left(I + S_1^{-1}S_0\right)A_0 + \left(I - S_1^{-1}S_0\right)B_0\right] \tag{2.24}$$

The major difference between the single discontinuity and the double discontinuity waveguide (or the multiple discontinuity) problems is the appearance of the exponential factor $\left(D_1 = e^{+jS_1d_1}\right)$ in the equations (see equations (2.18)-(2.24)) to be solved. The exponential is evaluated in a similar manner to the square-root, using also eigenvalue decomposition, giving:

$$e^{+jSd} = Ue^{+j\sqrt{V}d}U^{-1} \tag{2.25}$$
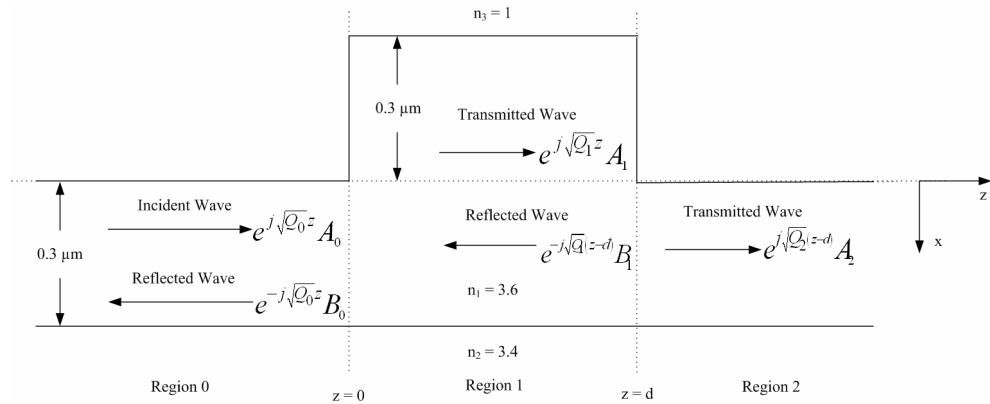
Figure 2-8 A double discontinuity waveguide

Multiple longitudinal discontinuities in a planar waveguide structure can be implemented using either the Layer by Layer [23, 56] or the Cascading and Doubling Procedures [13]. Numerical results for the single discontinuity and the double discontinuity problems will be presented in the next chapter including a comparison along of the new approach based on Padé approximants.

The *MOL* is known to have a high numerical accuracy. However, computation of the eigenvalues and the eigenvectors is numerically inefficient when the number of discretization points is too large. The memory and time requirements of the *MOL* is known to be proportional to M^2 and M^3 respectively [57].

In the next chapter we will introduce an alternative approach which does not rely on eigenpairs calculation. This new approach is based on Padé approximants [58]. Padé

approximants have been implemented in the beam propagation method (BPM) framework [34, 35, 38, 43, 44, 57, 59, 60]. This approach significantly reduces the numerical effort as will be demonstrated in the next chapter.

CHAPTER 3

APPLICATION OF PADÉ APPROXIMANTS TO THE METHOD OF LINES

3.1.   INTRODUCTION

As discussed in the previous chapter, the *MOL* relies on computing the eigenpairs of the system matrix, which makes it numerically inefficient when the matrix dimension is relatively large. However, computation of the eigenpairs can be avoided with the use of the Padé approximation, which makes it potentially a very efficient approach. The basic idea of Padé approximants is to overcome the divergent nature of Taylor series approximation by representing a given function as a ratio of two polynomials. Padé approximants can provide an approximation to the function throughout the whole complex plane, and is a topic of study in mathematical approximation theory [58].

3.2.   PADÉ APPROXIMANTS

A Padé Approximant is the ratio of two polynomials, the coefficients of these polynomials (called Padé primes) are constructed from the coefficients of the Taylor series expansion of the function to be approximated. This ratio is matched with the Taylor

series as far as necessary. Any arbitrary function $f(X)$ can be represented in one of the

two standard Padé forms:

$$f(X) = f(0)\left(1 + \sum_{k=1}^{p} \frac{h_k^{(p)} X}{1 + e_k^{(n)} X}\right) \tag{3.1}$$

or

$$f(X) = f(0)\left(\frac{\prod_{k=1}^{p} 1 + d_k^{(p)} X}{\prod_{k=1}^{n} 1 + e_k^{(n)} X}\right) \tag{3.2}$$

where $d_k^{(p)}$, $h_k^{(p)}$, are called Padé primes of order p for the numerator and $e_k^{(n)}$ is the

Padé prime of order n for the denominator. The approximated function is represented as

$P(p,n)$, where p is the order of the numerator and n is the order of the denominator. In

this thesis work the order of the numerator and the denominator are taken to be equal

$(p = n)$. The second Padé approximant form given by equation (3.2) will be used since it

offers certain advantages over the first form. The advantage of this form will be seen later.

In the next section, detailed explanation for obtaining Padé primes will be presented. It is

to be stressed here that this is just one of many other possible approaches that can be used

for this purpose.

3.3.   CALCULATION OF PADÉ PRIMES

Consider an arbitrary function $f(X)$ whose Padé primes are to be evaluated. This function is first represented by its Taylor series expansion as shown below

$$f(X) = \sum_{m=0}^{\infty} f^{(m)}(0) \frac{X^m}{m!} = \sum_{m=0}^{\infty} c_m X^m \tag{3.3}$$

where $c_m = f^{(m)}(0) \Big/ m!$ are the Taylor series coefficients.

In order to obtain a Padé approximation of order $P(N,N)$ we equate equation (3.3) to Padé approximation which has a form essentially the same as equation (3.2).

$$\sum_{m=0}^{\infty} c_m X^m = \frac{a_0 + a_1 X + a_2 X^2 + \cdots\cdots\cdots + a_N X^N}{b_0 + b_1 X + b_2 X^2 + \cdots\cdots\cdots + b_N X^N} \tag{3.4}$$

The symbol N has been used here to indicate the order of Padé approximants. In order to simplify our calculations we let $b_0 = 1$ which results in $a_0 = c_0 = f(0)$. Thus we are left with $2N$ unknowns, by considering the Taylor series terms up to $2N$ we should have sufficient equations to solve for the Padé primes. Thus we have:

$$\sum_{m=0}^{2N} c_m X^m = \frac{\displaystyle\sum_{i=0}^{N} a_i X^i}{\displaystyle\sum_{j=0}^{N} b_j X^j} \tag{3.5}$$

or

$$\sum_{m=0}^{2N} c_m X^m \sum_{i=0}^{N} b_i X^i = \sum_{j=0}^{N} a_j X^j \tag{3.6}$$

Matching the coefficients of equal powers of X from $N+1$ to $2N$ in equation (3.6) results in the following set of equations:

$$c_N b_N + c_{N+1} b_{N-1} + c_{N+2} b_{N-2} + \cdots\cdots + c_{2N-1} b_1 = -c_{2N}$$

$$c_{N-1} b_N + c_N b_{N-1} + c_{N+1} b_{N-2} + \cdots\cdots + c_{2N-2} b_1 = -c_{2N-1}$$

$$c_{N-2} b_N + c_{N-1} b_{N-1} + c_N b_{N-2} + \cdots\cdots + c_{2N-3} b_1 = -c_{2N-2}$$

$$\vdots \qquad \vdots \qquad \vdots \qquad \qquad \vdots \qquad \vdots \tag{3.7}$$

$$c_1 b_N + c_2 b_{N-1} + c_3 b_{N-2} + \cdots\cdots + c_N b_1 = -c_{N+1}$$

which can be represented in matrix form as:

$$\begin{bmatrix} c_N & c_{N+1} & c_{N+2} & \cdots & \cdots & c_{2N-1} \\ c_{N-1} & c_N & c_{N+1} & \cdots & \cdots & c_{2N-2} \\ c_{N-2} & c_{N-1} & c_N & \cdots & \cdots & c_{2N-3} \\ \vdots & \vdots & \vdots & \vdots & \vdots & \vdots \\ \vdots & \vdots & \vdots & \vdots & \vdots & \vdots \\ c_1 & c_2 & c_3 & \cdots & \cdots & c_N \end{bmatrix}_{NXN} \begin{bmatrix} b_N \\ b_{N-1} \\ b_{N-2} \\ \vdots \\ \vdots \\ b_1 \end{bmatrix}_{NX1} = \begin{bmatrix} -c_{2N} \\ -c_{2N-1} \\ -c_{2N-2} \\ \vdots \\ \vdots \\ -c_{N+1} \end{bmatrix}_{NX1} \tag{3.8}$$

or equivalently,

$$[C][B] = [\bar{C}] \tag{3.9}$$

Finally

$$[B] = [C]^{-1}[\bar{C}] \tag{3.10}$$

With the use of equation (3.10) all the b_i coefficients are evaluated. Using equation (3.6) and matching coefficients of equal powers of X from 0 to N, results in the following set of equations:

$$
\begin{aligned}
a_0 &= c_0 \\
a_1 &= c_0 b_1 + c_1 \\
a_2 &= c_0 b_2 + c_1 b_1 + c_2 \\
&\vdots \\
&\vdots \\
a_N &= c_0 b_N + c_1 b_{N-1} + c_2 b_{N-2} + \cdots\cdots + c_N
\end{aligned}
\tag{3.11}
$$

Which gives all the a_i coefficients from the previously calculated b_i coefficients. The form shown in equation (3.4) can easily be modified to be represented in product form (or zero-pole form) as shown in equation (3.2). This can be done by finding the roots of the numerator and the denominator in equation (3.4).

3.4.   PADÉ APPROXIMATION OF THE SQUARE ROOT

FUNCTION

Let us consider an example of the simple square-root function $\sqrt{y}$ of the scalar quantity y. The square root function is first modified in order to avoid the singularity of the higher derivatives of $\sqrt{y}$ in Taylor series expansion at $y = 0$. The function $\sqrt{y}$ is then rewritten as

$$\sqrt{y} = f(X) = \sqrt{1+X} \tag{3.12}$$

$$\sqrt{1+X} \approx 1 + \sum_{k=1}^{p} \frac{h_k^{(p)} X}{1+e_k^{(p)} X} = \prod_{k=1}^{p} \frac{1+d_k^{(p)} X}{1+e_k^{(p)} X} \tag{3.13}$$

where $X = y - 1$, and $d_k^{(p)}$, $e_k^{(p)}$ and $h_k^{(p)}$ are called Padé primes of order p. These Padé primes are actually available in closed form [60] and are obtained from $e_k^{(p)} = \cos^2(k\theta)$, $h_k^{(p)} = \sin^2(k\theta)$, $d_k^{(p)} = \dfrac{c_k^{(p)}}{p+0.5}$ where $\theta = \dfrac{\pi}{2p+1}$.

The Padé primes of the same square root function were evaluated using the above mentioned method and compared with the ones available in closed form. The results are presented in Table 3-1.

Table 3-1 Comparison of Padé Primes of order P (10, 10) for the Square Root Function

Padé Primes	Developed Program	Closed Form	Absolute Error	Padé Primes	Developed Program	Closed Form	Absolute Error
d_1	2.2214E-02	2.2214E-02	4.7330E-08	e_1	9.7779E-01	9.7779E-01	3.0580E-08
d_2	8.6880E-02	8.6881E-02	1.6807E-07	e_2	9.1312E-01	9.1312E-01	1.1513E-07
d_3	1.8825E-01	1.8826E-01	3.0972E-07	e_3	8.1174E-01	8.1174E-01	2.3235E-07
d_4	3.1733E-01	3.1733E-01	4.1448E-07	e_4	6.8267E-01	6.8267E-01	3.4995E-07
d_5	4.6263E-01	4.6263E-01	4.4506E-07	e_5	5.3736E-01	5.3737E-01	4.2986E-07
d_6	6.1126E-01	6.1126E-01	3.9691E-07	e_6	3.8874E-01	3.8874E-01	4.4011E-07
d_7	7.5000E-01	7.5000E-01	2.9349E-07	e_7	2.5000E-01	2.5000E-01	3.6975E-07
d_8	8.6653E-01	8.6653E-01	1.7141E-07	e_8	1.3347E-01	1.3347E-01	2.4011E-07
d_9	9.5048E-01	9.5048E-01	6.7172E-08	e_9	4.9515E-02	4.9516E-02	1.0134E-07
d_{10}	9.9442E-01	9.9442E-01	7.7363E-09	e_{10}	5.5846E-03	5.5846E-03	1.2190E-08

For the above mentioned square root function, the Padé approximation of equation (3.13) is not accurate when $y < 0$ (this fact can easily be concluded, since $\sqrt{y}$ is pure imaginary when $y < 0$, while the calculated Padé primes are real. Padé approximants predict a real number for $\sqrt{y}$ in this case, which is a clear contradiction). Figure 3-1 shows the absolute relative error in calculating $\sqrt{y}$ using Padé approximants of order $P(5, 5)$ as well as the error that results from the use of Taylor series expansion of order 10.

The relative error $\left(R.E.\right)$ is defined as:

$$R.E. = \frac{\left|f_{exact} - f_{approx}\right|}{f_{exact}} \qquad (3.14)$$

where f_{exact} is the exact value of the function and f_{approx} is its approximated value using either Padé approximants or Taylor series approximation.

It is well known that the Taylor series has a limited range of convergence, when y increases beyond this range Taylor series expansion fails to converge. However, the Padé approximation has a wider range of convergence for positive values of y and comparatively superior performance with respect to Taylor series approximation. This fact can easily be seen in Figure 3-1. In this figure, the Padé approximation results in small error for $y > 0$. However, for $y < 0$, it produces large relative error. Hence, equation (3.13) cannot be used to approximate the square root function for $y < 0$.
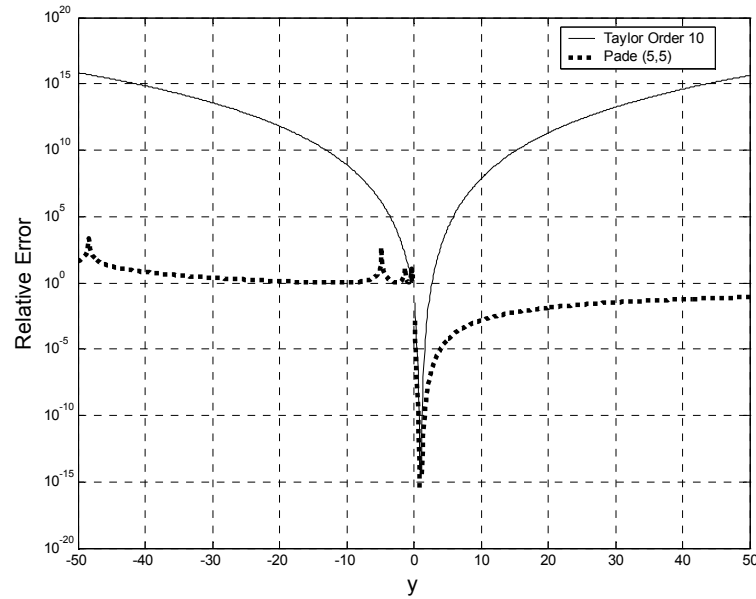
Figure 3-1 The relative error for $\sqrt{y}$ using Taylor and Padé approximations

In order to extend Padé approximation to include the range $y < 0$, we use [49]:

$$\sqrt{y} = \gamma^{-\frac{1}{2}}\sqrt{1 + (\gamma y - 1)} \qquad (3.15)$$

or,

$$= \gamma^{-\frac{1}{2}}\sqrt{1 + X} \qquad (3.16)$$

where $X = \gamma y - 1$ is used in this case. The complex factor γ can be written in the form $\gamma = \alpha e^{j\theta}$ where α is the magnitude and θ is the angle of γ. When $\theta \neq 0$, the factor γ causes the branch cut of the square root function to be rotated in the complex plane. In this case, equation (3.13) can be used to approximate $\sqrt{1 + X}$ appearing in equation (3.16)

Figure 3-2 shows the relative error for the square root function for different values of γ. When we make γ pure imaginary by letting $\theta = -\pi/2$, we find a substantial decrease in the relative error of the Padé approximants of the square root function. The relative error is reduced even further when α the magnitude of γ is reduced. In reality, there is a limited range of α and θ, for which Padé approximation converges. In the next sections, when Padé approximation with branch cut rotation is applied to the *MOL*, we will address the range of α and θ that result in low calculational errors.
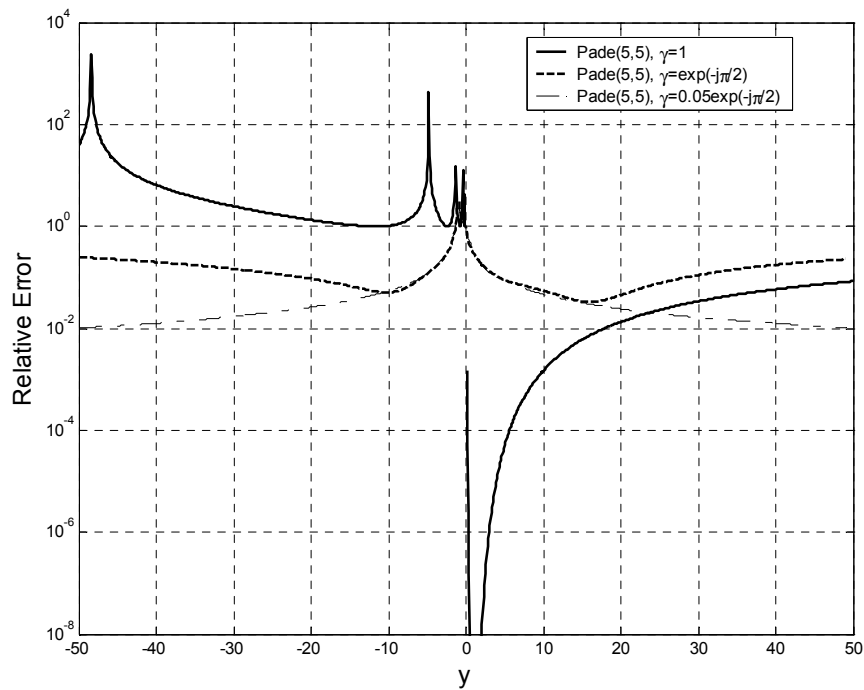
Figure 3-2 Relative Error of $\sqrt{y}$ using Padé Approximations with and without branch cut rotation

3.5.   IMPLEMENTATION OF THE MOL WITH PADÉ

APPROXIMANTS

This section is divided into three sub-sections. The first sub-section deals with the computation of the reflection operator at a single longitudinal discontinuity using Padé approximants. The second sub-section deals with the computation of the propagation operator. Finally, in the third sub-section, a generalized approach that utilizes Padé approximants is developed for the analysis of multiple longitudinal waveguide discontinuities.

3.5.1. <u>Implementation of the Reflection Operator</u>

As discussed in the previous chapter, the problem of a single longitudinal discontinuity (see Figure 3-3) involves computation of $S = \sqrt{Q}$. The matrix Q is inherently sparse and computing its square root produces a full matrix, which results in large memory requirements. With the use of Padé approximants (as in equation 2.2), the sparsity of the matrices can be fully utilized which results in small memory requirements and faster computational time. Applying equations (2.15) and (2.16) for TE polarized waves at the single longitudinal discontinuity, we have:

$$B_0 = \left(I + S_0^{-1}S_1\right)^{-1}\left(I - S_0^{-1}S_1\right)A_0 \qquad (3.17)$$

$$A_1 = 2\left(I + S_0^{-1}S_1\right)^{-1}A_0 \qquad (3.18)$$

Equation (3.17) is first rewritten in the form:

$$\left(I + S_0^{-1}S_1\right)B_0 = \left(I - S_0^{-1}S_1\right)A_0 \qquad (3.19)$$

Incorporating Padé approximation for S_1 and S_0^{-1} in equation (3.19) leads to the following relationship:

$$\left(I + \gamma_0^{+\frac{1}{2}}\left[\prod_{k=1}^{p}\frac{I + b_k^{(p)}X_0}{I + a_k^{(p)}X_0}\right]\gamma_1^{-\frac{1}{2}}\left[\prod_{k=1}^{p}\frac{I + a_k^{(p)}X_1}{I + b_k^{(p)}X_1}\right]\right)B_0 =$$

$$\left(I - \gamma_0^{+\frac{1}{2}}\left[\prod_{k=1}^{p}\frac{I + b_k^{(p)}X_0}{I + a_k^{(p)}X_0}\right]\gamma_1^{-\frac{1}{2}}\left[\prod_{k=1}^{p}\frac{I + a_k^{(p)}X_1}{I + b_k^{(p)}X_1}\right]\right)A_0 \qquad (3.20)$$

where $X_0 = \gamma_0 Q_0 - I$, $X_1 = \gamma_1 Q_1 - I$. The complex constants γ_0 and γ_1 are associated with region 0 and region 1 respectively. For simplicity, we will assume that $\gamma_0 = \gamma_1$, so that $\gamma_0^{-\frac{1}{2}}\gamma_1^{\frac{1}{2}} = 1$. I represents the identity matrix with the same dimensions as Q. S_1^{-1} can easily be obtained by simply interchanging the Padé primes of the numerator and the denominator respectively as clearly seen in equation (3.20). Expanding equation (3.20) for the case $p = 4$ (i.e. fourth order Padé approximants):

$$\left\{I + \left(\frac{I + b_1 X_0}{I + a_1 X_0}\right)\left(\frac{I + b_2 X_0}{I + a_2 X_0}\right)\left(\frac{I + b_3 X_0}{I + a_3 X_0}\right)\left(\frac{I + b_4 X_0}{I + a_4 X_0}\right)\right.$$

$$\left.\left(\frac{I + a_1 X_1}{I + b_1 X_1}\right)\left(\frac{I + a_2 X_1}{I + b_2 X_1}\right)\left(\frac{I + a_3 X_1}{I + b_3 X_1}\right)\left(\frac{I + a_4 X_1}{I + b_4 X_1}\right)\right\}B_0 =$$

$$\left\{I - \left(\frac{I + b_1 X_0}{I + a_1 X_0}\right)\left(\frac{I + b_2 X_0}{I + a_2 X_0}\right)\left(\frac{I + b_3 X_0}{I + a_3 X_0}\right)\left(\frac{I + b_4 X_0}{I + a_4 X_0}\right)\right. \qquad (3.21)$$

$$\left.\left(\frac{I + a_1 X_1}{I + b_1 X_1}\right)\left(\frac{I + a_2 X_1}{I + b_2 X_1}\right)\left(\frac{I + a_3 X_1}{I + b_3 X_1}\right)\left(\frac{I + a_4 X_1}{I + b_4 X_1}\right)\right\}A_0$$

In equation (3.21) the matrices X_0 and X_1 are sparse because Q_0 and Q_1 are also

sparse and A_0 and B_0 are M element column vectors. Considering the right hand side

(RHS) of equation (3.21), we first multiply $(I + a_4 X_1)$ with A_0 which results in a

column vector. The resulting vector is next left divided by $(I + b_4 X_1)$ which again results

in a column vector. The left division is used in this case to avoid inversion of $(I + b_4 X_1)$,

which would result in a full matrix, thereby causing both the memory and runtime

requirements to be large. Thus, by repeating this procedure we would never encounter full

matrices and after every multiplication and division step the resultant is a column vector.

Thus equation (3.21) is implemented computationally using only sparse matrix vector

product and sparse matrix vector divide. After computing the RHS of equation (3.21), B_0

can then be calculated using the BICGSTAB (Biconjugate Gradients Stabilized Method)

[61] subroutine in Matlab environment which solves a system of linear equations

iteratively. BICGSTAB guesses a particular value of B_0 and that guessed value is fed as

input to a function which evaluates the LHS of equation (3.21) in a similar way as the

RHS was evaluated and then tries to equate it to the RHS. If the residual norm is less

than a certain specified value, then BICGSTAB converges. The convergence of

BICGSTAB depends on the type of the problem at hand. If the problem is complex then

BICGSTAB needs more iterations to converge which in turn increases the computational

time. The single longitudinal discontinuity problem presented in section 4 of chapter 2

was calculated using the method that we have just described. The input waveguide is

excited by its fundamental TE mode, whose profile is shown in Figure 3-4. The reflected

and the transmitted fields are shown in Figure 3-5 and 3-6 for a range of Padé orders using

$\alpha = 1$ and $\theta = -\pi/2$.
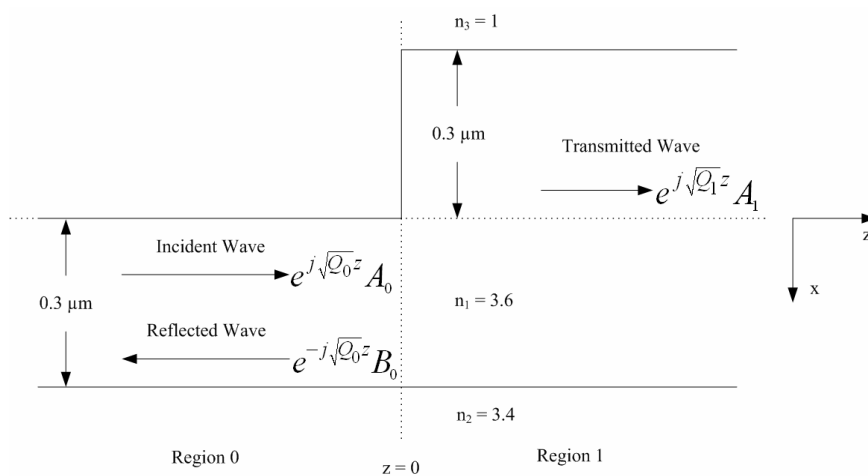
Figure 3-3 An abrupt longitudinal waveguide discontinuity
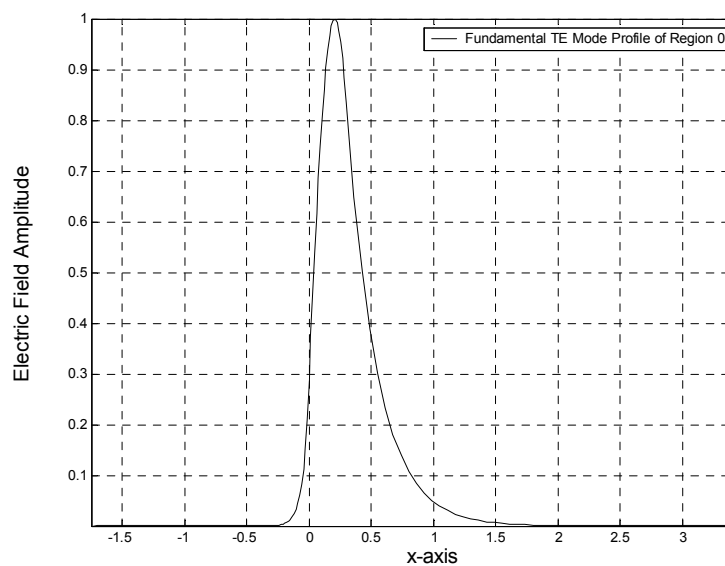
Figure 3-4 Profile of the Incident field in region 0, which corresponds to the fundamental TE mode
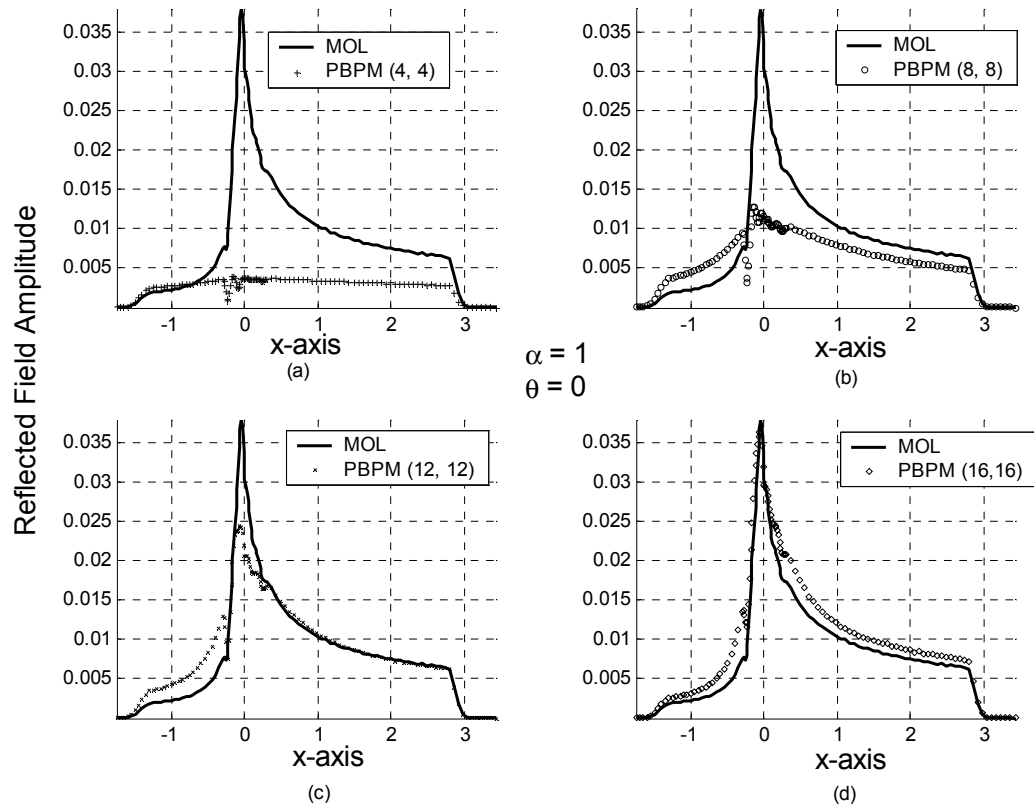
Figure 3-5 Reflected field at $z = 0$ at the waveguide discontinuity using the MOL and the PBPM computational methods. The order of Padé approximants are shown in the brackets.

As shown in Figure 3-5, with the increase in the Padé order in the MOL, the reflected fields computed using the MOL and $PBPM$ have better agreement as the Padé order increases. However, even when the Padé order becomes large [i.e. order P (16, 16)], as seen in Figure 3-5 d, there is a substantial disparity between the two approaches. This situation can be largely improved by reducing the value of $\alpha = |\gamma|$, as can be seen in the next set of figures (see Figure 3-6 a-d).

When α is reduced from unity to 0.1, the agreement in the calculated reflected

fields improves, as seen in Figure 3-6 a. A better agreement is achieved for $\alpha = 0.02$ and

$\alpha = 0.01$ as seen in Figure 3-6 b and c. However, when α is too low the calculated

results begin to disagree again (see Figure 3-6 d). The value of $\alpha = 0.0007$ is too low to

allow accurate results using the *PBPM* for this particular problem. It is noteworthy that

the calculated results shown in Figure 3-6 correspond to a Padé order of 4. This means

that there is a range of values of the parameter α for which the *PBPM* gives accurate

results for the reflected field, even for a relatively low order of Padé approximant.
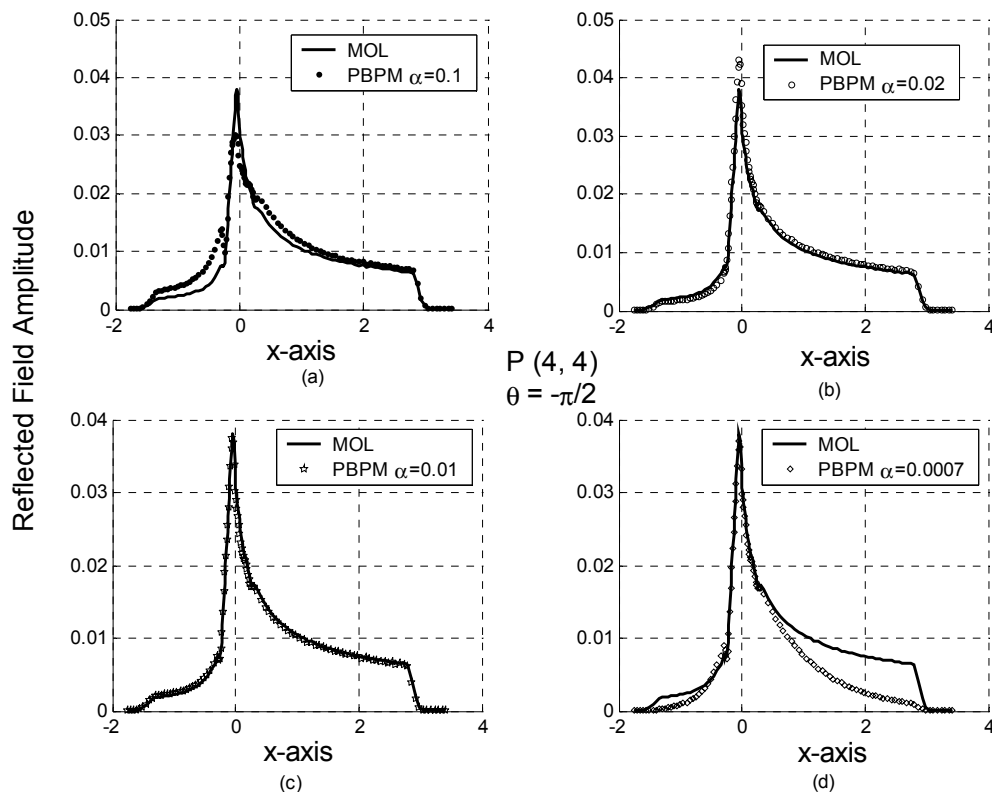
Figure 3-6 Reflected field at $z = 0$ at the waveguide discontinuity using the MOL and PBPM computational methods.

The effect of the magnitude α and the phase θ of γ is analyzed for various Padé orders in the computation of the reflected field. Firstly, the effect of α is studied. Figure 3-7 shows the root mean square error between the reflected fields computed using the *PBPM* with different values of α and *MOL* computational methods. The root mean square relative error is defined as:

$$Relative\ Error = \left[\frac{\sum_{i=1}^{M}\left(\left|\psi_i^c\right|-\left|\psi_i^p\right|\right)^2}{\sum_{i=1}^{M}\left|\psi_i^c\right|^2} \right]^{\frac{1}{2}} \tag{3.22}$$

where ψ represents the field and the superscripts c and p refer to *MOL* and *PBPM* respectively.
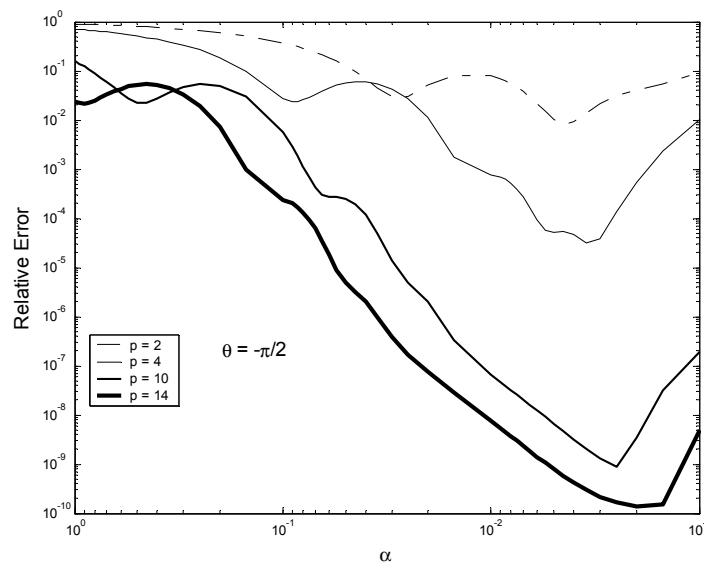
Figure 3-7 Relative error in the reflected field (computed using the PBPM, and the MOL computational methods) versus α with $\theta = \pi/2$

As seen in Figure 3-7, there is a range of α for which the error is low. This range of α depends on Padé order used and this range is seen to increase with higher orders of Padé approximation. For the case of $p = 4$, α ranges approximately from 1×10^{-3} to 2×10^{-2}. Based on a number of simulations for various problems, the value of α was set to $\alpha = \dfrac{1}{(1.5k_0)^2}$, where k_0 is the wave number. The value of α in this case is evaluated to be 0.011, which lies within the range of α specified above for low error. In this thesis work, the value of α is fixed to $(1.5k_0)^{-2}$. However, the phase θ also has a significant effect on the convergence of the $PBPM$.

Figure 3-8 shows the relative error in the reflected field versus θ and fixed value of $\alpha = 0.011$. As can be seen in the figure, the optimum value of θ also depends on the Padé order used. However, for any Padé order $p \geq 4$, $\theta = -\pi/2$ is seen to have a low relative error $(\leq 10^{-3})$. Thus, $\alpha = (1.5 \times k_0)^{-2}$ and $\theta = -\pi/2$ will be used throughout this thesis. The Padé order $p = 4$ will be fixed, for the square root operator, throughout the thesis work.
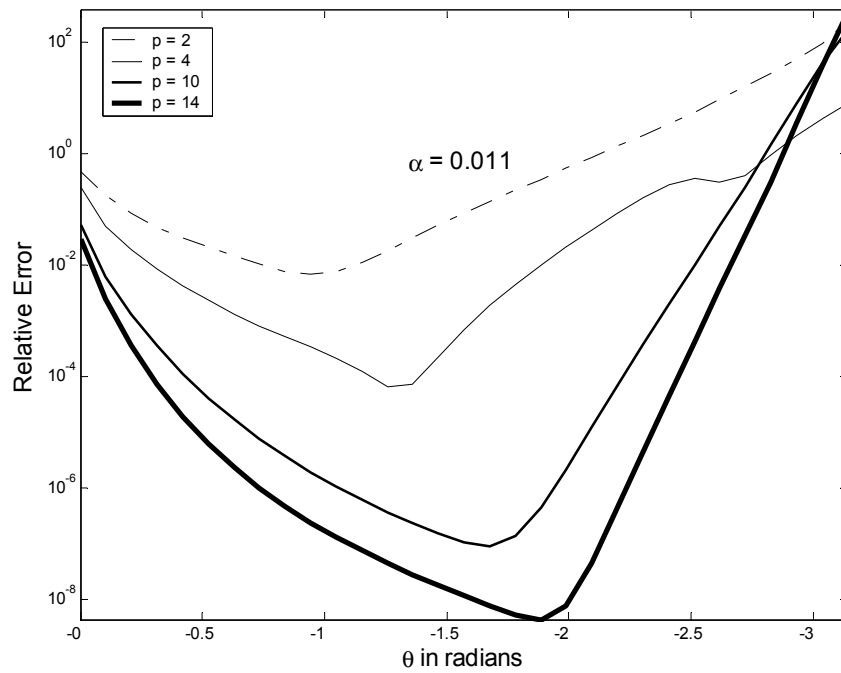
Figure 3-8 Relative error in the reflected field (computed using the PBPM and the MOL computational methods) versus θ with $\alpha = 0.011$

Using the above mentioned fixed values, the reflected field is computed. After computing the reflected field B_0, the transmitted field A_1 can easily be obtained using the relationship $A_1 = A_0 + B_0$. Figure 3-9 shows the transmitted field A_1 computed using the *PBPM* and the *MOL* methods. As can be seen in the figure, the two fields agree well with each other.
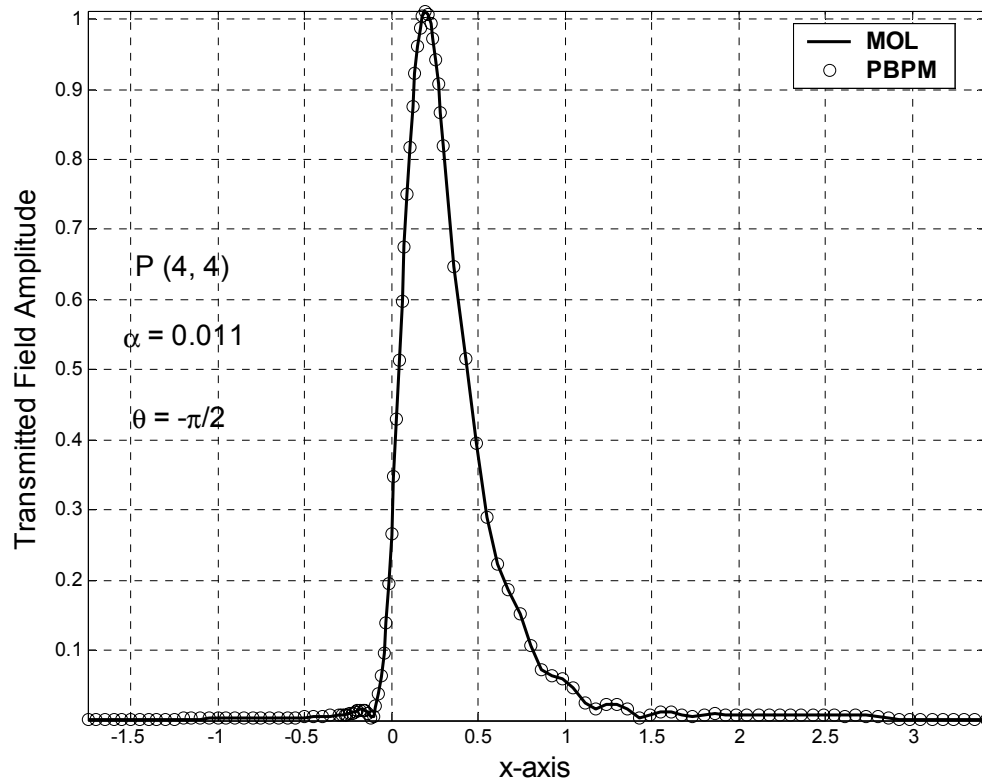
Figure 3-9 Transmitted field at $z = 0$ at the waveguide discontinuity using the MOL and the PBPM computational methods

Figure 3-10 shows the computational time requirements for the *MOL* and the *PBPM* for the calculation of the reflected field at the waveguide discontinuity. Clearly, the time taken to numerically simulate the single discontinuity problem with the *MOL* is many folds more than that required by the *PBPM* .
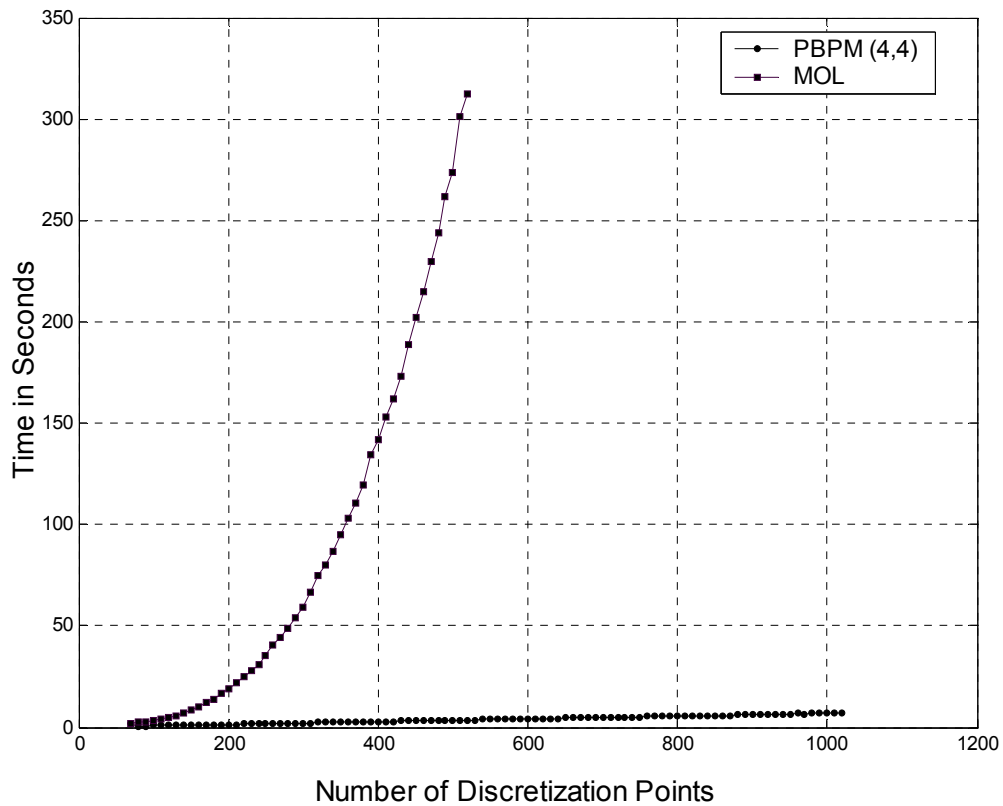
Figure 3-10 Comparison of computational time requirements for the MOL and the PBPM for the calculation of the reflected field

The time taken by the *MOL* when the number of transverse mesh points $M = 520$ is 312.06 seconds. For the same case, the time requirement is reduced to just 3.6 seconds when the *PBPM* is used. The *PBPM* is faster than the *MOL* in this case by a factor of approximately 85. From Figure 3-10, it is also easily seen that the *MOL* time requirement is proportional to M^3. However, the *PBPM* time requirement is proportional to M.

3.5.2. <u>Implementation of the Propagation Operator</u>

In order to analyze multiple discontinuities the propagation operator $e^{+jSz} = e^{+j\sqrt{Q}z}$ discussed at the outset of this section also needs to be accounted for in the $PBPM$. For this purpose, we express this term as:

$$
\begin{aligned}
e^{+j\sqrt{Q}d} &= e^{+j\gamma^{-\frac{1}{2}}\sqrt{1+(\gamma Q-1)}z} \\
&= e^{+j\gamma^{-\frac{1}{2}}\sqrt{1+X}z} \\
&= e^{g\sqrt{1+X}}
\end{aligned}
\tag{3.23}
$$

where $g = +j\gamma^{-\frac{1}{2}}z$ and $X = \gamma Q - I$. The Taylor series expansion coefficients of $\exp\left(g\sqrt{1+X}\right)$ need to be obtained first. Calculation of Taylor series coefficients of this function is straight forward, but this task becomes tedious for higher order coefficients. In order to simplify this process, we have used the Matlab symbolic math function for this purpose. The coefficients which are functions of g are given by:

$$c(0) = \exp(g)$$

$$c(1) = \frac{1}{2}(g)\exp(g)$$

$$c(2) = \left(-\frac{1}{8}g + \frac{1}{8}g^2\right)\exp(g)$$

$$c(3) = \left(\frac{1}{16}g - \frac{1}{16}g^2 + \frac{1}{48}g^3\right)\exp(g) \qquad (3.24)$$

$$c(4) = \left(-\frac{5}{128}g + \frac{5}{128}g^2 - \frac{1}{64}g^3 + \frac{1}{384}g^4\right)\exp(g)$$

$$\vdots$$
$$\vdots$$
$$\vdots$$

The expressions for the coefficients in equation (3.24) are stored as a function in an m-file with g as a variable, which can be accessed to compute the Taylor series coefficients, whenever needed.

Based on a number of simulations, it became clear to us that there is an upper limit on z $(\triangle z)$, which depends on the problem at hand. However, the most important attribute of the maximum step size $\triangle z$ is that, it is actually independent of Δx (the transverse mesh size). Subsequently, if the field needs to be propagated over a distance larger than the maximum step size Δz, then multi-step propagation is used.

In order to analyze the effect of $\triangle z$, a $TE-$polarized Gaussian beam with a spot size of $0.1\mu m$ was propagated a total distance of $5\mu m$ in a homogeneous medium (see

Figure 3-11) of width 3 μm and refractive index $n=1$ at the operating wavelength λ=1.0 μm. The Gaussian beam is first propagated over the 5 μm distance using the MOL. The same beam was then propagated using the $PBPM$ using different values of Δz. The order of the Padé approximants for the propagation operator is set to $p=10$. This order will be used throughout this thesis work to approximate the propagation operator.
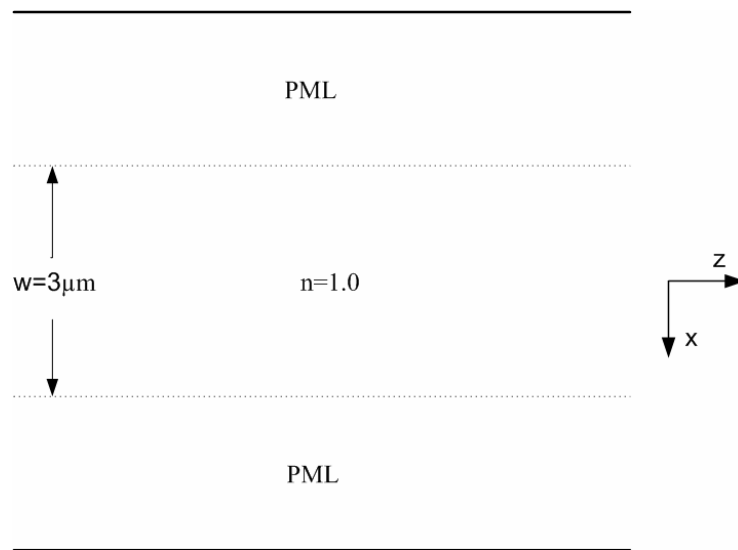
Figure 3-11 A homogeneous medium

In Figure 3-12, the Gaussian beam propagation over the 5 μm distance, as calculated by the MOL is used as reference. When the step size Δz is relatively large, the $PBPM$ results are clearly inaccurate (see Figure 3-12 (a) corresponding to $\Delta z = 2$ μm). However, as seen in the remaining figures (3-12 b-d), when Δz is approximately 0.5 μm or less, the $PBPM$ results agree very well with the MOL calculations. Although, this may

appear as a serious limitation of the *PBPM* , the *PBPM* actually remains more efficient than the *MOL* with respect to the CPU time and memory requirements, as will be seen later.
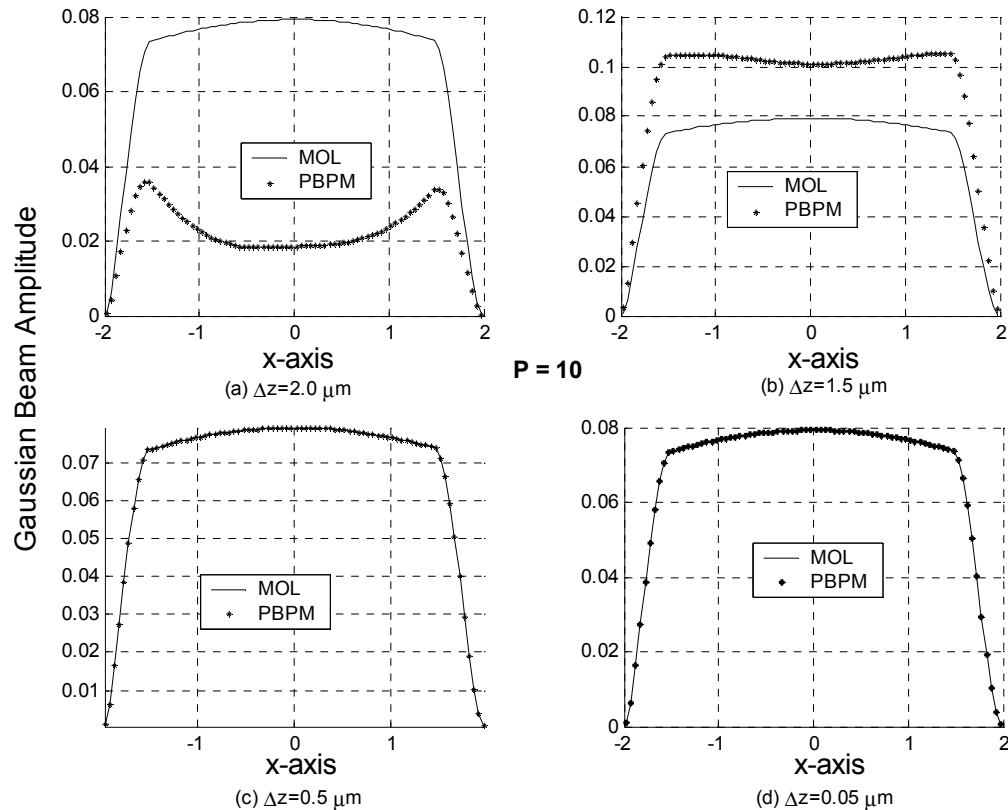
Figure 3-12 Comparison of the MOL and the PBPM in the case of Gaussian beam propagation over a 5 μm distance in air

In the previous two sections (5.1 and 5.2), we have presented and demonstrated the application of the *PBPM* in the case of reflection from a single longitudinal discontinuity as well beam propagation in a longitudinally uniform region. However, many interesting integrated optical devices involve multiple longitudinal discontinuities. The procedures

presented in section 5.1 and 5.2 cannot be used on their own to handle this type of problem. Thus, we need a general procedure that can effectively account for multiple longitudinal waveguide discontinuities. This general procedure, which will be presented in the next section relies on the results that were presented in sections 5.1 and 5.2 as will be seen next.

3.5.3. <u>Generalized PMOL Procedure for Analysis of Multiple Longitudinal Waveguide Discontinuities</u>

Consider the arbitrary structure shown in Figure 3-13 which contains multiple longitudinal discontinuities along the direction of wave propagation. The discontinuities are assumed to be present at z_i where $i = 0,\ 1,\ 2\ ....,\ \text{m-1, m, ..., L}$.
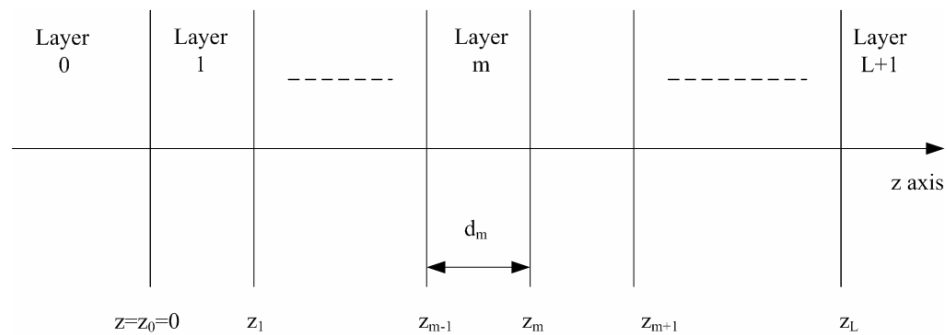
Figure 3-13 Arbitrary multiple longitudinal waveguide discontinuities

The first discontinuity is assumed to be at the origin. The width of the mth layer is $d_m \equiv z_m - z_{m-1}$. The field in the mth layer is expressed as:

$$\psi_m = e^{jS_m(z-z_{m-1})} A_m + e^{-jS_m(z-z_m)} B_m \qquad (3.25)$$

For $TE-$polarized waves, application of the boundary conditions at $z = z_m$ result in:

$$P_m A_m + B_m = A_{m+1} + P_{m+1} B_{m+1} \qquad (3.26)$$

and

$$S_m P_m A_m - S_m B_m = S_{m+1} A_{m+1} - S_{m+1} P_{m+1} B_{m+1} \qquad (3.27)$$

where

$$P_m = e^{jS_m d_m} = e^{jS_m(z_m - z_{m-1})} \qquad (3.28)$$

and $P_0 = I$, where I is the identity matrix having the same size as Q. By substituting different values of m in equations (3.26) and (3.27), we have:

$$A_1 + B_0 - P_1 B_1 = -P_0 A_0 = -A_0 \qquad (3.29)$$

$$-S_1 A_1 - S_0 B_0 + S_1 P_1 B_1 = -S_0 A_0 \qquad (3.30)$$

$$P_1 A_1 - A_2 + B_1 - P_2 B_2 = 0 \qquad (3.31)$$

$$S_1 P_1 A_1 - S_2 A_2 - S_1 B_1 + S_2 P_2 B_2 = 0 \qquad (3.32)$$

$$P_2 A_2 - A_3 + B_2 - P_3 B_3 = 0 \qquad (3.33)$$

$$S_2 P_2 A_2 - S_3 A_3 - S_2 B_2 + S_3 P_3 B_3 = 0 \qquad (3.34)$$

We proceed in this manner and finally arrive at the last set of equations which are:

$$P_L A_L - A_{L+1} + B_L - P_{L+1} B_{L+1} = 0 \tag{3.35}$$

$$S_L P_L A_L - S_{L+1} A_{L+1} - S_L B_L + S_{L+1} P_{L+1} B_{L+1} = 0 \tag{3.36}$$

Note that since, there is no reflected field in the transmission layer $(m = L+1)$, the vector B_{L+1} will be set to zero in equations (3.35) and (3.36). In equation (3.29), A_0 is the incident field vector at $z = 0$. The above set of equations can be simplified by eliminating $P_m B_m$ from equations (3.29), (3.31), (3.33) up to (3.35), and by eliminating $S_m P_m A_m$ from equations (3.32), (3.34) up to (3.36) while retaining equation (3.30). Thus, we have the new set of equations:

$$-2S_1 A_1 + (S_1 - S_0) B_0 = -(S_1 + S_0) A_0 \tag{3.37}$$

$$-S_1 A_1 - S_0 B_0 + S_1 P_1 B_1 = -S_0 A_0 \tag{3.38}$$

$$(S_1 + S_2) P_1 A_1 - 2S_2 A_2 + (S_2 - S_1) B_1 = 0 \tag{3.39}$$

$$(S_2 - S_1) A_2 + 2S_1 B_1 - (S_2 + S_1) P_2 B_2 = 0 \tag{3.40}$$

$$(S_2 + S_3) P_2 A_2 - 2S_3 A_3 + (S_3 - S_2) B_2 = 0 \tag{3.41}$$

$$(S_3 - S_2) A_3 - 2S_2 B_2 - (S_3 + S_2) P_3 B_3 = 0 \tag{3.42}$$

We proceed in a similar manner for the remaining equations. The last set of equations is thus:

$$\left(S_L + S_{L+1}\right) P_L A_L - 2 S_{L+1} A_{L+1} + \left(S_{L+1} - S_L\right) B_L = 0 \qquad (3.43)$$

$$\left(S_{L+1} - S_L\right) A_{L+1} + 2 S_L B_L = 0 \qquad (3.44)$$

Arranging equations (3.37), (3.38) up to (3.44) in matrix form, with all the unknowns A_i and B_i assembled in a column vector as shown in equation (3.45). The square matrix in equation (3.45) has been sub-divided into four regions in order to improve readability and to make it easier for the reader to relate the different terms in the matrix relation.

$$
\begin{bmatrix}
-2S_1 & 0 & 0 & \cdots & 0 & (S_1-S_0) & 0 & 0 & \cdots & 0 \\
(S_1+S_2)P_1 & -2S_2 & 0 & \cdots & 0 & 0 & (S_2-S_1) & 0 & \cdots & 0 \\
0 & (S_2+S_3)P_2 & -2S_3 & \cdots & 0 & 0 & 0 & (S_3-S_2) & \cdots & 0 \\
\cdots & \cdots & \cdots & \cdots & \cdots & \cdots & \cdots & \cdots & \cdots & \cdots \\
0 & 0 & 0 & (S_L+S_{L+1})P_L & -2S_L & 0 & 0 & 0 & \cdots & (S_{L+1}-S_L) \\
-S_0 & S_1P_1 & 0 & 0 & \cdots & 0 & -S_1 & 0 & 0 & \cdots & 0 \\
0 & 2S_1 & -(S_2+S_1)P_2 & 0 & \cdots & 0 & 0 & (S_2-S_1) & 0 & \cdots & 0 \\
0 & 0 & 2S_2 & -(S_3+S_2)P_3 & \cdots & 0 & 0 & 0 & (S_3-S_2) & \cdots & 0 \\
\cdots & \cdots & \cdots & \cdots & \cdots & \cdots & \cdots & \cdots & \cdots & \cdots \\
0 & 0 & 0 & \cdots & 2S_L & 0 & 0 & 0 & 0 & \cdots & (S_{L+1}-S_L)
\end{bmatrix}
\begin{bmatrix}
A_1 \\ A_2 \\ A_3 \\ \vdots \\ A_{L+1} \\ B_0 \\ B_1 \\ B_2 \\ \vdots \\ B_L
\end{bmatrix}
=
\begin{bmatrix}
-(S_1+S_0)A_0 \\ 0 \\ 0 \\ \vdots \\ 0 \\ -S_0A_0 \\ 0 \\ 0 \\ \vdots \\ 0
\end{bmatrix}
$$

(3.45)

The matrix relation (3.45) can be made computationally more efficient by multiplying it by S_i^{-1} at appropriate positions and by removing the common factors. This results in the following modified matrix relation:

$$
\begin{bmatrix} A_1 & A_2 & A_3 & \cdots & A_{L+1} & B_0 & B_1 & B_2 & \cdots & B_L \end{bmatrix}
$$

$$
\times
\begin{bmatrix}
I & 0 & 0 & \cdots & 0 & \tfrac{1}{2}(S_1^{-1}S_0-I) & 0 & 0 & \cdots & 0 \\
-\tfrac{1}{2}(I+S_2^{-1}S_1)P_1 & I & 0 & \cdots & 0 & 0 & \tfrac{1}{2}(S_2^{-1}S_1-I) & 0 & \cdots & 0 \\
0 & -\tfrac{1}{2}(I+S_3^{-1}S_2)P_2 & I & \cdots & 0 & 0 & 0 & \tfrac{1}{2}(S_3^{-1}S_2-I) & \cdots & 0 \\
\vdots & \vdots & \vdots & \cdots & \vdots & \vdots & \vdots & \vdots & \cdots & \vdots \\
0 & 0 & 0 & \cdots & I & \tfrac{1}{2}(S_{L+1}^{-1}S_L-I) & 0 & 0 & \cdots & 0 \\
S_0^{-1}S_1 & 0 & 0 & \cdots & 0 & I & 0 & 0 & \cdots & 0 \\
0 & \tfrac{1}{2}(S_1^{-1}S_2-I) & 0 & \cdots & 0 & -S_0^{-1}S_1 P_1 & I & 0 & \cdots & 0 \\
0 & 0 & \tfrac{1}{2}(S_2^{-1}S_3-I) & \cdots & 0 & 0 & -\tfrac{1}{2}(S_1^{-1}S_2+I)P_2 & I & \cdots & 0 \\
\vdots & \vdots & \vdots & \cdots & 0 & \vdots & \vdots & -\tfrac{1}{2}(S_2^{-1}S_3+I)P_3 & \cdots & \vdots \\
0 & 0 & 0 & \cdots & \tfrac{1}{2}(S_L^{-1}S_{L+1}-I) & 0 & 0 & 0 & \cdots & I
\end{bmatrix}
$$

$$
=
\begin{bmatrix} \tfrac{1}{2}(I+S_1^{-1}S_0)A_0 & 0 & 0 & \cdots & 0 & A_0 & 0 & 0 & \cdots & 0 \end{bmatrix}
$$

$$(3.46)$$

The unknowns in equation (3.46) are A_i $\left(L+1\geq i\geq 1\right)$ and B_i $\left(L\geq i\geq 0\right)$. Because of the extremely large size of the square matrix in equation (3.46), explicit solution of this equation will be avoided. In addition, the matrix elements of the square matrix are themselves full square matrices, which will not be obtained explicitly in order to maintain relatively low memory usage. An iterative procedure using the BICGSTAB routine will be used to solve for all the unknown in equation (3.46) simultaneously.

3.6. ANALYSIS OF WAVEGUIDE WITH TWO LONGITUDINAL DISCONTINUITIES

The general *PMOL* procedure that accounts for multiple longitudinal discontinuities, which was presented in the previous section, will be demonstrated for a waveguide structure having two longitudinal discontinuities.

Consider the structure shown in Figure 3-14, which has two longitudinal discontinuities, one located at $z=0$ and the other at $z=d=0.5\mu m$. The TE_0 mode of region 0 is assumed to be incident from the left hand side of the structure. In the case of two longitudinal discontinuities, equation (3.46) reduces to the following relation:
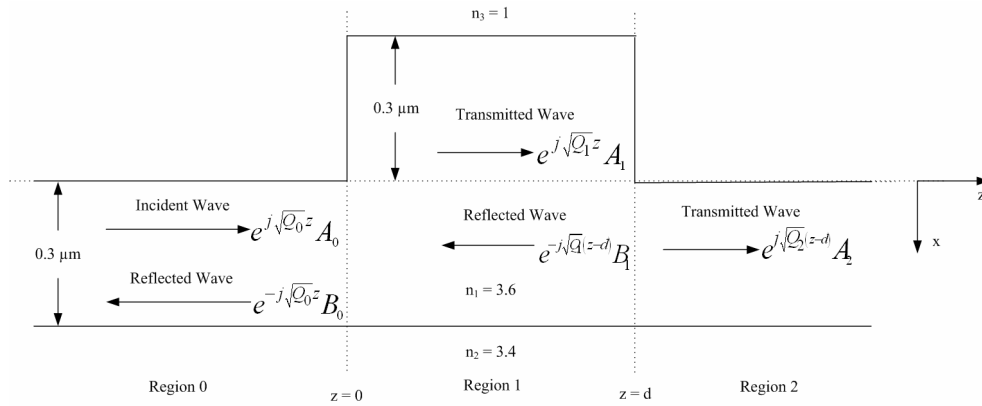
Figure 3-14 Waveguide with two longitudinal discontinuities

$$
\begin{bmatrix}
I & 0 & \frac{1}{2}\left(S_1^{-1}S_0 - I\right) & 0 \\[2ex]
-\frac{1}{2}\left(I + S_1^{-1}S_0\right)P_1 & I & 0 & \frac{1}{2}\left(S_2^{-1}S_1 - I\right) \\[2ex]
S_0^{-1}S_1 & 0 & I & -S_0^{-1}S_1 P_1 \\[2ex]
0 & \frac{1}{2}\left(S_1^{-1}S_2 - I\right) & 0 & I
\end{bmatrix}
\begin{bmatrix}
A_1 \\[2ex] A_2 \\[2ex] B_0 \\[2ex] B_1
\end{bmatrix}
=
\begin{bmatrix}
\frac{1}{2}\left(I + S_1^{-1}S_0\right)A_0 \\[2ex]
0 \\[2ex]
A_0 \\[2ex]
0
\end{bmatrix}
$$

$$(3.47)$$

In equation (3.47), the right hand side vector is known. This vector can be computed once using sparse matrix vector multiply and sparse matrix vector divide as mentioned in section 5.1. On the other hand, the vector on the left hand side of equation (3.47) is unknown. The BICGSTAB subroutine in Matlab environment provides a guess for the value of this unknown vector. Then using the procedures presented in section 5.1 and 5.2, the matrix vector product shown on the left hand side of the equation is performed. This process is repeated until the left and the right hand side are equal. In this case BICGSTAB converges, giving accurate results.

As mentioned earlier, the value of γ will be fixed to a specific value for both the square root and propagation operators. A Padé order of four is used for the square root operator and a Padé order of 10 is used for the propagation operator.

The reflected and the transmitted fields associated with Figure 3-14, (at $\lambda = 1.00 \ \mu m$) were calculated using both the *PBPM* and the *MOL*. The results are shown in Figure 3-15 and 3-16 respectively. The computed fields are seen to be in good agreement with each other.
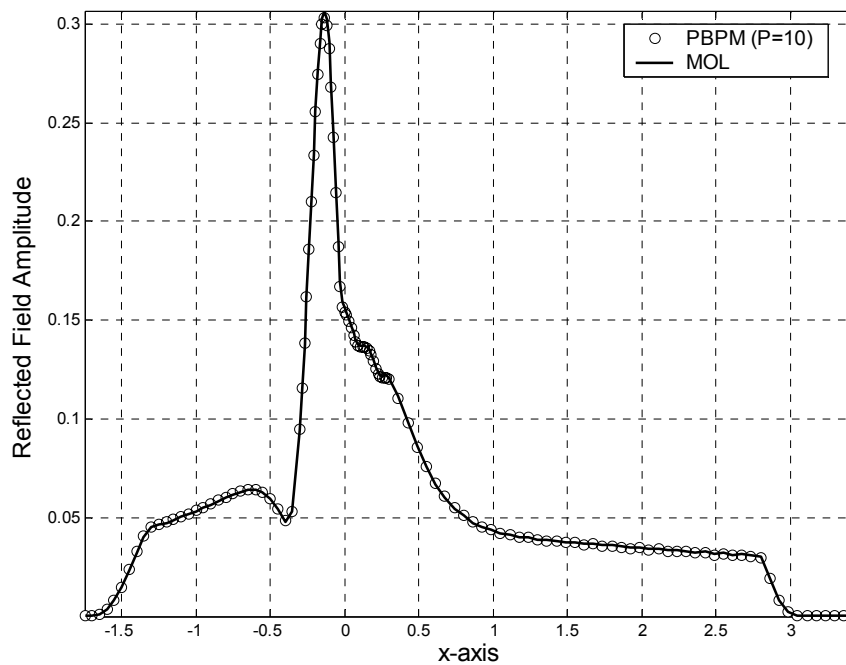
Figure 3-15 Reflected field at z=0 for the double discontinuity waveguide using the PBPM and the MOL
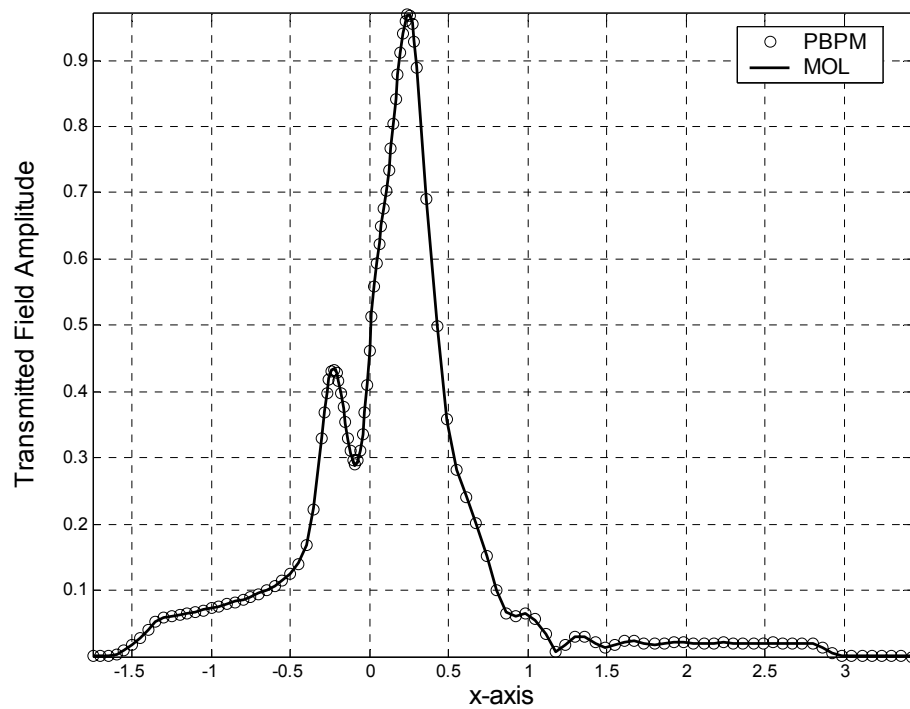
Figure 3-16 Transmitted field at z=d$^+$ for double discontinuity waveguide using PBPM and MOL

In order to verify the accuracy of the generalized procedure further, a multiple discontinuity problem with more than two discontinuities was analyzed. The planar waveguide shown in Figure 3-17 with six longitudinal discontinuities, each 0.5μm apart, was simulated using the same parameters used for the double discontinuity problem considered earlier.
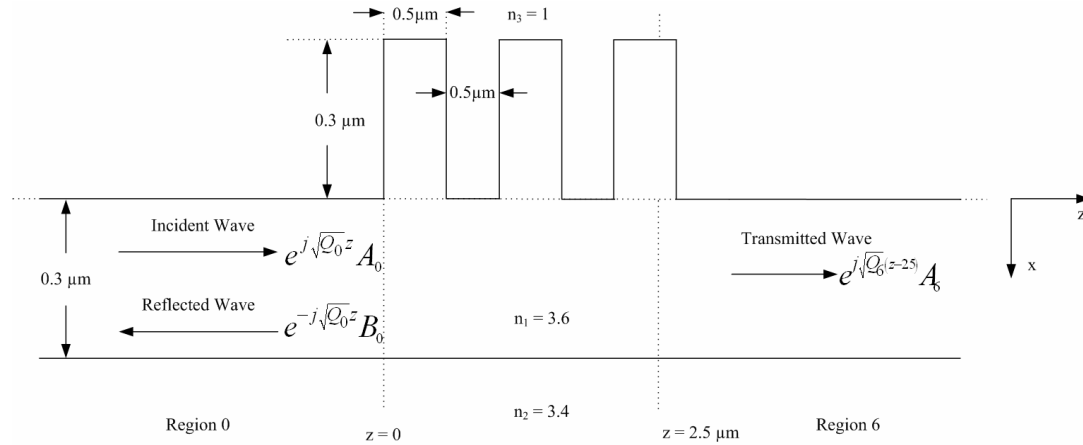
Figure 3-17 Planar waveguide with six longitudinal discontinuities spaced 0.5µm apart.

The generalized *PBPM* and the *MOL* were both used to compute the reflected and the transmitted fields and their results were compared, as shown in Figure 3-18 and 3-19 respectively. There is good agreement between the two methods as can be observed from these two figures.
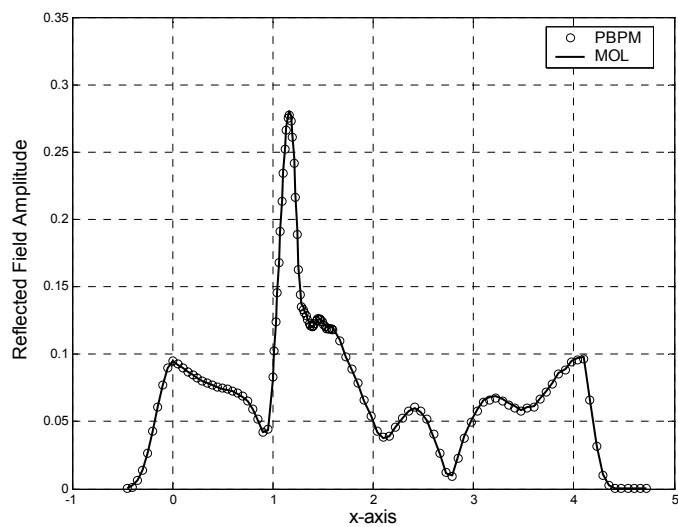
Figure 3-18 Comparison of the reflected field at z=0 for the waveguide with multiple longitudinal discontinuities
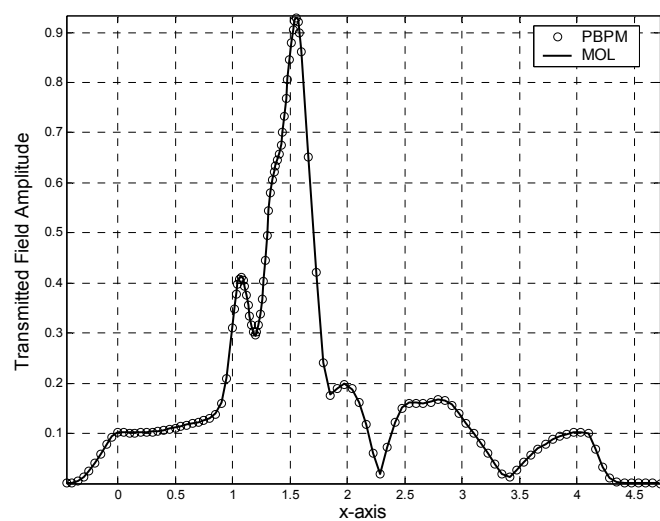
Figure 3-19 Comparison of the transmitted field at z=2.5 µm for the waveguide with multiple longitudinal discontinuities

3.7.   CONCLUSION

In conclusion, it has been seen that the *PBPM* provides results that are very close to the *MOL* calculations, establishing the accuracy of the approach discussed in this chapter. The CPU time requirement of the *PBPM* as compared to the *MOL* is in general, problem dependent. For problems with relatively low number of mesh points (few hundred or less), the *MOL* is faster than the *PBPM* . However, when the number of mesh points exceeds fewer hundred, the *PBPM* becomes faster than the *MOL* . A demonstration of this statement will be shown in the next chapter, when the *PBPM* is applied to a practical problem.

Having developed and validated the general *PBPM* approach, we apply it in the next chapter for the analysis of the beam expander as mentioned in chapter 1.

CHAPTER 4

ANALYSIS OF WAVEGUIDE BEAM EXPANDER

4.1.   INTRODUCTION

In this chapter, we study a simple waveguide junction in the form of a linearly tapered waveguide that connects two waveguide having different core widths, as shown in Figure 4-1. We focus our attention on waveguides with high refractive index contrast. The reflected, transmitted and radiated power associated with this beam expander will be considered.

A major advantage of the general $PBPM$ formulation discussed in the previous chapter is the simulation of guided structures exhibiting many longitudinal discontinuities. The MOL, in general is inefficient when applied to such structures if the reflected, transmitted as well as the field within the structure are of interest. This is due to the large memory storage requirements of the MOL in this particular case. However, the $PBPM$ does not suffer this limitation, because its memory requirements are very low. The study of the linearly tapered waveguide junction will provide us with an opportunity to test the general $PBPM$ approach for this type of problems and compare its results with the MOL based calculations. The linearly tapered junction will be modeled using locally

homogeneous layers based on the staircase approximation scheme, thus treating this problem as a multi longitudinal discontinuity problem.

We will assume that the input power is incident from the narrow waveguide into the wider waveguide, thus we effectively have a beam expander. Both a symmetric and asymmetric beam expanders will be considered in this chapter.

4.2.   SYMMETRIC BEAM EXPANDER

We will first study the symmetric beam expander (see Figure 4-1). As mentioned above, the tapered beam expander will be modeled using the staircase approximation. The input core width w_1 is kept at 0.2 µm which ensures single mode operation for the input waveguide at the operating wavelength $\lambda = 1.55\,\mu m$. The taper is allowed to expand resulting in an output waveguide with a core width of w_2. The tapered section of length t connects cores of the input and the output waveguides. The refractive index of the input waveguide core, the tapered section, and the output waveguide core have the same value of $n = 3.6$. The cladding is assumed to be air throughout. The tapered section is divided into a number of divisions (N_s) in the z-direction using the staircase approximation. The width of each division (dz) is thus $dz = t/N_s$. Initial simulations were done to check the

convergence of the staircase approximation for the tapered section for different values of

N_s and different values of dx, where dx is the transverse mesh size.
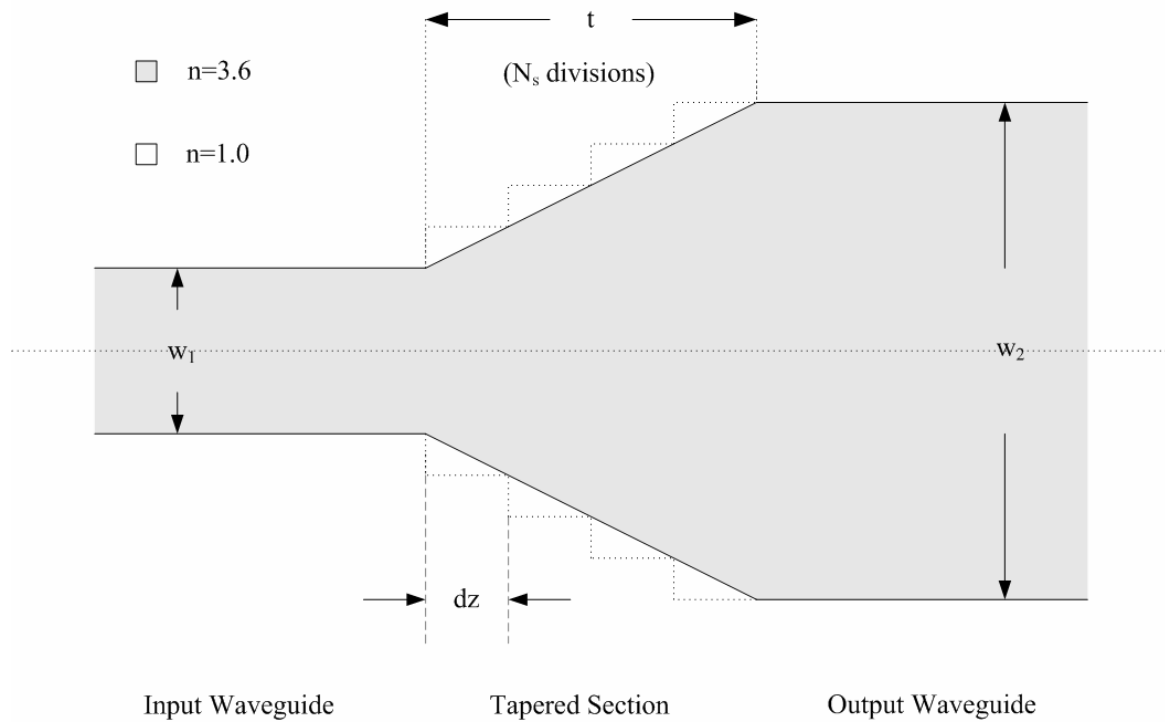
Figure 4-1 A symmetric beam expander

Figure 4-2 shows the modal reflectivity of the symmetric beam expander for

$w_2 = 2$ μm, $t = 2$ μm and $N_s = 25$, for different values of dx. It can be seen in this

figure, that as dx decreases the modal reflectivity converges. Values of $dx < 0.03$ give

convergent results. The structure is then checked for convergence by varying N_s. The

same values of w_2 and t were used with dx fixed to 0.04. Figure 4-3 shows the modal

reflectivity of the symmetric beam expander for different values of N_s. As N_s increases, the results converge. Convergence is obtained for values of $N_s > 18$, implying a proper staircase approximation to the tapered section of the beam expander. In this chapter, $dx = 0.025$ and $N_s = 25$ will be used for the remaining simulations.
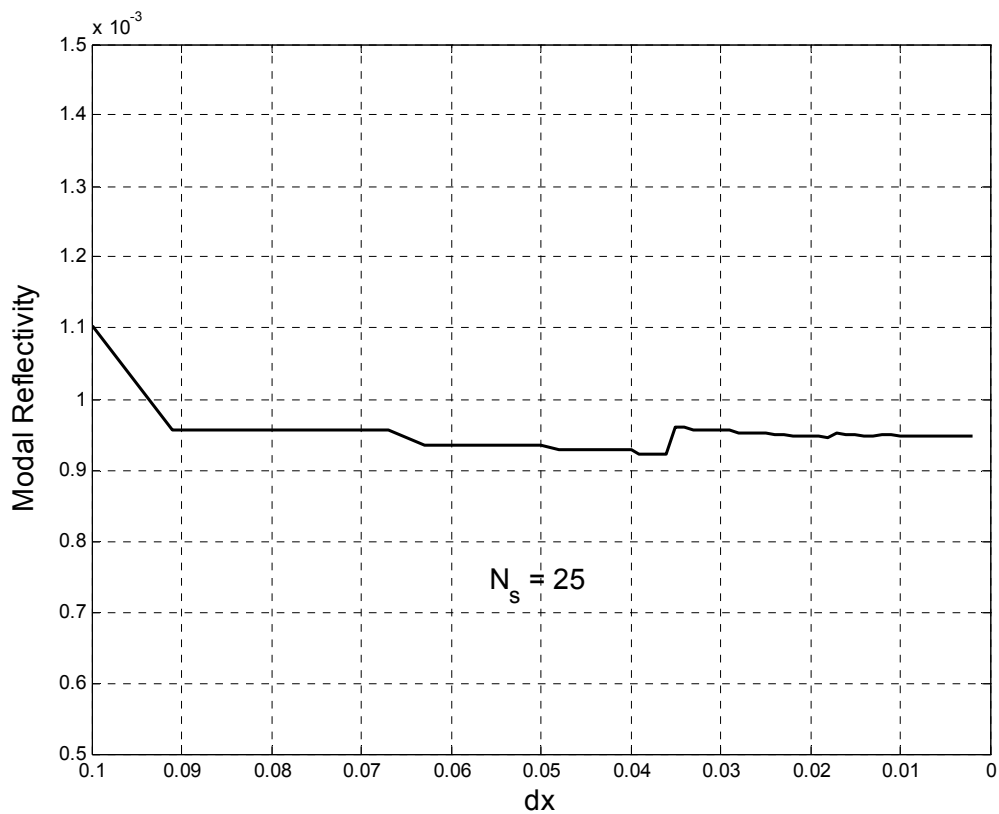
Figure 4-2 Convergence of the modal reflectivity of the symmetric beam expander with dx
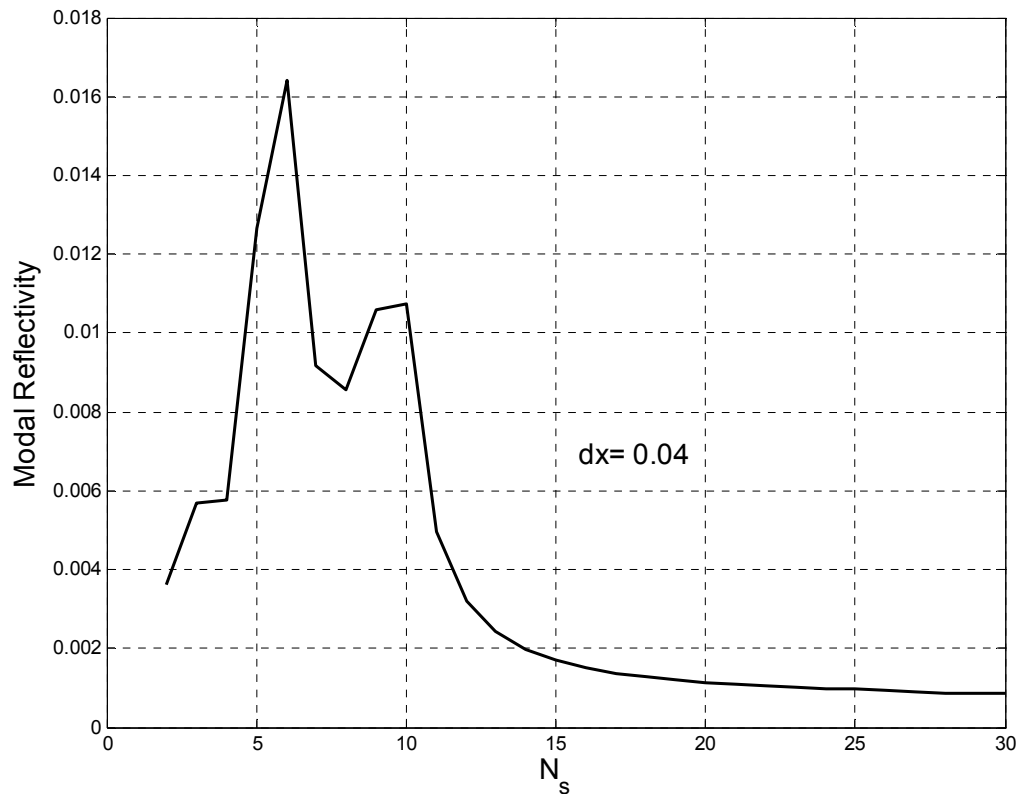
Figure 4-3 Convergence of the modal reflectivity of the symmetric beam expander with N_s

   The behavior of the beam expander was studied by varying its various parameters. The input waveguide core width, as mentioned earlier is fixed to 0.2 μm, and the effect of varying t and w_2 is studied. Firstly, the effect of varying t on the modal reflectivity and the fraction of power transmitted was studied. The output waveguide core width was fixed at $w_2 = 2$ μm in this case.

As can be clearly seen in Figure 4-4, as t increases from zero, the modal reflectivity initially decreases. However, beyond a certain value of t, it starts to increase reaching a peak value near $t = 5.6 \ \mu m$ and then it starts to decrease again.
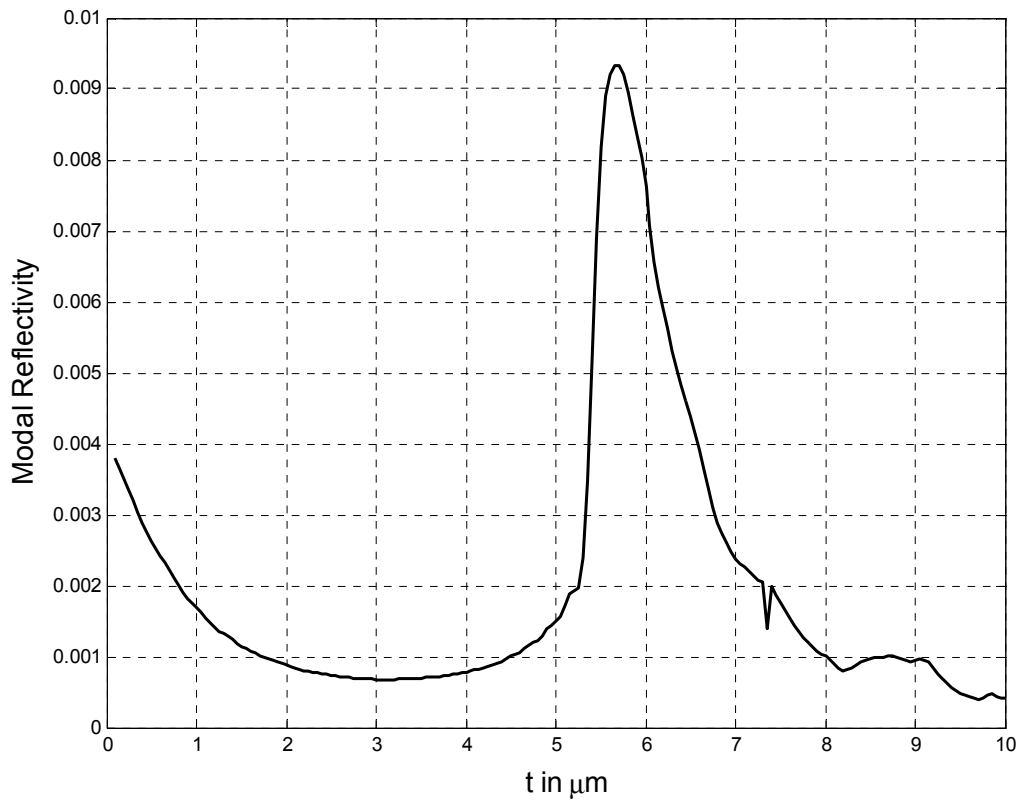
Figure 4-4 Variation of the modal reflectivity of the symmetric beam expander with t

Figure 4-5 shows the fraction of power transmitted versus t. The fraction of power transmitted is fairly constant at around 1 for values of t below 5 μm. However, at few values of t, the fraction of power exceeds 1 by a small amount, which can be ascribed to

slight numerical inaccuracies in the *PBPM* . The fraction of transmitted power exceeds

unity by less than 1 %. It is also seen from this figure that the fraction of power

transmitted starts to decrease as *t* exceeds 5 μm.
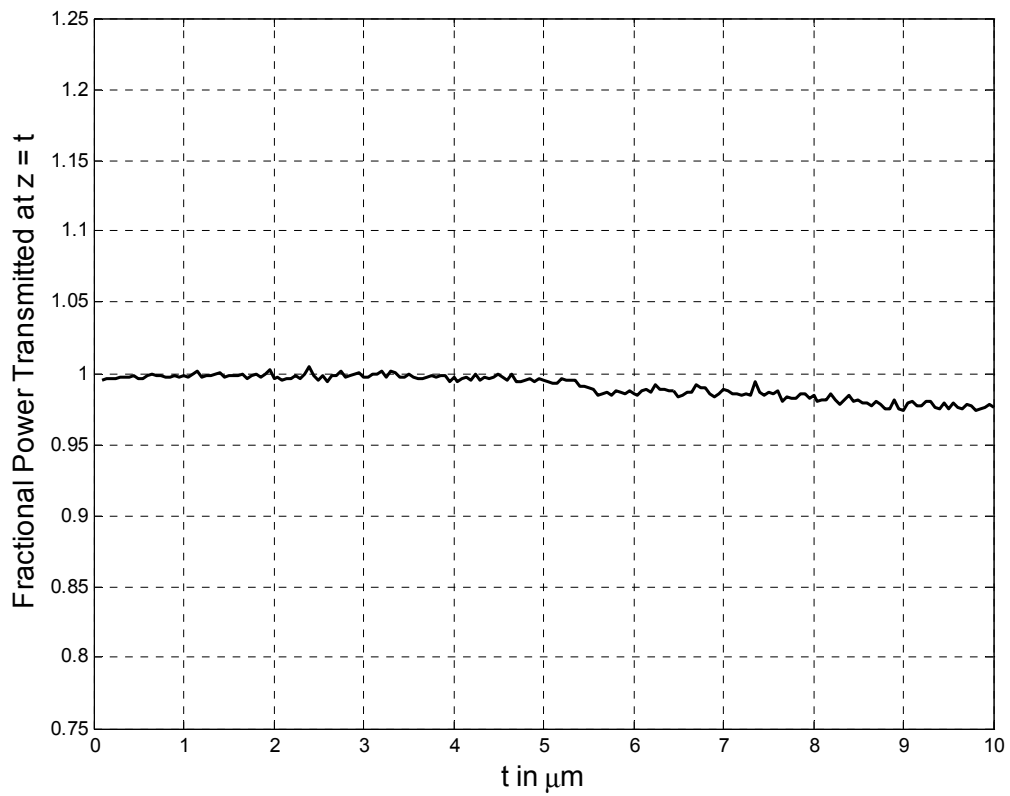
Figure 4-5 Fraction of power transmitted versus t

The fraction of power transmitted in the output waveguide was calculated at

different longitudinal positions along the output waveguide. This was done for various

values of t. the results are shown in Figure 4-6, the fraction of power transmitted is seen to

decrease as we advance along the output waveguide.
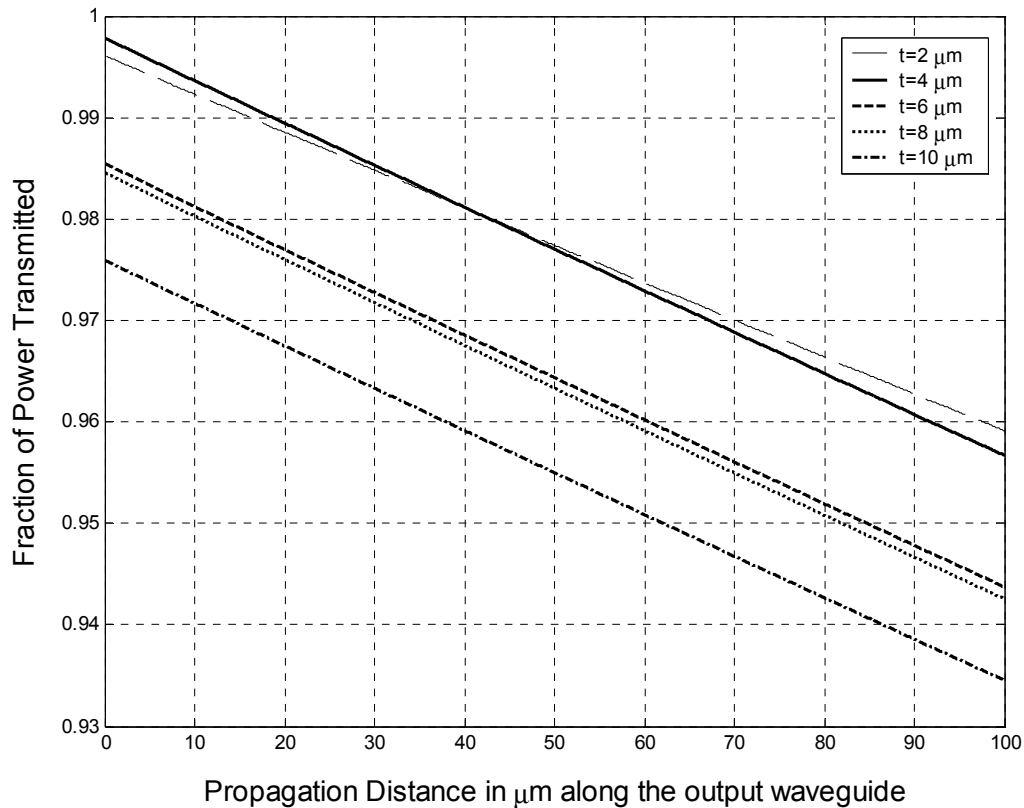
Figure 4-6 Fraction of power transmitted along the output waveguide

The other parameter that was varied is the output waveguide core width w_2 with t

fixed to 2 µm. The modal reflectivities were calculated using both the *PBPM* and the

MOL as shown in Figure 4-7. The modal reflectivity calculated using both methods agree

very well with each other, thus verifying the accuracy of the general *PBPM* for this type

of problem. As can be seen in the figure, the modal reflectivity increases from zero for

$w_2 = 0.2$ μm (equal core widths for the input and the output waveguides $w_1 = w_2 = 0.2$ μm) to approximately 0.004 at $w_2 = 7$ μm and continues to increase as the outer waveguide core width increases.
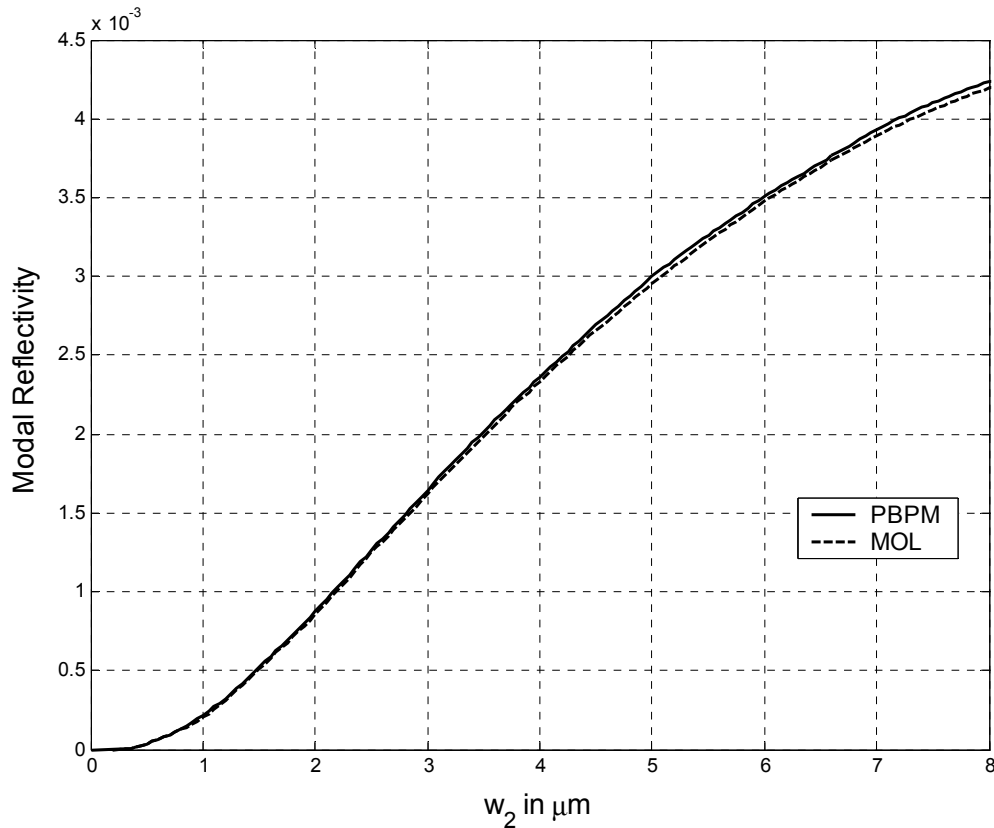
Figure 4-7 Comparison of the modal reflectivities for the symmetric beam expander for different output waveguide core widths w_2 using the PBPM and the MOL

As seen in Figure 4-8, there is no significant variation in the fraction of power transmitted as the outer waveguide core width increases.
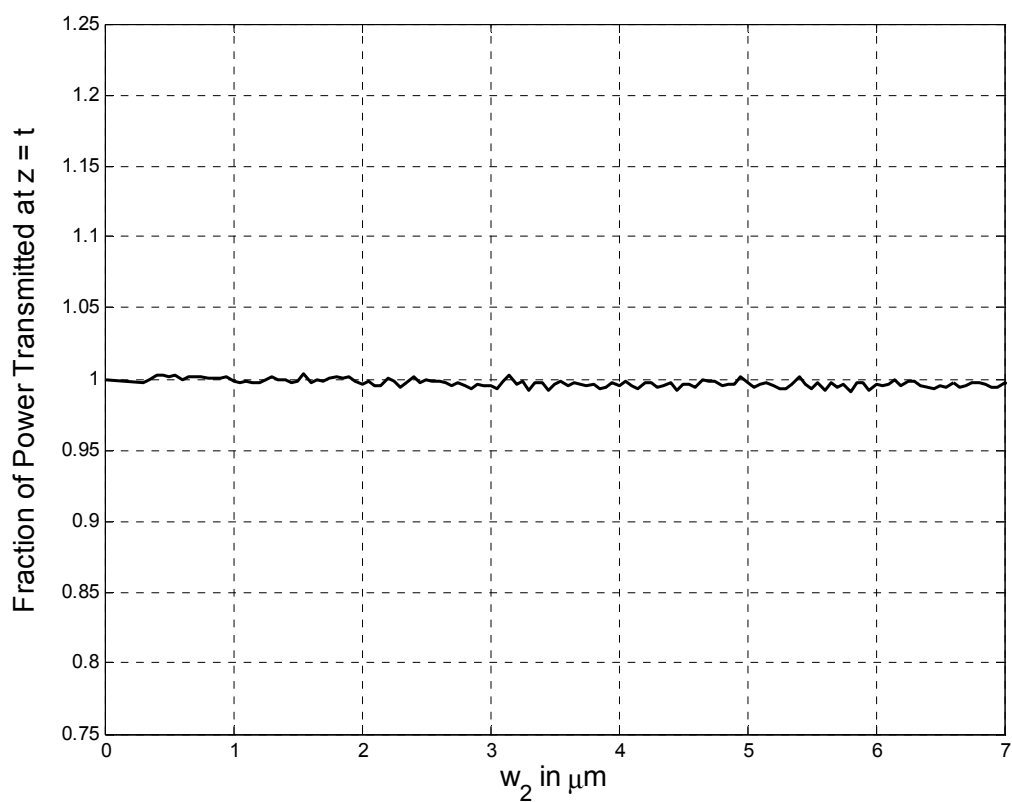
Figure 4-8 Fraction of transmitted power versus the output waveguide core width w_2

Figure 4-9 shows the fraction of power transmitted along the output waveguide, which is seen to decrease linearly with distance along the output waveguide. However, even after a sufficiently long distance, the power drop is in the range of 2-4 % only.
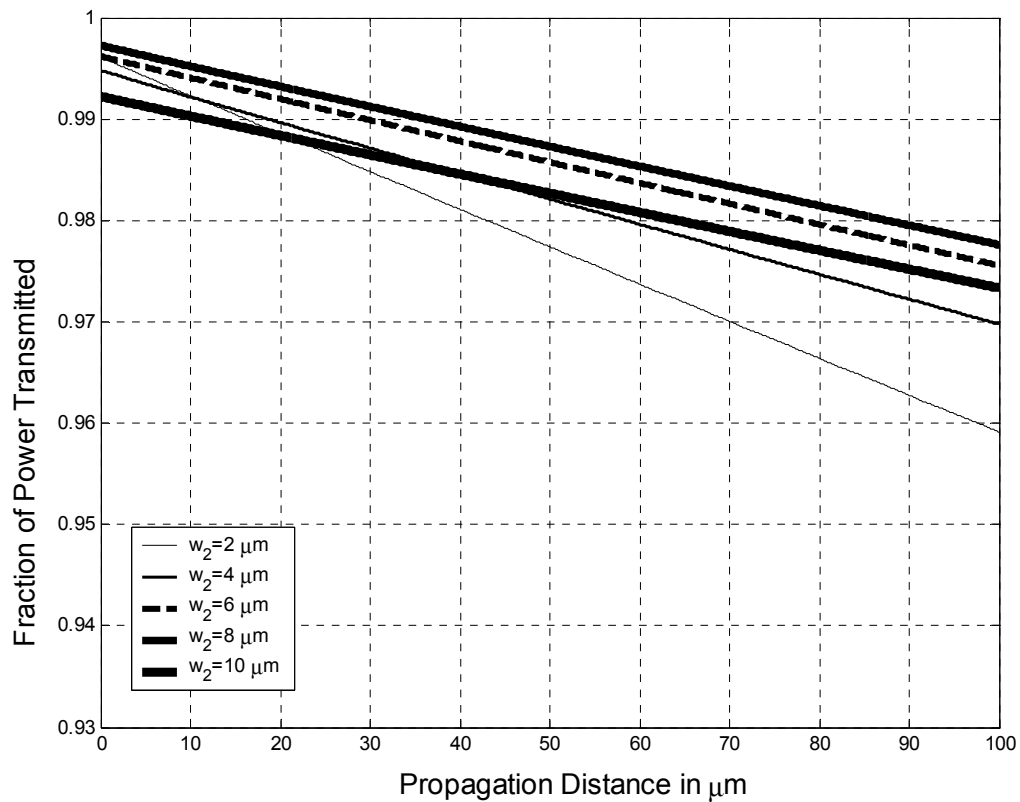
Figure 4-9 Fraction of power transmitted along the output waveguide

The computational time required by the *PBPM* and the *MOL* for the waveguide with a single longitudinal discontinuity was demonstrated in chapter 3. However, the problem of the single discontinuity requires less computational time. This is due to two reasons. Firstly, the propagation operator is not required in this case and secondly, the BICGSTAB requires more iterations, in general, for multi-discontinuity problems. In order to illustrate the efficiency of the general *PBPM* over the *MOL* in the case of multiple longitudinal discontinuities, the two methods were compared with respect to the

computational time required in the analysis of the symmetric beam expander. As mentioned earlier, N_s and dx are fixed at 25 and 0.025 respectively. Thus, increasing w_2 implies an increase in the number of discretization points. This is more evident from the relation $M = \dfrac{w_2}{N_s \times dx}$, where M is the number of transverse discretization points. Thus increasing w_2 results in higher discretization points.

The layer by layer approach was used in the *MOL* in such a manner so that the memory requirement by the *MOL* is minimized. By doing so, the *MOL* was constrained to computing only the reflected field, without computing the fields inside the structure or the transmitted field. However, in the *PBPM* case, the reflected field and more importantly the field within the structure and the transmitted field were computed.

Figure 4-10 shows the computational time requirements for both the *MOL* and the general *PBPM* versus the number of discretization points M. As can be seen, when M is small, the *MOL* requires a smaller computational time than the general *PBPM*. At $M \approx 350$, the computational time required by both of these approaches is almost the same. However, as M increases further, clearly the general *PBPM* becomes faster than the *MOL*. The computational time requirements of the *MOL* is seen to be proportional to M^3, which fits the cubic interpolation shown in the same figure. Whereas, the general

PBPM is seen to increase only linearly with M which fits the linear interpolation, also shown in the Figure 4-10.
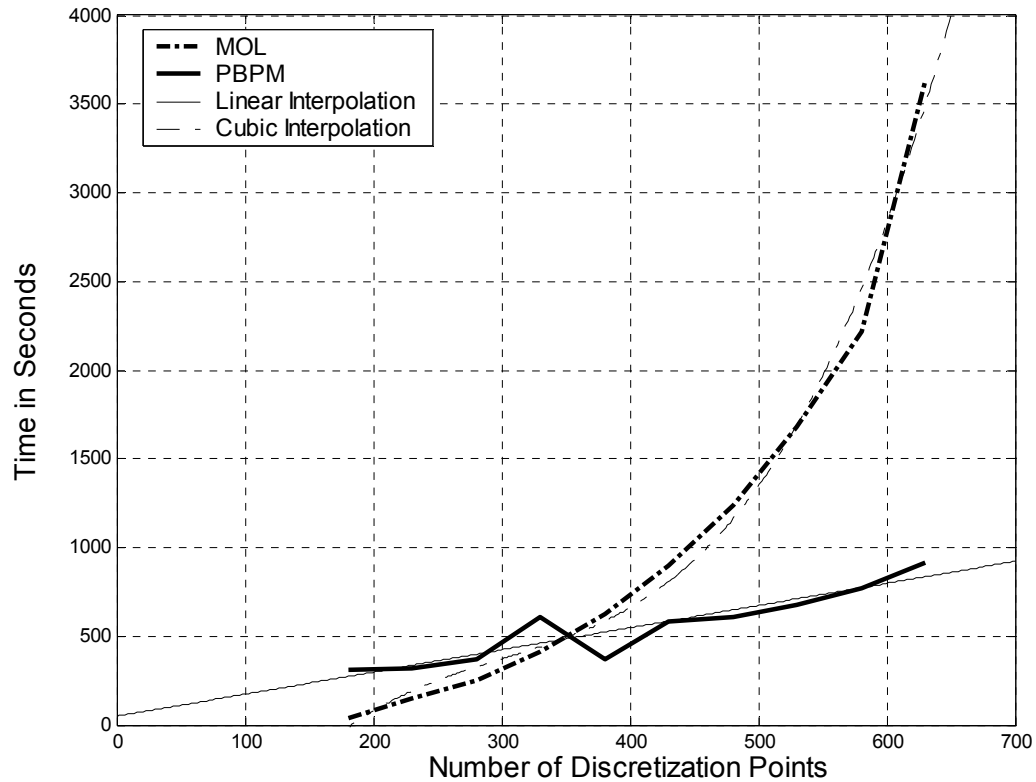
Figure 4-10 Comparison of the computational time requirement by the PBPM and the MOL for the symmetric beam expander.

At $M = 630$, the general *PBPM* is about four times faster than the *MOL*, thus establishing its higher efficiency as compared to the *MOL* for large values of M. It is also obvious that as M increases further, the *PBPM* becomes much more efficient than the *MOL*. Comparison of the time required by the two methods for $M > 630$ was not

done, because the *MOL* becomes exceedingly slow and it almost exhausts the computer memory available. However, the time requirement of the *PBPM* continues to increase linearly and can easily obtain the required results for much higher values of M.

The symmetric waveguide structure shown in Figure 4-1 is studied with the input being fed from the wider waveguide as shown in Figure 4-11. The output core width is fixed at $w_1 = 0.2\mu m$ and the effect of varying t and w_2 is studied.
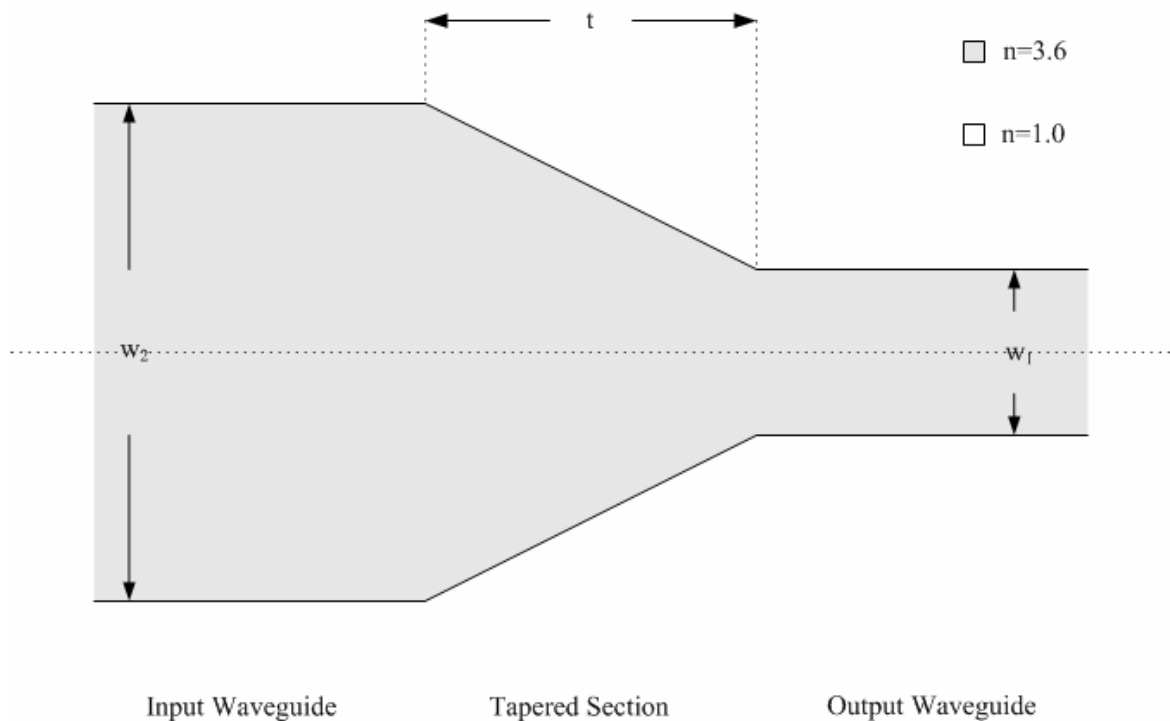
Figure 4-11 Symmetric tapered waveguide structure with wide input waveguide and narrow output waveguide.

Firstly, the modal reflectivity and the modal transmissivity were studied by varying t while fixing w_2 at 2 μm. As can be seen in Figure 4-12, the modal reflectivity has a peak value of $\simeq 0.26$ at $t \simeq 0.9\mu m$. Beyond this peak, the modal reflectivity generally becomes a decreasing function of t. The modal transmissivity shown in Figure 4-13 generally increases with t and remains fairly constant at approximately 0.97 for $t > 5\mu m.$.
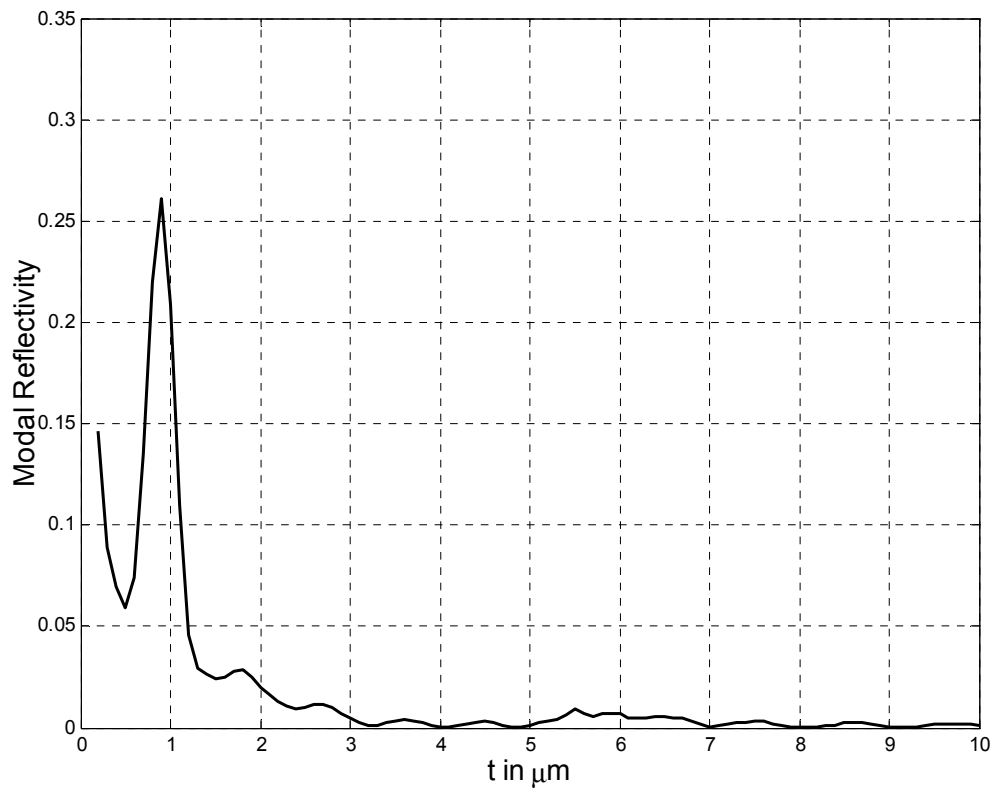
Figure 4-12 Variation of modal reflectivity with t
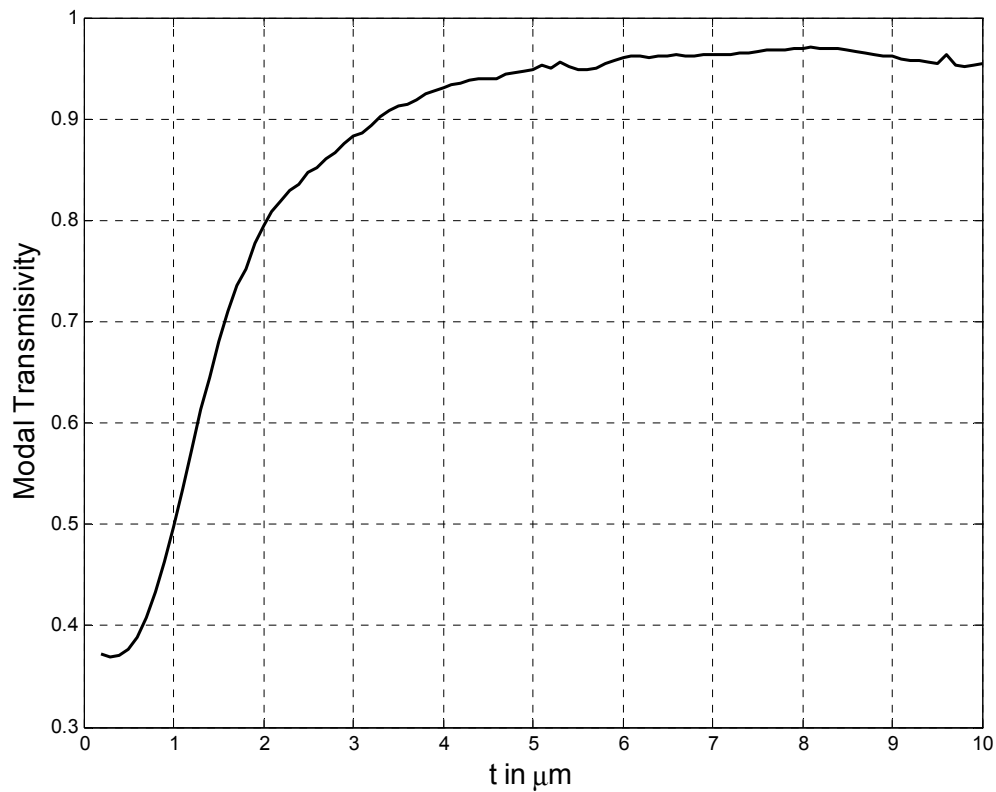
Figure 4-13 Modal Transmissivity versus t

With t fixed at 2 μm, the input waveguide core width w_2 is varied. Figure 4-14 shows the modal reflectivity versus w_2. Initially the modal reflectivity increases with w_2, reaching a peak value of ≈ 0.57 at approximately $w_2 = 4.2 \mu m$. Beyond this peak, the modal reflectivity decreases with w_2, reaching very low values beyond $w_2 \approx 6 \mu m$. The modal transmissivity shown in Figure 4-15, is generally a decreasing function of w_2. However, the modal transmissivity remains high for $w_2 \leq 1.0 \mu m$.
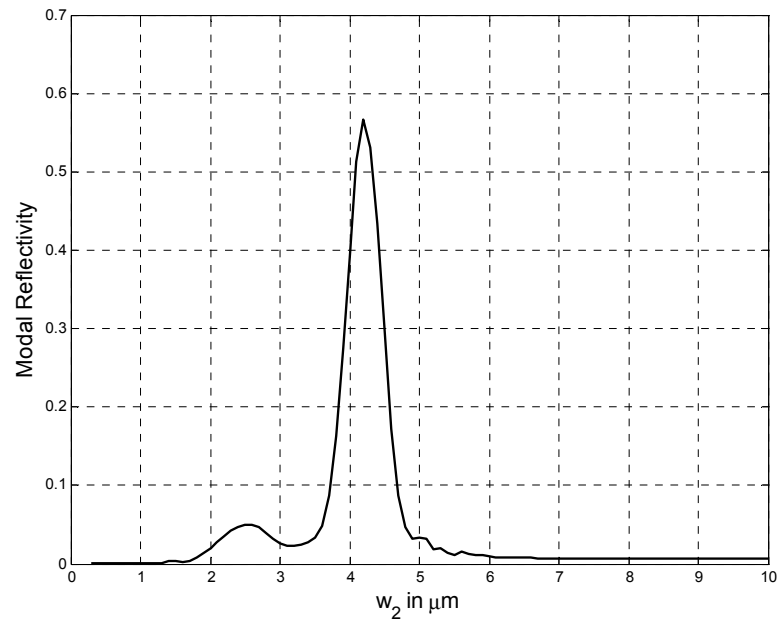
Figure 4-14 Modal reflectivity versus w_2
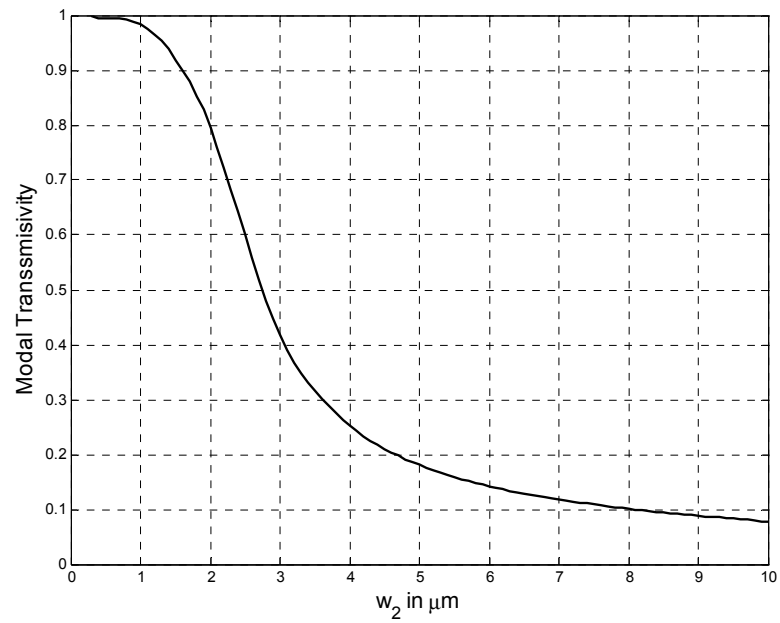
Figure 4-15 Modal Transmissivity versus w_2

4.3.   ASYMMETRIC BEAM EXPANDER

Consider the asymmetric beam expander shown in Figure 4-16. The input and output waveguide cores have a refractive index of 3.6 and are surrounded by air throughout. The widths of the input and the output waveguide cores are taken to be 0.2 μm and 2 μm, respectively. The length t of the tapered section is fixed at 2 μm. The position of the output waveguide core, is kept fixed while the core of the input waveguide is moved vertically away from the line of symmetry. The lower end of the output waveguide core is taken as the reference axis and the input waveguide is shifted upwards. The resulting displacement is denoted as d. The structure becomes symmetric when $d = 0.9$ μm. The values $N_s = 25$ and $dx = 0.025$ were used because they lead to convergent results.
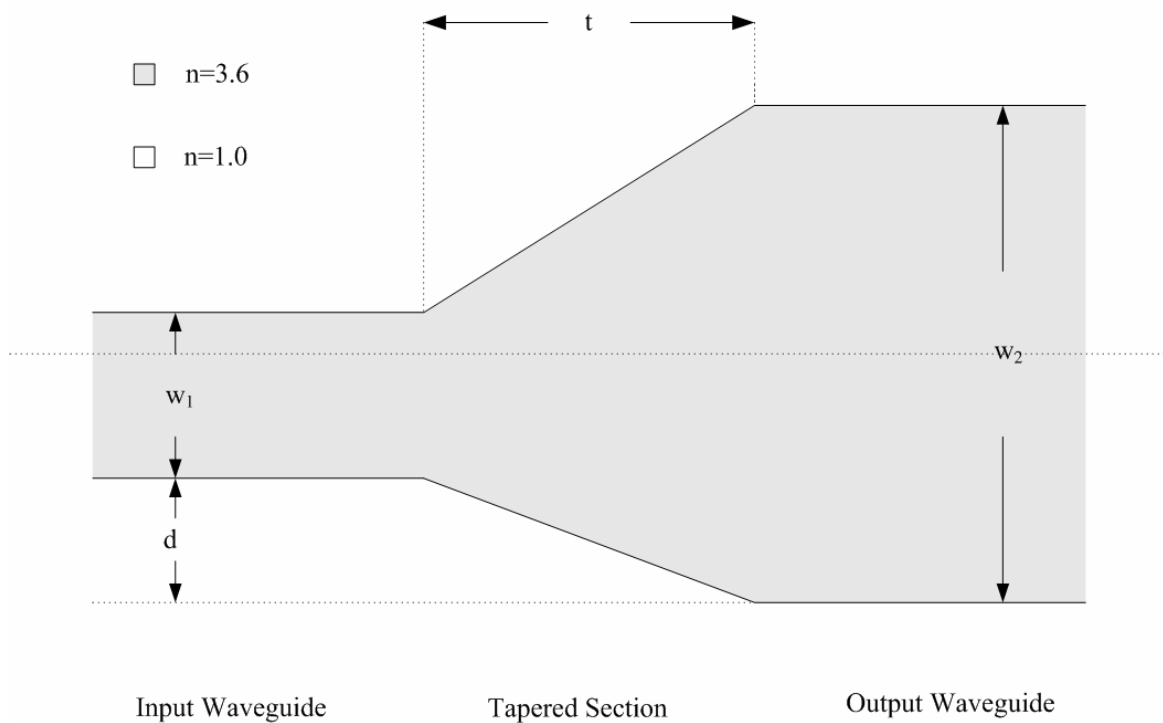
Figure 4-16 An asymmetric beam expander

This beam expander is analyzed by varying d. Figure 4-17 shows the modal reflectivity of the beam expander for different values of d. As can be seen in the figure, as d increases from zero, the modal reflectivity also increases and reaches a peak value of approximately 8.8×10^{-4} at $d=0.9$ μm. which corresponds to the value of the modal reflectivity for $w_2 = 2$ μm in Figure 4-7. This means that maximum modal reflectivity occurs, when the beam expander becomes symmetric.

Figure 4-18 shows the fraction of power transmitted for different values of d. The fraction of power transmitted is fairly constant at about 1.
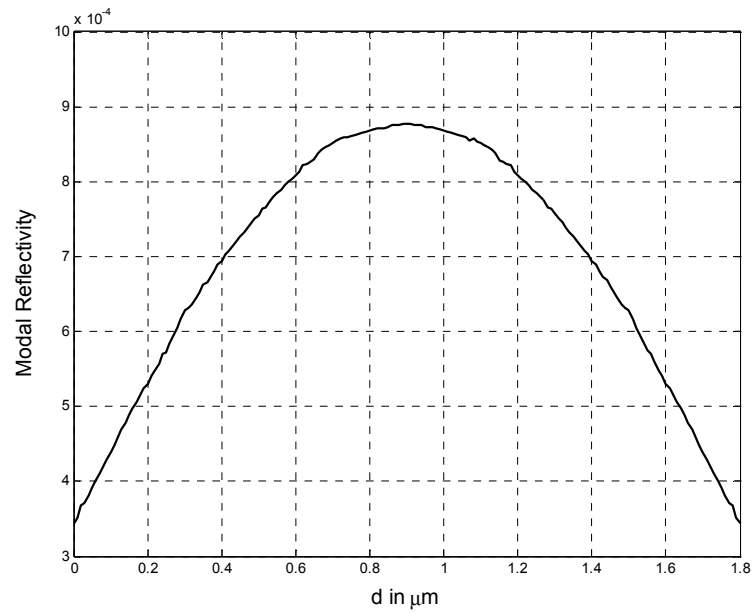
Figure 4-17 Modal reflectivity of the asymmetric beam expander versus d
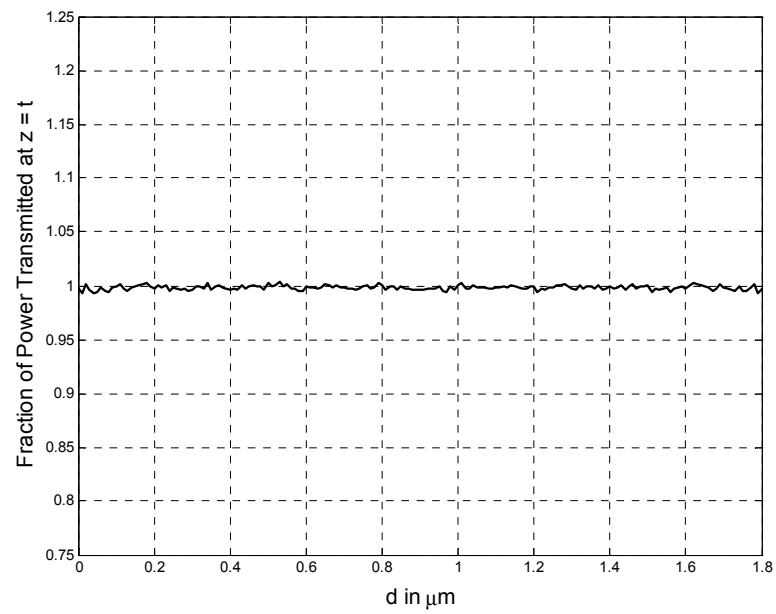
Figure 4-18 Fraction of power transmitted for the asymmetric beam expander versus d

4.4.   SPECIAL CASE OF THE ASYMMETRIC BEAM

EXPANDER

We next analyze a special case of the asymmetric beam expander. As shown in Figure 4-19, the lower boundaries of the input and the output waveguide cores are aligned, resulting in a one-sided linearly tapered beam expander. The width of the input waveguide core is fixed at 0.2 μm. The beam expander is then analyzed by varying t.
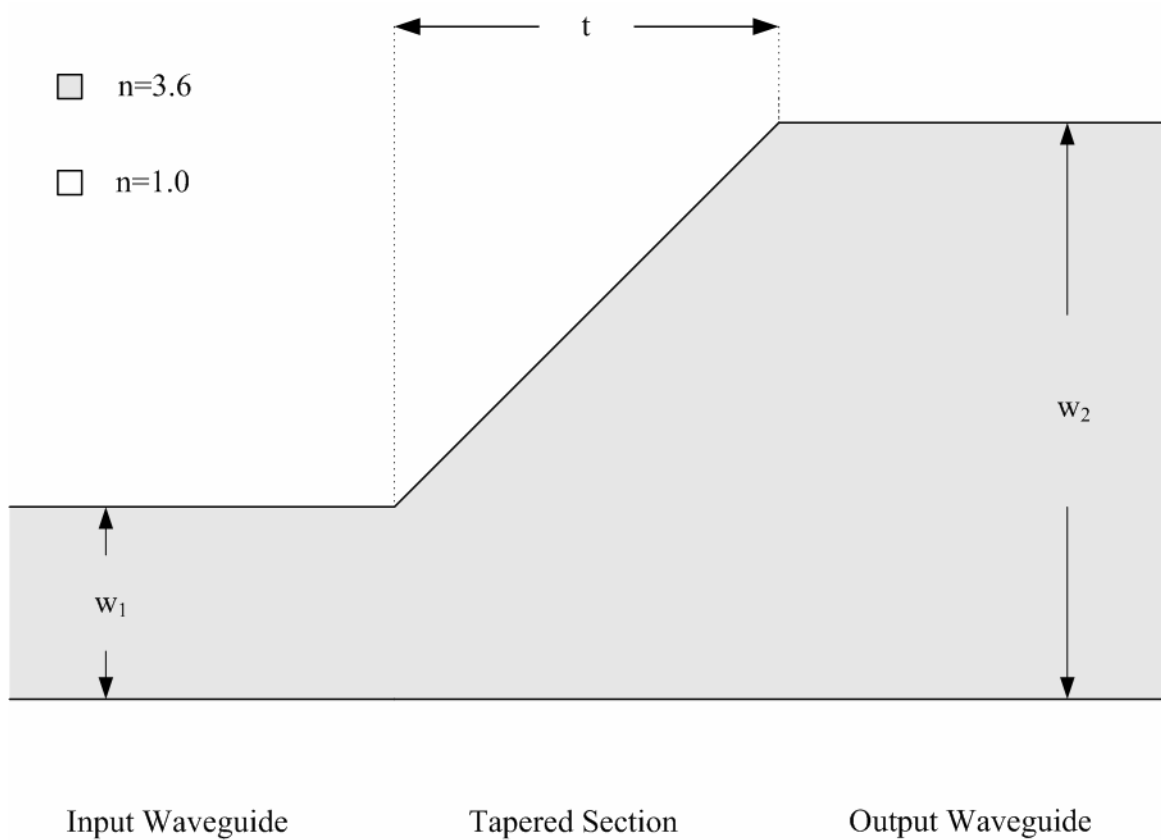
Figure 4-19 A one-sided linearly tapered beam expander

The output waveguide width w_2 was kept fixed at 2 μm and t was varied. Figure 4-20 shows the modal reflectivity versus t. The modal reflectivity is in general low. However, it reaches a peak value of approximately 8.8×10^{-3} when $t = 5.7$ μm. The fraction of power transmitted is also fairly constant up to $t < 5.7$ μm and then it decreases as shown in Figure 4-21.

Figure 4-22 shows the fraction of power transmitted along the output waveguide for various values of t. It can be seen in the figure that the transmitted power decreases with both t and the propagation distance along the output waveguide.
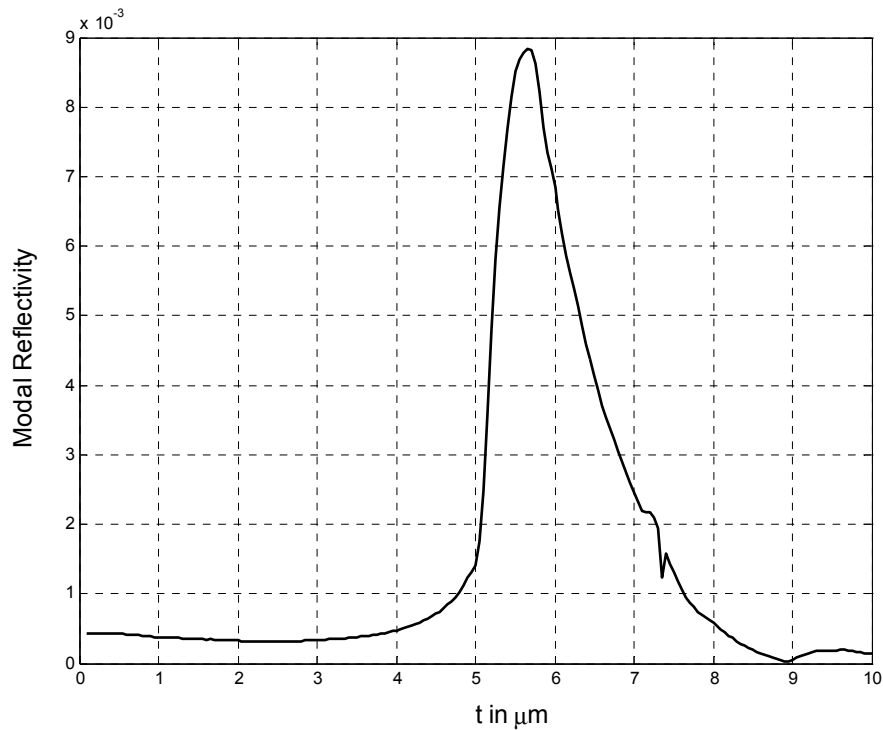
Figure 4-20 Modal reflectivity of the one-sided linearly tapered beam expander versus t
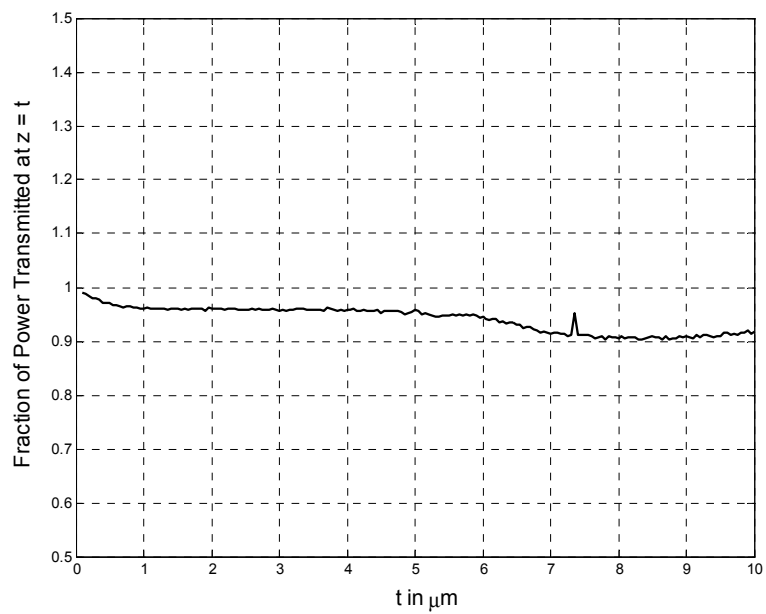
Figure 4-21 Fraction of power transmitted versus t
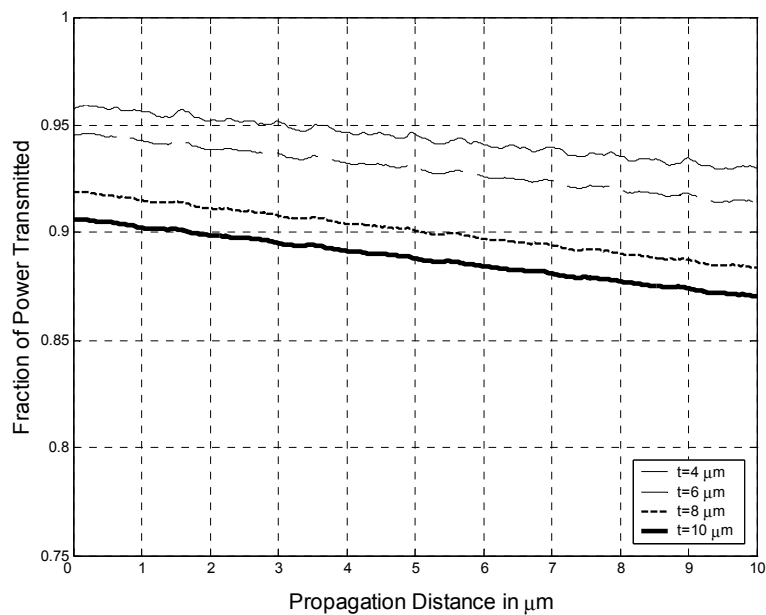
Figure 4-22 Fraction of power transmitted along the output waveguide

The behavior of the one-sided beam expander was analyzed for different values of w_2. The results are almost similar to those of the symmetric beam expander, and thus the results will not be shown here.

4.5.   CONCLUSION

In this chapter, we have demonstrated the efficiency of the general $PBPM$ approach when applied to a multi-discontinuity problem. The linearly tapered beam expander was modeled using the stair-case approximation, thus giving rise to a multi-discontinuity situation. The performance of the general $PBPM$ and the MOL were compared. Even for a constraint MOL routine based on the layer by layer approach, the $PBPM$ is seen to be more computationally efficient, when the number of transverse mesh points is relatively large. The time requirement of the MOL was seen to be proportional to M^3, while the general $PBPM$ time requirement is proportional only to M.

For the case of the symmetric beam expander, it is observed that any value of t (length of the tapered section) less than 5 μm results in low modal reflectivity and high fraction of power transmitted in the output waveguide. Whereas, increasing t further results in higher modal reflectivity and reduces the fraction of power transmitted in the output waveguide. A similar behavior was observed for the case of the asymmetric beam expander. However, the modal reflectivity continuously increases as the output waveguide core width w_2 increases for both the symmetric and asymmetric beam expanders. The

fraction of power transmitted in the output waveguide, in general decreases as we advance long the output waveguide. From the analysis of the asymmetric beam expander, it can be concluded that maximum modal reflectivity occurs when the beam expander is symmetric along the horizontal axis. However, the fraction of power transmitted is lower than that associated with the symmetric beam expander.

When the input optical power is incident from the wide waveguide side of the beam expander, the structure has a completely different response. When compared to the response of the same device when excited from the narrow waveguide side.

CHAPTER 5

ANALYSIS OF WAVEGUIDE CROSSINGS

5.1.   INTRODUCTION

Waveguide crossings (WC) are integral part of any optical integrated circuit, because they are essential for realizing complex optical integrated circuit designs. The main criterion in designing the junction is the ability of the structure to couple negligibly small power from one waveguide into the other thus minimizing crosstalk. The term crosstalk is defined as the undesirable power that is coupled to the other waveguide. The other design criterion is of optical symmetry of the structure on all four sides of the waveguide crossing. In a simple waveguide crossing, the two waveguides are made to intersect directly. This results in a relatively large amount of optical power being reflected back into the input waveguide. In addition, an undesirably high crosstalk results in this case and the resulting transmitted power is relatively low. Thus, the simple waveguide crossing needs to be modified to avoid these undesirable effects.

In addition to analysis of the waveguide crossing, this structure will give us an opportunity to test the $PBPM$ in the situation where optical $guided$ fields in the vertical (transverse direction) are encountered. The $PBPM$ has not been tested for accuracy or convergence in this unique situation.

87

5.2. A SIMPLE 90-DEGREE CROSSING

The structure shown in Figure 5-1 is a simple four way 90-degree symmetric waveguide crossing. The two waveguides directly cross each other and have the same core width $w_c = 0.2\ \mu m$ and the same core refractive index $n = 3.2$. The waveguide core is surrounded by air. This insures single mode operation for TE polarized waves in the entire wavelength range under consideration.
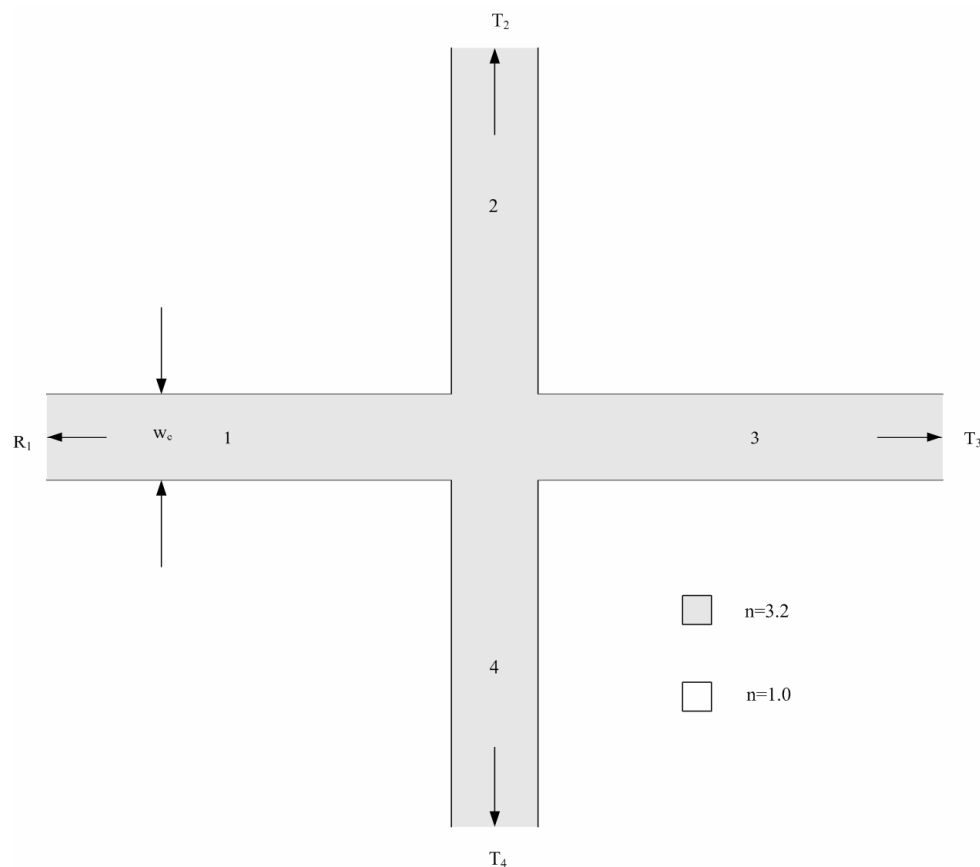
Figure 5-1 A simple 90^0 waveguide crossing

Ideally, when two waveguides cross each other, they should not affect each other. That is to say, the reflected power back into the input waveguide should be zero, the crosstalk should be zero and all the input power should be transmitted (i.e. all the input optical power should remain in the input waveguide). This ideal situation, as we will see shortly is not even nearly achievable by the simple waveguide crossing depicted in Figure 5-1. However, this simple waveguide crossing will be analyzed in order to establish useful reference values. The modal reflectivity in the left arm(input arm) is denoted as R_1, the modal transmissivity in the right arm is T_3, the crosstalk in the upper and the lower arms are denoted as T_2 and T_4, respectively.

The left arm of the WC is excited by the TE_0 mode of the waveguide. The spectral response of the structure is then calculated over the wavelength range 1.48-1.62 μm. As seen in Figure 5-2 the modal reflectivity (R_1), which is clearly undesirably high, is in the approximate range 0.015-0.03. The modal reflectivity is also seen to increase with wavelength. This value of R_1 may seem to be somewhat low. However, in some applications it may prove to be undesirably high.

The crosstalk $(T_2$ and $T_4)$ are computed using the following procedure. The field samples are collected at specific intervals (dz) along the propagation axis (z-axis), sufficiently far from the center of the waveguide crossing in the transverse direction (x-axis) as shown in Figure 5-3. In addition, the analytically available TE_0 mode pattern

along the z-direction is discretized at the same points used in the sample field. Finally, overlap integration is calculated using these two field samples in order to calculate the crosstalk.
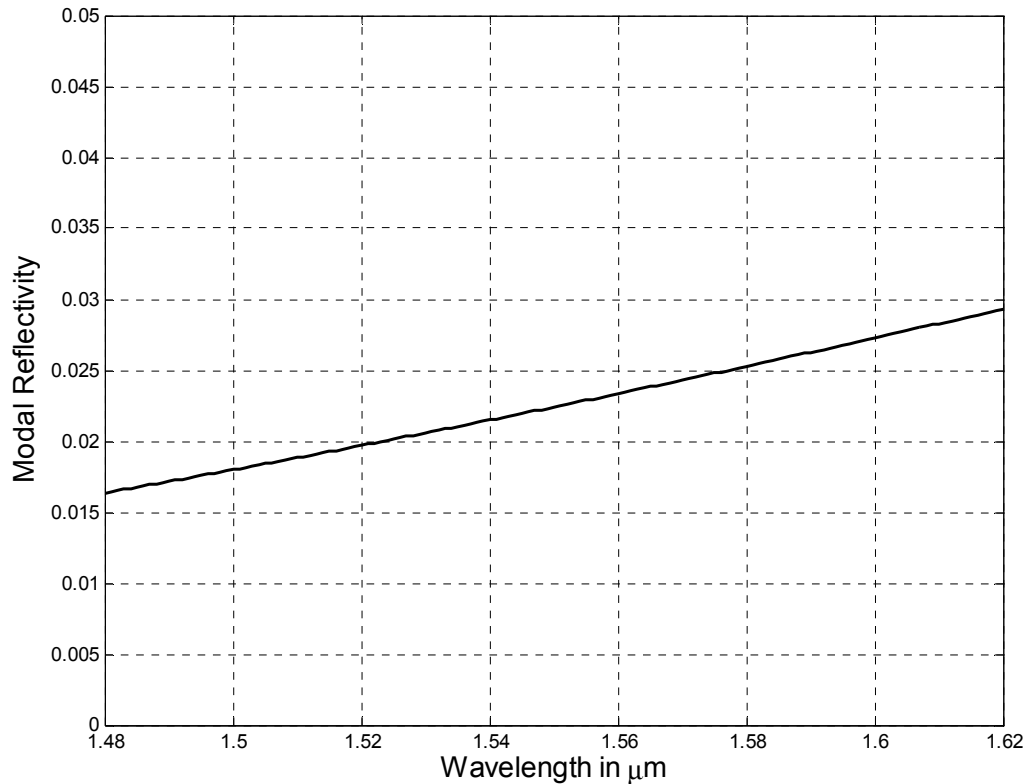
Figure 5-2 Modal reflectivity in the simple waveguide crossing

The crosstalk level is shown in Figure 5-4. Because of structural symmetry, the crosstalk levels $(T_2 \text{ and } T_4)$ in the upper and lower vertical arms, respectively, are identical to each other and thus only one crosstalk level is depicted in Figure 5-4. The value of $T_2 = T_4$ is about 0.07, which is clearly undesirably high. The modal

transmissivity T_3 is approximately 0.83 as can be seen in Figure 5-5. It can be seen that T_3

is substantially independent of λ over the range of the figure. The fraction of radiated

power due to the *WC* is shown in Figure 5-6. The figure shows that only a small fraction

of the input optical power is lost to radiation. This power generally decreases with

wavelength, as seen in Figure 5-6.
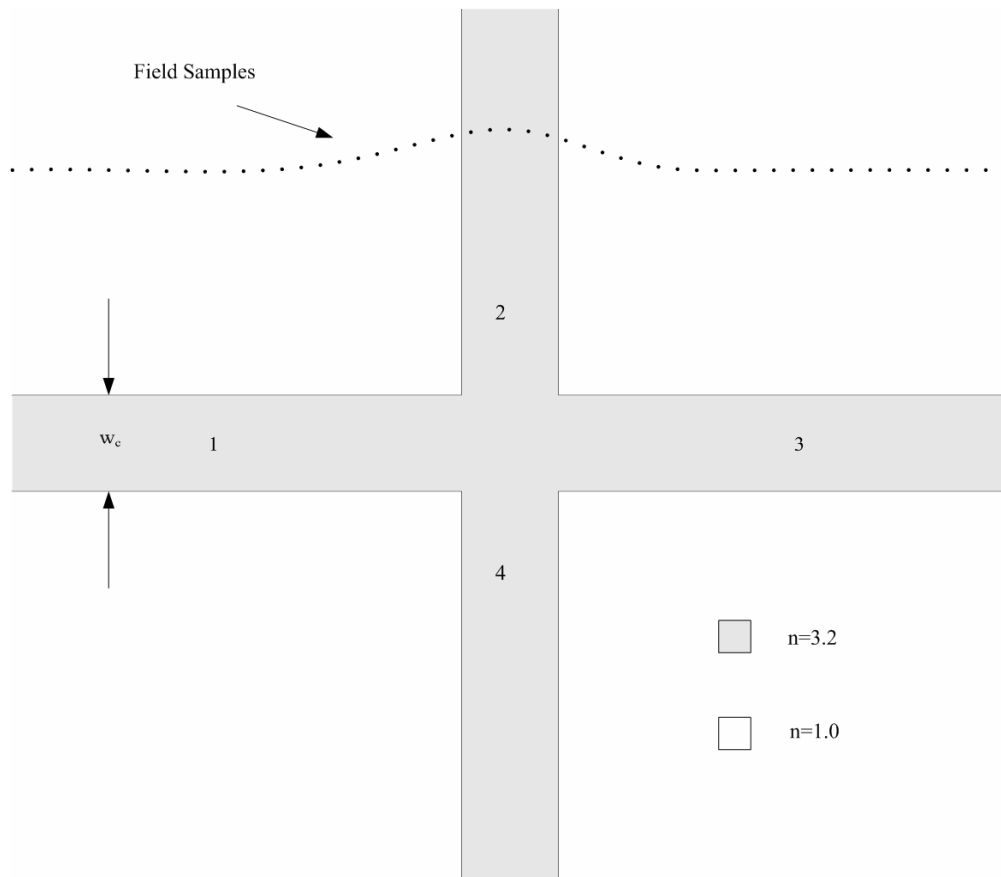
Figure 5-3 Simple waveguide crossing
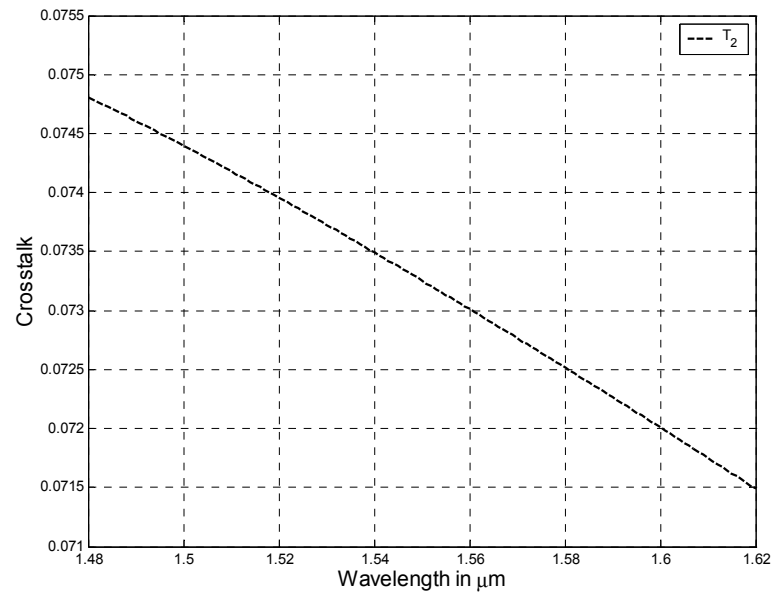
Figure 5-4 Crosstalk in a simple waveguide crossing
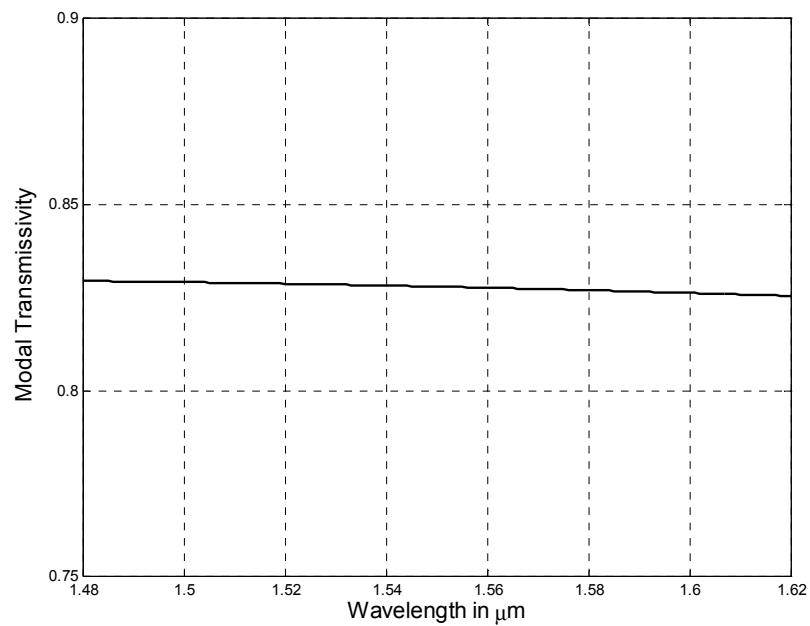
Figure 5-5 Modal transmissivity in a simple waveguide crossing
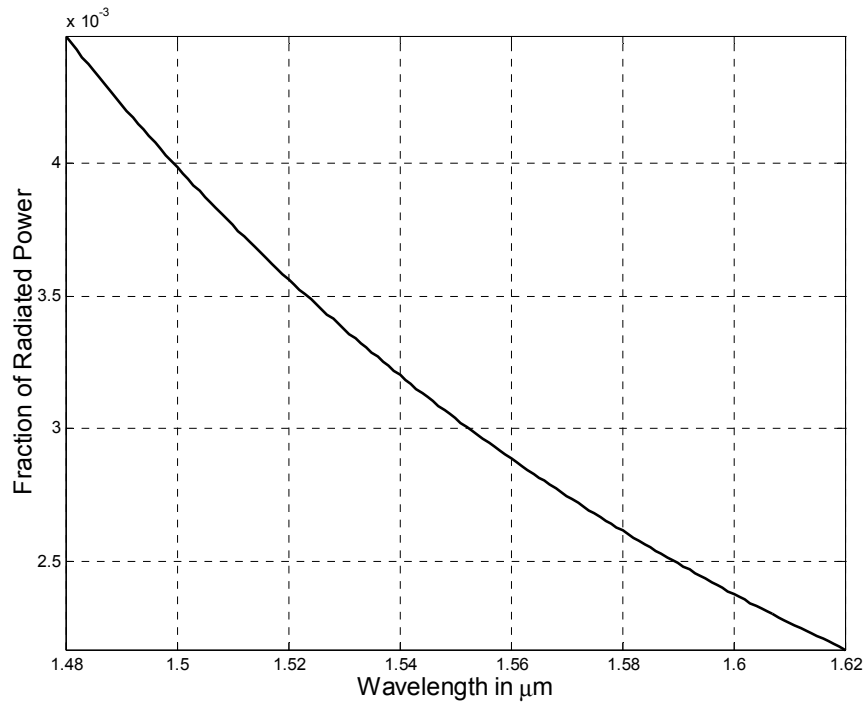
Figure 5-6 Fraction of radiated power in the simple waveguide crossing

5.3.   WAVEGUIDE CROSSING WITH SQUARE RESONANT

CAVITY

In order to transmit maximum power with minimum reflection and minimum crosstalk the simple *WC* is modified at the junction. Instead of joining all the four arms directly, the four arms are coupled using a resonant cavity as shown in Figure 5-7 [62, 63]. The square cavity shown in Figure 5-7 has the same refractive index as the waveguide core and it is separated from the four arms by a small air gap of width a_g. If

the size of the square cavity (of dimensions $s \times s$) is appropriately chosen, then the resonant mode with odd symmetry in the horizontal direction and even symmetry in the vertical direction is excited by the input modal field. Excitation of this mode insures small power coupling to the vertical arms, which results in low crosstalk T_2 and T_4 [62, 63]. If the air gap is appropriately chosen, the modal reflectivity R_1 can be made small and the modal transmissivity T_3 is maximized.
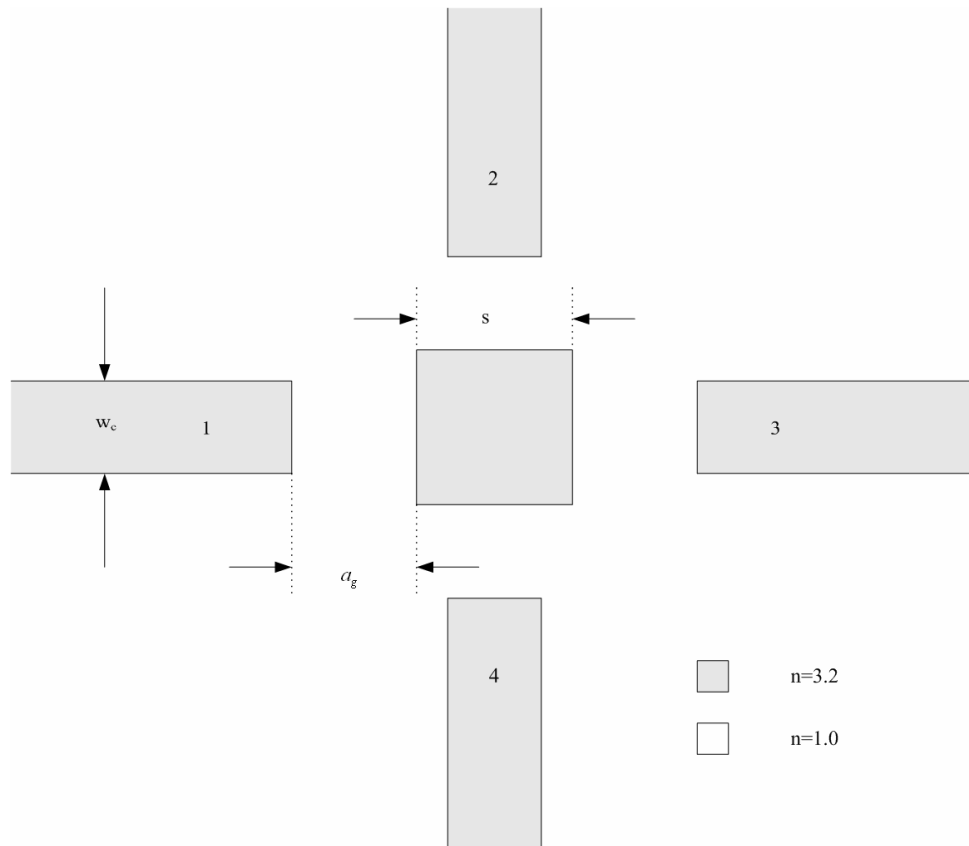
Figure 5-7 Waveguide crossing with a square resonant cavity at the center

When the side of the square cavity $s = 0.36$ µm and the air gap separating the cavity from the four arms is taken as $a_g = 0.04$ µm, the WC is optimized (i.e. small R_1, T_2, T_4 and large T_3) around the wavelength $\lambda = 1.55$ µm. Figure 5-8 shows an image of the field intensity around the WC. The origin is located at the geometrical center of the cavity. The fundamental mode of arm 1 is assumed to be incident on the WC and is not shown in the image in order to enhance the visibility of the reflected field.
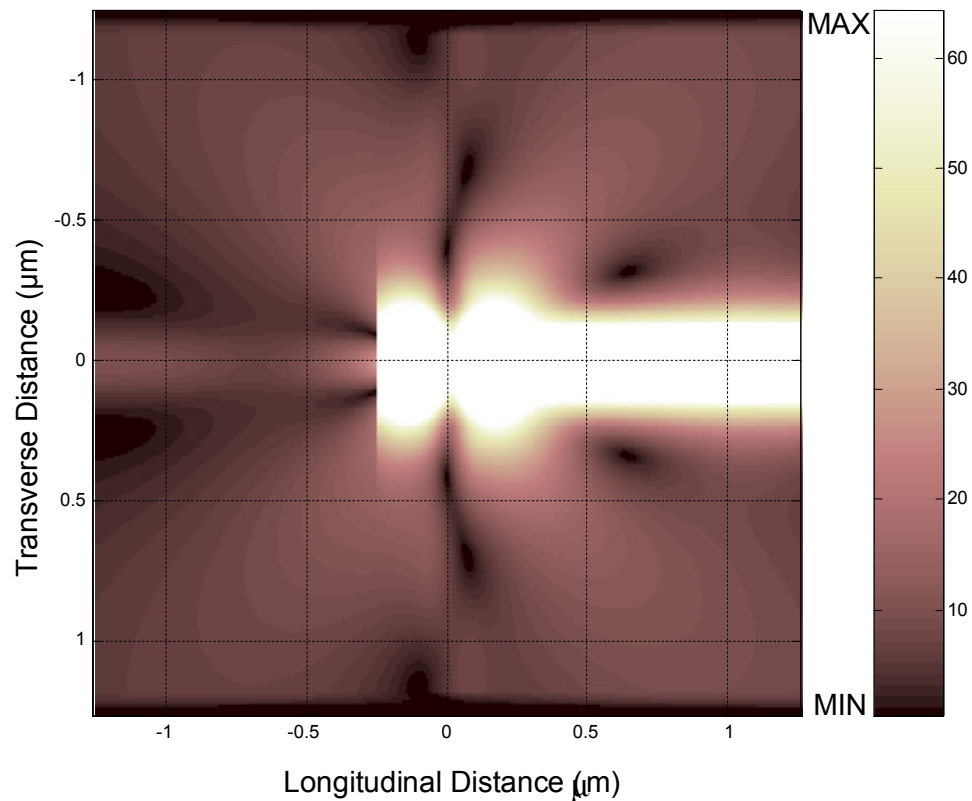
Figure 5-8 Field intensity image inside the WC with square resonant cavity

Figure 5-8 clearly shows odd mode excitation (in the horizontal direction) inside the square resonant cavity, thus causing a small amount of power to be coupled to the upper and the lower arms of the WC. Figure 5-9, 5-10, 5-11 and 5-12 respectively show a comparison between the modal reflectivity, crosstalk, the modal transmissivity and the fraction of power radiated for the simple WC and WC with the square resonant cavity. As seen in Figure 5-9, the modal reflectivity of the modified WC (having a square cavity) is generally much smaller than that corresponding to the simple WC. The minimum reflectivity of the modified WC is about 1.5×10^{-4} which occurs around $\lambda = 1.57$ μm. The modal reflectivity generally remains low $\left(< 10^{-2} \right)$ for λ ranging between 1.54-1.60 μm.
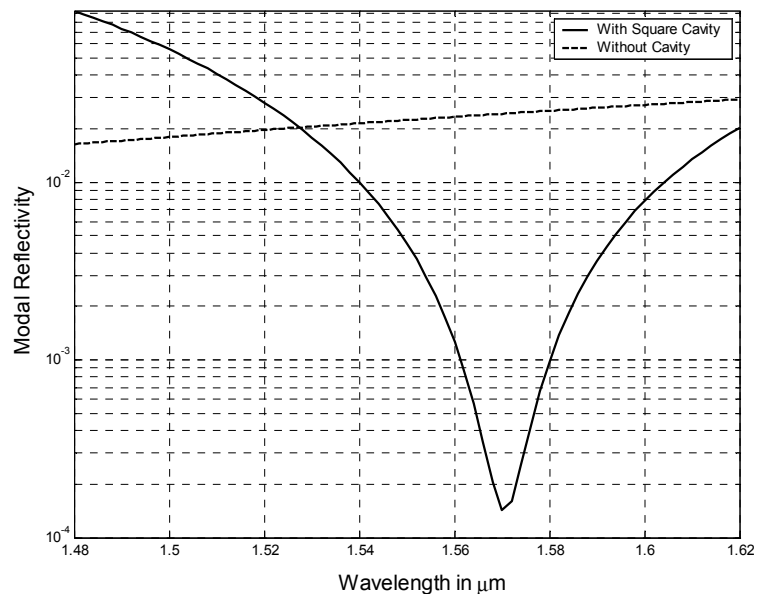
Figure 5-9 Comparison of the modal reflectivity of the simple WC and the WC with square cavity
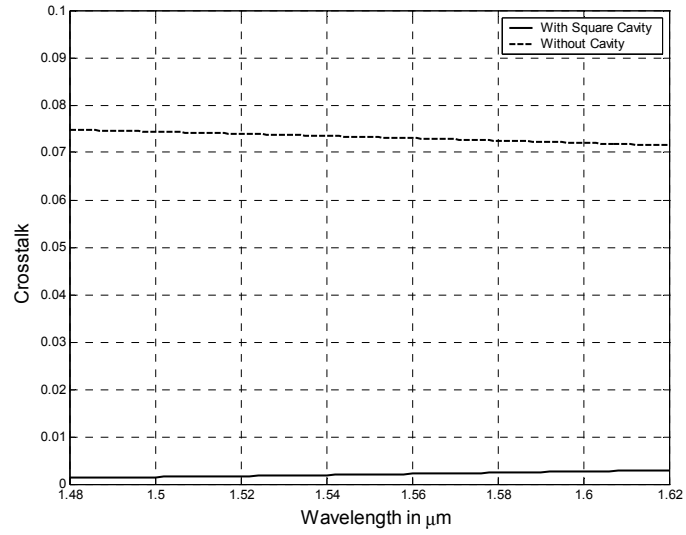
Figure 5-10 Comparison of crosstalk of the simple WC and the WC with square cavity
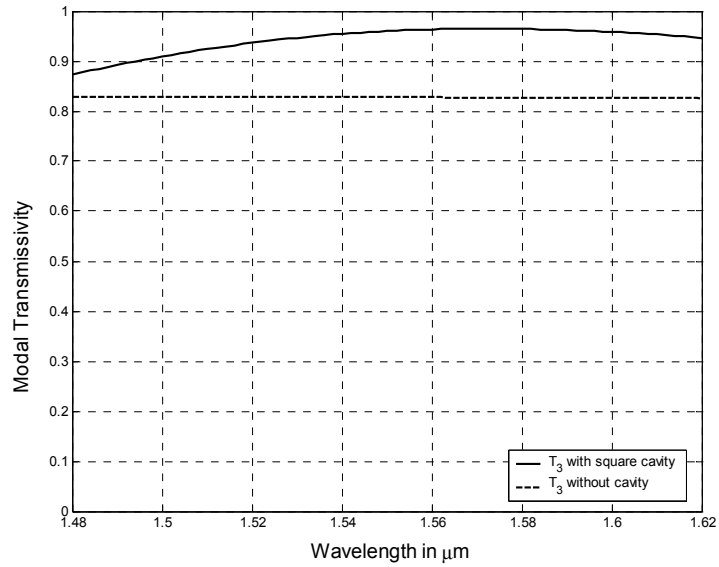
Figure 5-11 Comparison of modal transmissivity of the simple WC and the WC with square cavity
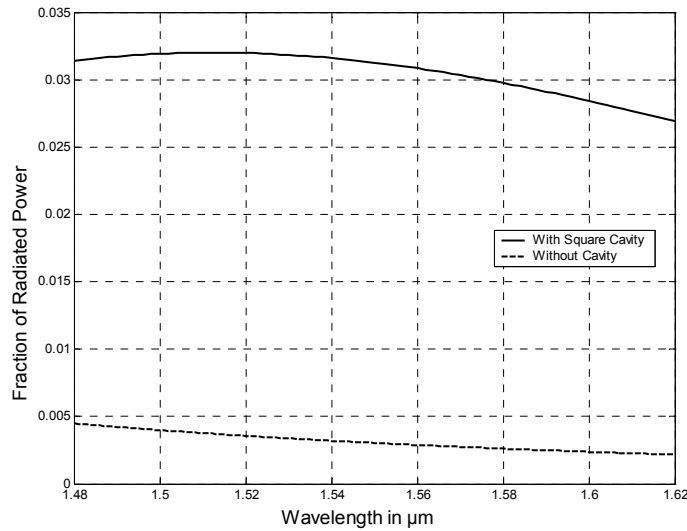
Figure 5-12 Comparison of fraction of radiated power of the simple WC and the WC with square cavity

As seen in Figure 5-10, the crosstalk has decreased from about 0.07 for the simple *WC* to about 0.001 for the *WC* with the square cavity. This reduction in the crosstalk is important, because crosstalk is undesirable. The modal transmissivity, as shown in Figure 5-11, has increased from approximately 0.83 for the simple *WC* to about 0.965 for the *WC* with square cavity. The modal transmissivity in this case remains higher than the modal reflectivity of the simple *WC* for a wide range of wavelengths. However, there is an increase in the fraction of radiated power for the *WC* with square cavity as can be seen in Figure 5-12. This can be ascribed to the presence of the air gaps between the arms and the resonant cavity.

5.4.   WAVEGUIDE CROSSING WITH OCTAGONAL CAVITY

In this section, we replace the square resonant cavity with a resonant cavity having the shape of an octagonal. We have two major aims in the selection of the octagonal cavity. First, we are interested in examining the suitability of the general $PBPM$ for this type of structure, since it contains longitudinally tapered portions and at the same time, this structure gives rise to a guided optical field in the vertical direction. Thus, this should be a unique structure for testing the applicability of the $PBPM$.

The second aim is to analyze the spectral response of the WC with octagonal and square cavities and compare the results in order to make a decision on which cavity shape provides a better spectral response.

The octagonal cavity can be thought of as a square with the corners chopped off. The structure consists of eight sides with four sides parallel to the four waveguide arms with equal width (w_c) as that of the waveguide cores, and the other four sides are inclined as shown in Figure 5-13 each having a width of w. The inclined walls of the octagonal cavity are approximated using the staircase approximation as done in chapter 4 when considering the beam expander. The number of steps used for the stair case approximation to the inclined walls were fixed at 10 which gives convergent results using the general $PBPM$. With 10 steps for the stair case approximation, the total number of longitudinal

discontinuities are 24, which makes the analysis of this type of problems computationally demanding using the MOL. The number of transverse mesh points per micron were fixed at 40 points.

An extensive number of simulations were done in order to find optimized parameter values of a_g and w. The air gap width $a_g = 0.06$ μm and the inclined width $w = 0.13$ μm gave optimized results. Figure 5-14 shows comparison of the modal reflectivities for the WC with the octagonal and the square resonant cavities. The octagonal cavity results in a smaller reflectivity minimum (2×10^{-5} at λ=1.564 μm) than the square cavity (1.5×10^{-4} at λ=1.57 μm). The octagonal cavity also gives rise to a wider reflectivity bandwidth. However, there is an increase in the crosstalk for the WC with octagonal cavity, as seen in Figure 5-15. However, for a wide wavelength range, the crosstalk remains below 0.01.

Figure 5-16 shows a comparison of the modal transmissivities for the WC with octagonal and square resonant cavities. The value of T_3 for the WC with the octagonal cavity is slightly higher than that of the WC with the square cavity. The fraction of radiated power is approximately 0.015 for the WC with the octagonal cavity when compared to about 0.032 for the WC with the square cavity as shown in Figure 5-17.
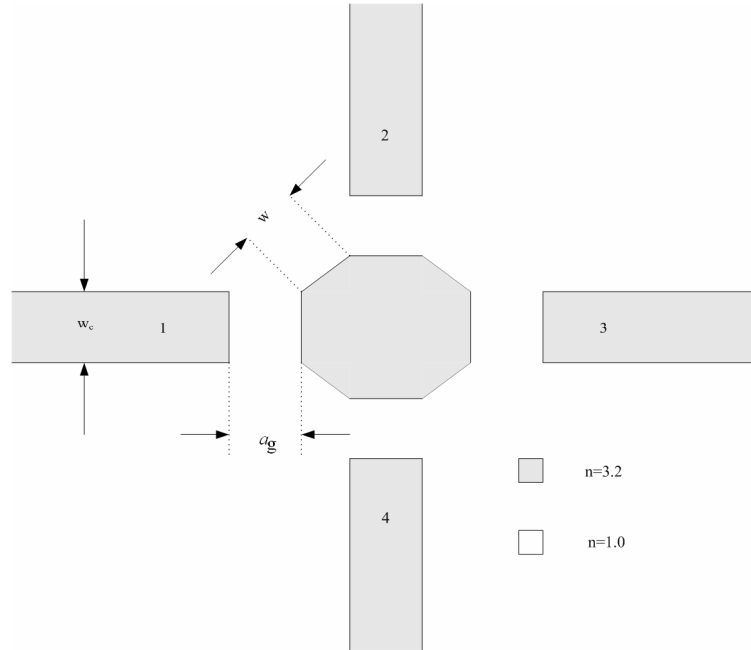
Figure 5-13 Waveguide crossing with an octagonal resonant cavity
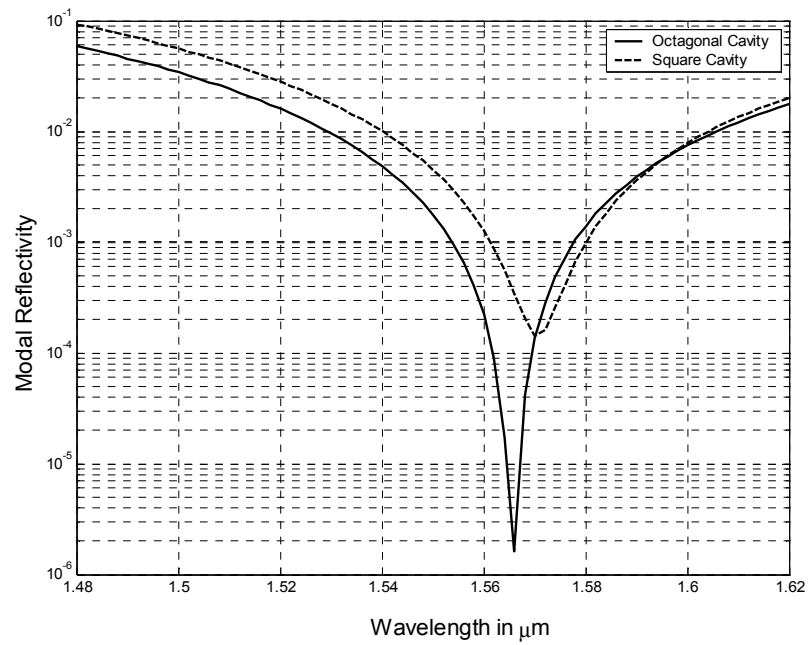
Figure 5-14 Comparison of the modal reflectivity of the WC with octagonal and square cavities
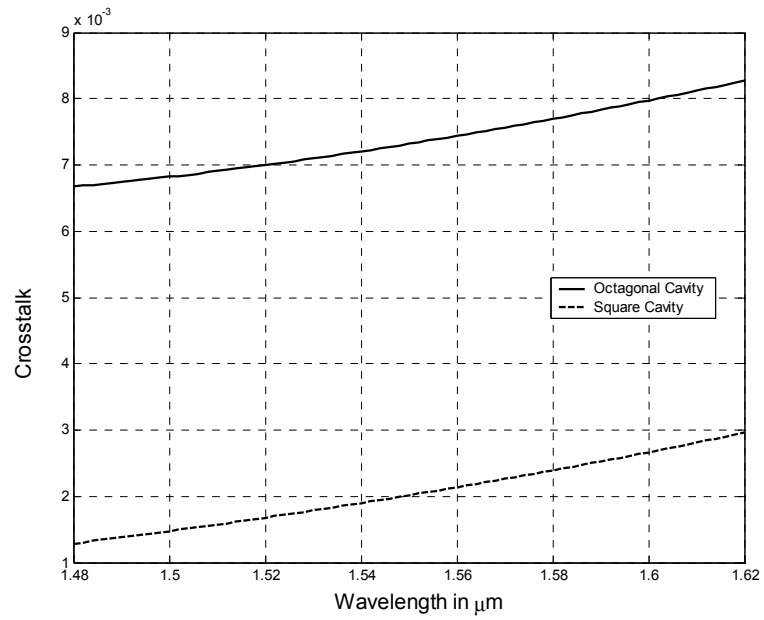
Figure 5-15 Comparison of crosstalk of the WC with octagonal and square cavities
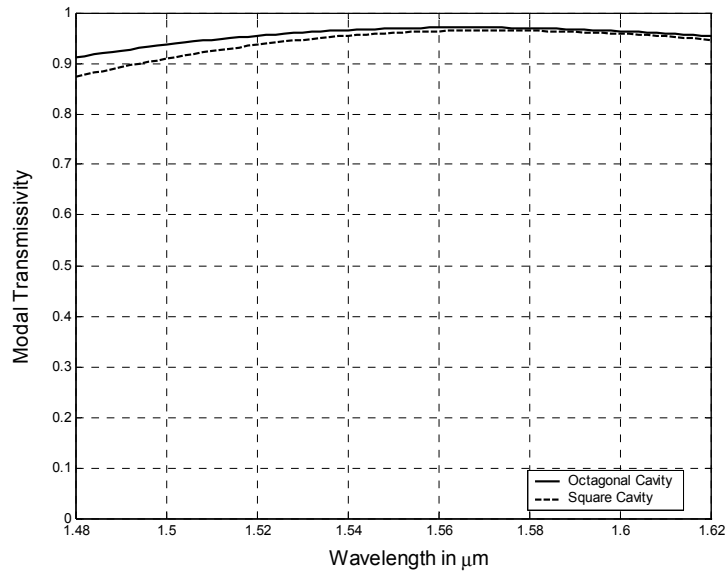
Figure 5-16 Comparison of the modal transmissivity of the WC with octagonal and square cavities
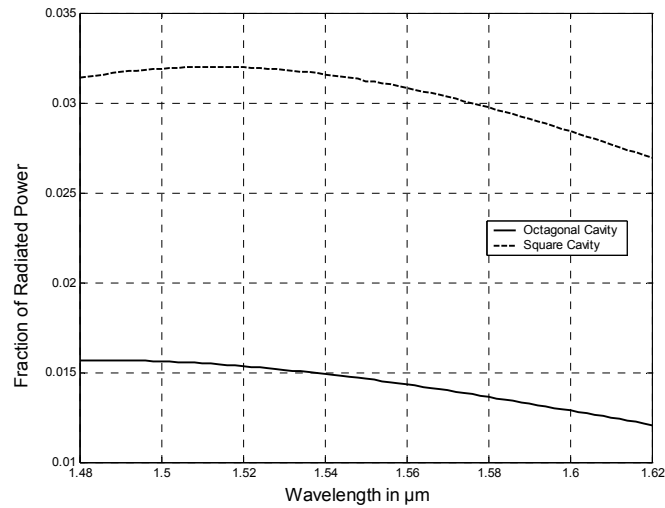
Figure 5-17 Comparison of the fraction of radiated power of the WC with octagonal and square cavities

The air gap a_g and the width w of the WC are crucial in deciding the values of R_1, T_2, T_3 and T_4. The effect of which are analyzed and shown in Figure 5-18 and 5-19. Figure 5-18 shows the behavior of the structure with different values of w while fixing a_g at 0.06 µm. As can be seen in the figure, that as w increases, the resonance wavelength of the WC shifts towards higher wavelengths. In each case considered, the minimum reflectivity is very small.

When the air gap changes while fixing w to 0.13 µm there is also a shift in the resonance wavelength, as seen in Figure 5-19. The resonance wavelength also increases with the air gap width. From Figure 5-18 and 5-19 it can be observed that the air gap and

the width are inter-related with each other. For a particular value of a_g there is a certain value of w which gives the least modal reflectivity. For some combinations of these two parameters, the minimum modal reflectivity can reach as low as 10^{-6}.
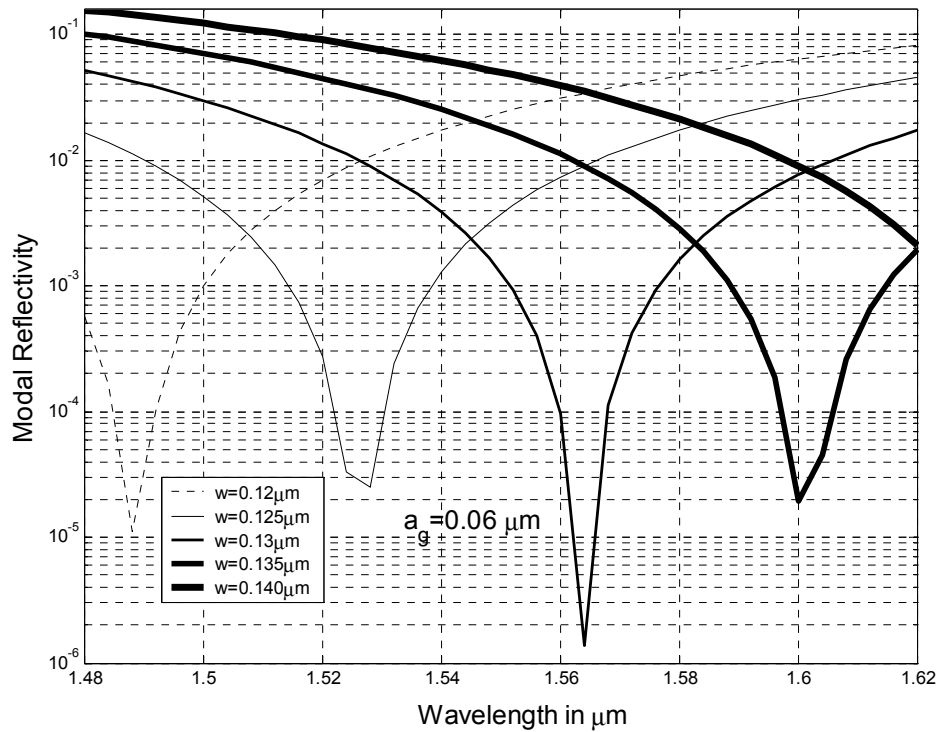
Figure 5-18 Comparison of modal reflectivities for the WC with the octagonal cavity for different widths w, and fixed air gap a_g=0.06 µm
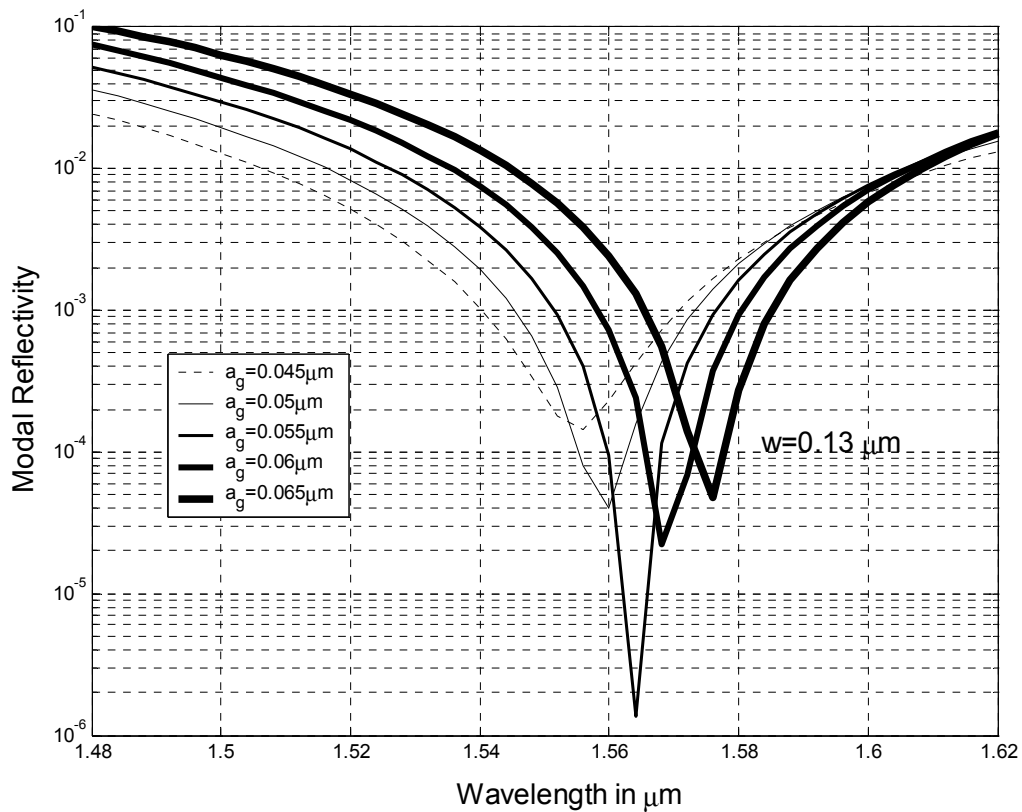
Figure 5-19 Comparison of modal reflectivity for the WC with the octagonal cavity for different air gaps a_g and fixed width w =0.13 μm

5.5.   CONCLUSION

Three different types of waveguide crossings were studied in this chapter. The simple *WC* has a comparatively high modal reflectivity and high crosstalk, with relatively low transmissivity. However, the radiation loss is small. The performance of this *WC* can be improved by coupling to a resonant cavity. The square resonant cavity offers higher

transmissivity, lower reflectivity and lower crosstalk but with higher radiation losses when compared to the simple WC. The proposed octagonal structure surpasses performance of the simple WC and the WC with square cavity in all aspects with the exception of some increase in the crosstalk.

As discussed at the outset of this chapter, the primary design criterion of waveguide crossing is to minimize crosstalk. However, the cavity in the waveguide crossing may be modified in order to result in relatively high coupling to the vertical arms, leading to a three way beam splitter. As will be shown in the next chapter, a rectangular cavity of suitable dimension may be used for this purpose.

CHAPTER 6

ANALYSIS OF THREE WAY BEAM SPLITTER

6.1.   INTRODUCTION

We have seen in the previous chapter that when a resonance cavity is imbedded at the center of the WC, it is possible to minimize the modal reflectivity and the crosstalk, while maximizing the modal transmissivity. The device operation relies on the excitation of a cavity mode which has odd symmetry in the horizontal direction and even symmetry in the vertical direction. In this chapter, we introduce a novel three way beam splitter that relies on a similar principle to the above mentioned WC. Here we are interested in causing optical power to be coupled to the vertical arms, rather than to inhibit the coupling, as has been done in the WC. If the square cavity of the WC considered in the previous chapter is replaced by a rectangular cavity by reducing its horizontal dimension, the odd mode in the horizontal direction is suppressed and the mode with even symmetry in the horizontal direction is excited instead. Thus, the field in the horizontal center of the rectangular cavity is maximized in this case, which may result in substantial power coupling to the vertical arms. This principle will be demonstrated in the present chapter, which leads to a 90-degree three way beam splitter. All the calculational results were obtained using the general $PBPM$ approach and the field intensity images that will be presented correspond to an operating wavelength of $\lambda = 1.55$ μm.

6.2.   THREE WAY BEAM SPLITTER

Consider the structure shown in Figure 6-1. This structure is similar to the structure discussed in the previous chapter. It differs only in the resonant cavity which is here rectangular in shape. The width w of the cavity is taken to be less than the waveguide core width of the arms. This is done in order to insure excitation of the cavity mode which has symmetry in the horizontal and vertical directions. The height h of the structure is assumed to be larger than the core width in order to improve power coupling in the upper and the lower waveguide arms. The waveguide core width is fixed to $w_c = 0.2$ μm. The parameters a_1, a_2, a_3 and a_4 are associated with the four air gap widths as shown in Figure 6-1. the parameters a_2 and a_4 represent the upper and lower air gap width, respectively. However, a_1 and a_4 represent only a portion of the air gap width in the horizontal direction. The complete air gap in the horizontal direction can easily be calculated from the figure, if necessary.

The primary design criterion for the structure is to have minimum modal reflectivity. For all the cases considered in this chapter, the modal reflectivity is kept below about 10^{-3}.
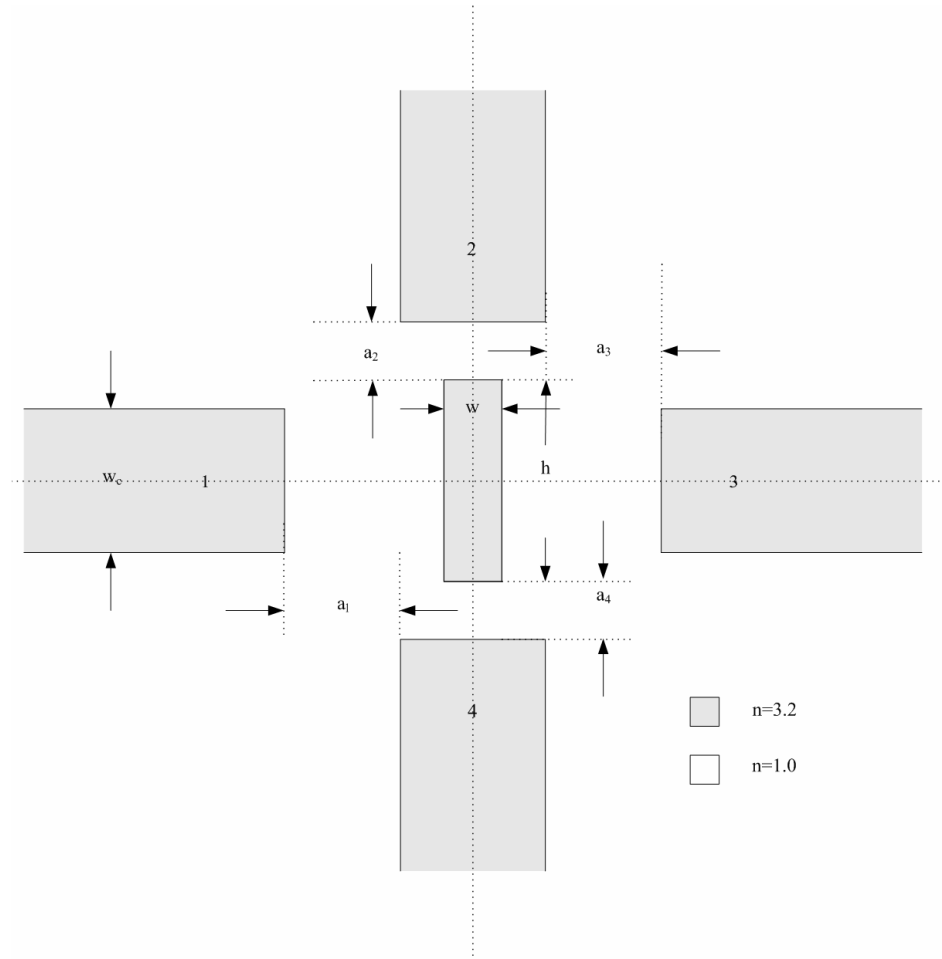
Figure 6-1 Three way beam splitter

The values of the various parameters of the three way beam splitter (i.e. a_1, a_2, a_3, a_4, w and h) will be varied in order to control the splitting ratio in the different arms of the beam splitter, while maintaining low modal reflectivities. Only key cases will be presented in the sections to follow. We begin by considering the case in which most of the power transmitted in the forward direction to the right arm of the beam splitter.

6.2.1. <u>Case I Maximum Forward Transmission</u>

The first case to be studied is when maximum power transmission occurs in the forward direction with minimum power being coupled to the vertical arms and minimum reflectivity. The structure is kept symmetric with respect to the horizontal and the vertical axes, i.e. $a_1 = a_3$ and $a_2 = a_4$. The air gaps and the width and the height of the rectangular cavity are tuned in order to obtain the desired effect. The tuned parameter values in this case are $a_1 = a_3 = 0.00 \ \mu m$, $a_2 = a_4 = 0.50 \ \mu m$, $w = 0.09 \ \mu m$ and $h = 0.53 \ \mu m$. The parameters a_1 and a_3 being zero as mentioned earlier does not actually mean that there is no air gap separating the (left and right) arms from the rectangular cavity. The air gaps separating the horizontal arms from the cavity are both equal to 0.055 μm in this case.

Figure 6-2 shows the resulting modal reflectivity spectrum of the beam splitter. As can be seen in the figure, the modal reflectivity is extremely low $\left(< 2 \times 10^{-3} \right)$ over a wide range of wavelength. Minimum reflectivity of $\left(6 \times 10^{-5} \right)$ occurs at a wavelength of 1.56 μm. Figure 6-3 shows the modal transmissivity coupled in the vertical arm. Note that since $T_2 = T_4$ in this case, only one curve is shown in the figure. The value of $T_2 = T_4$ is approximately 0.006 and it decreases with wavelength.
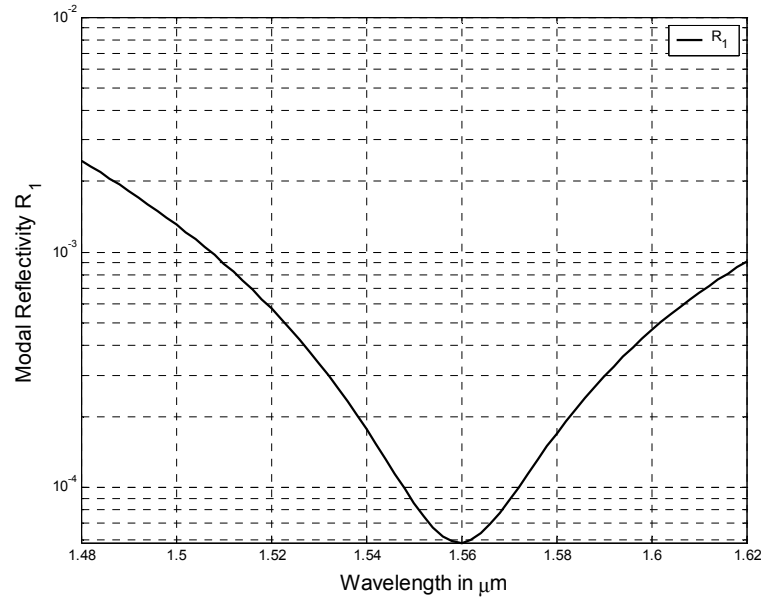
Figure 6-2 Modal reflectivity spectrum of the beam splitter
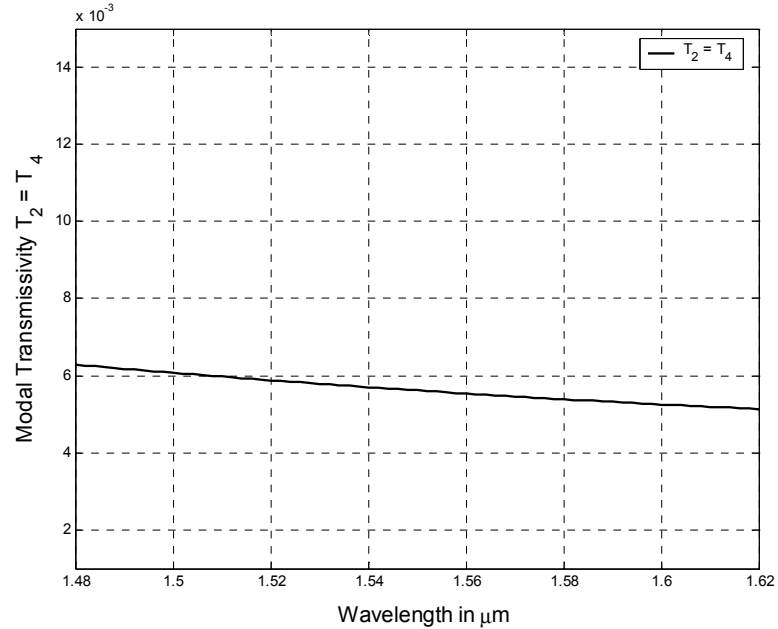
Figure 6-3 Modal transmissivity T_2 coupled in the upper (or lower) vertical arm

Figure 6-4 shows the modal transmissivity T_3 of the beam splitter. As can be seen from the figure, T_3 remains fairly high and is fairly constant over the entire wavelength range. It is approximately 0.985. The fraction of the radiated power is shown in Figure 6-5. It remains relatively low, within the approximate range 0.003-0.007.

Figure 6-6 shows an image of the field intensity around the splitter. As mentioned earlier, all the field intensity images correspond to an operating wavelength $\lambda = 1.55$ μm. The origin of the images is always centered at the geometric center of the structure. The TE_0 modal field is assumed to be incident from the left. As can be seen in the figure, the power coupled into the upper and the lower arms of the splitter is very small. The absence of any visible standing wave pattern in the input arm indicates insignificant amount of power reflection.

The air gaps play an important role in coupling power to the respective arms. If the air gaps are not properly tuned, this would result in large radiation losses, large modal reflectivity, or lower modal transmissivities. Figure 6-7 shows the effect of varying a_3 (with all other parameters fixed to their previous values) on R_1, $T_2 = T_4$, T_3 and the fraction of radiated power.
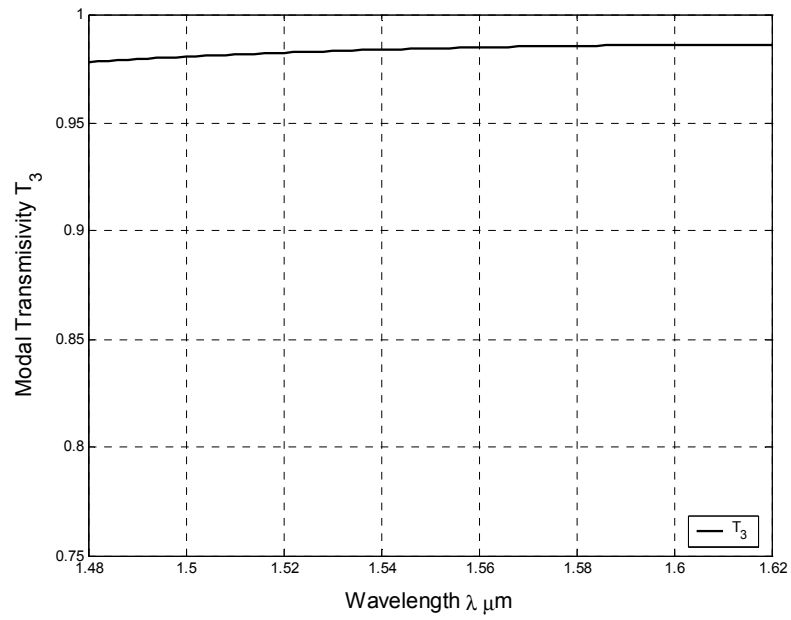
Figure 6-4 Modal transmissivity T_3 of the beam splitter
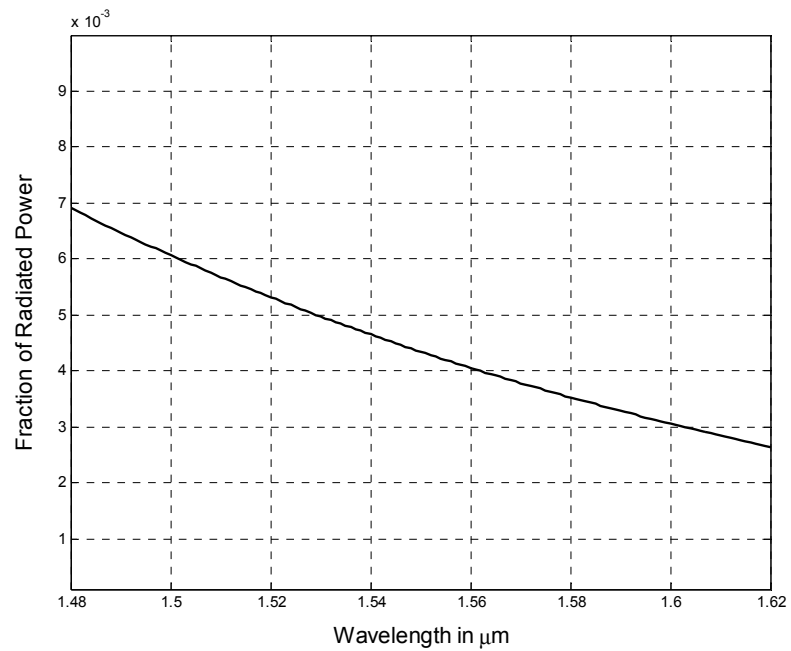
Figure 6-5 Fraction of radiated power in the beam splitter
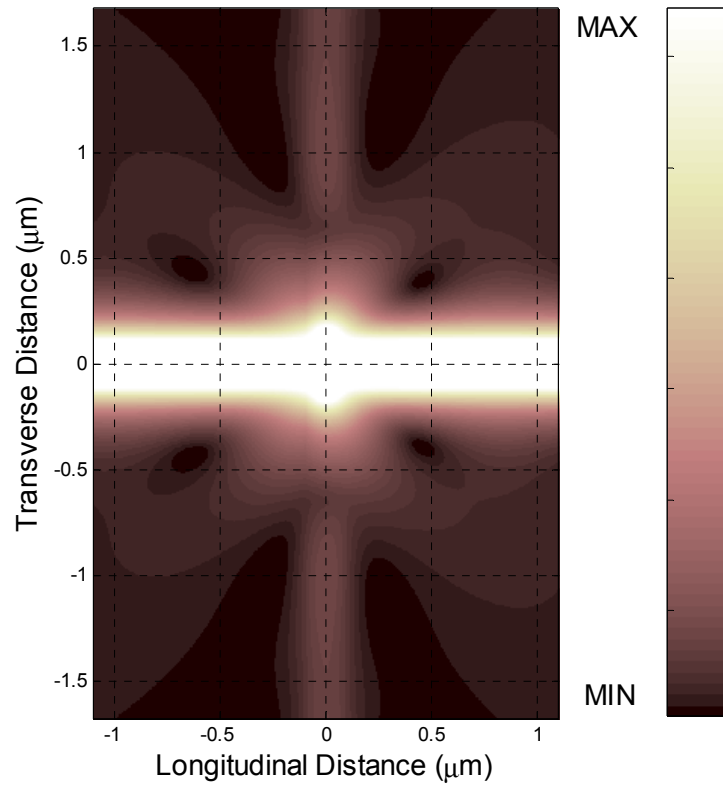
Figure 6-6 Field intensity image showing maximum power coupling into the forward arm

As a_3 increases, R_1 initially increases reaching a peak value at $a_3 = 0.3$ μm (see Figure 6-7 a) and starts to decrease as a_3 increases further. However, R_1 again starts to increase for $a_3 > 0.75$ μm. A similar behavior is observed for $T_2 (= T_4)$ as seen in Figure 6-7 b. As seen in Figure 6-7 c, there is a large decrease in T_3 as a_3 increases. This can be attributed to the increase in the fraction of radiated power as seen in Figure 6-7 d.
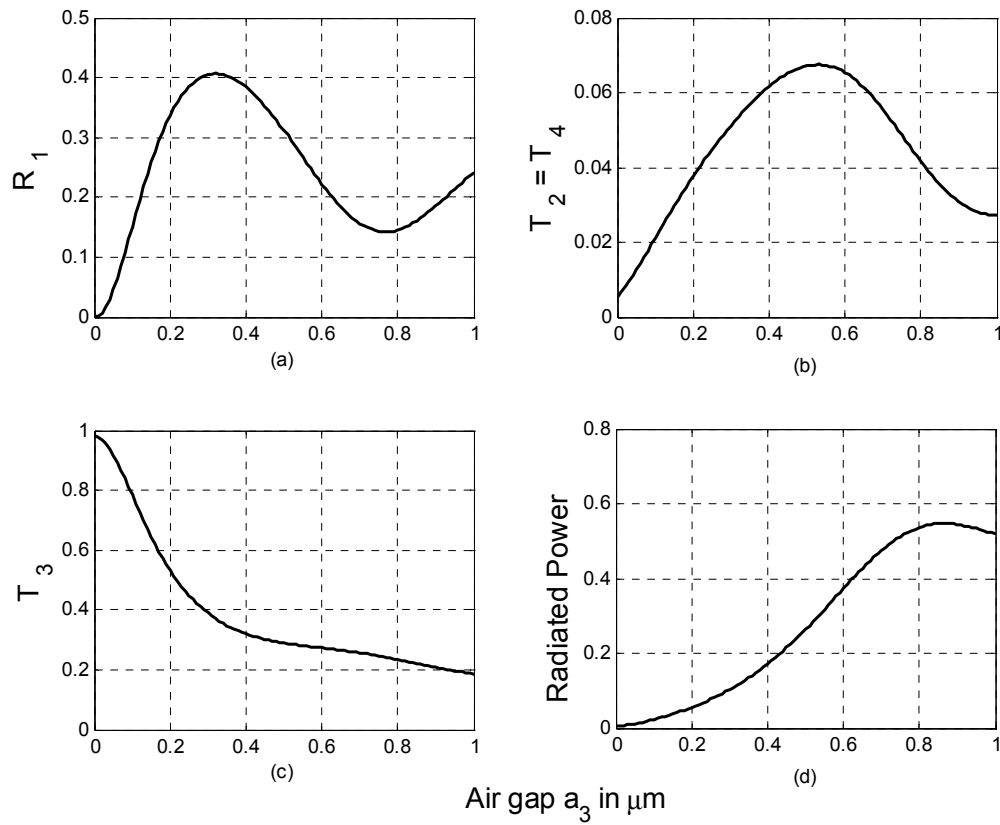
Figure 6-7 Variation of R_1, T_2, T_3 and the fraction of radiated power with a_3

6.2.2. Case II Controlled Power in the Upper and the Lower Arms

The previous case studied was of low coupling of power in the vertical arms. However, this structure can be easily tuned for coupling more power in the vertical arms. This can be achieved by increasing the parameter a_3 and effectively reducing the air gaps

$\left(\text{by reducing } a_2 \text{ and } a_4\right)$ between the cavity and the vertical arms thus forcing the cavity

to couple more power into the vertical arms. The parameter values $a_1 = 0.04$ μm,

$a_3 = 0.07$ μm, $a_2 = a_4 = 0.12$ μm, $w = 0.06$ μm and $h = 0.62$ μm cause an increase in

the power coupled to the vertical arms from almost negligible values, as in case I, to

around 0.11 in both arms. In order to maintain equal power coupling in the vertical arms,

the two air gaps a_2 and a_4 were kept equal so that we always have $T_2 = T_4$. The air gaps

a_2 and a_4 have been reduced from 0.5 μm in the previous case to 0.12 μm which helps in

coupling more power in the vertical arms, while the air gap a_3 has been increased in order

to cause less coupled power in arm 3.

Figure 6-8 shows the resulting modal reflectivity R_1 of the beam splitter. As can be

seen, using the last set of parameters, the modal reflectivity is low over a wide range of

wavelength. The coupling in the vertical arms increases in this case as can be seen in

Figure 6-9. The modal transmissivity coupled is approximately 0.11. It is noteworthy that

T_2 remains almost unchanged over a wide range of bandwidth. The modal transmissivity

is reduced in this case as can be seen in Figure 6-10 and it is approximately 0.77 in value.

The fraction of the radiated power is shown in Figure 6-11. It remains relatively low,

within the approximate range 0.005-0.01. Figure 6-12 shows an image of the field

intensity around the splitter.
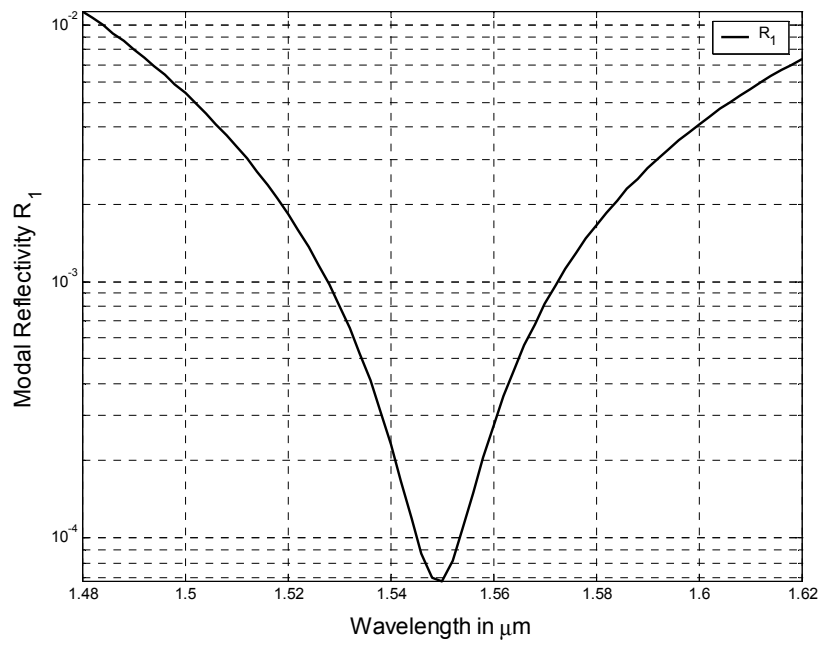
Figure 6-8 Modal reflectivity spectrum of the beam splitter
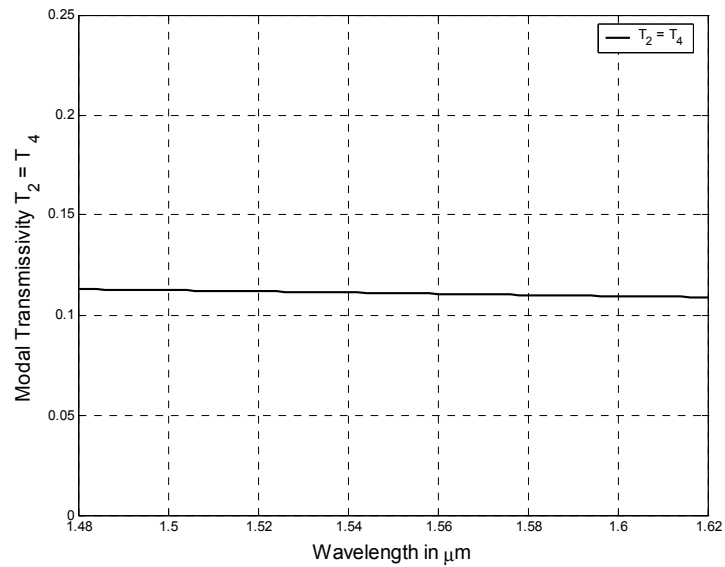
Figure 6-9 Variation of the modal transmissivity in the upper arm with wavelength
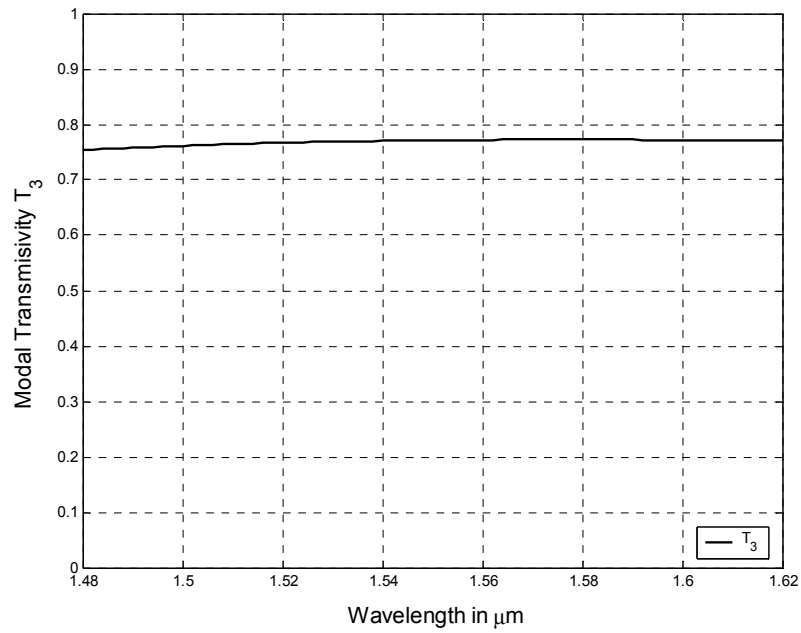
Figure 6-10 Variation of the modal transmissivity T_3 with wavelength
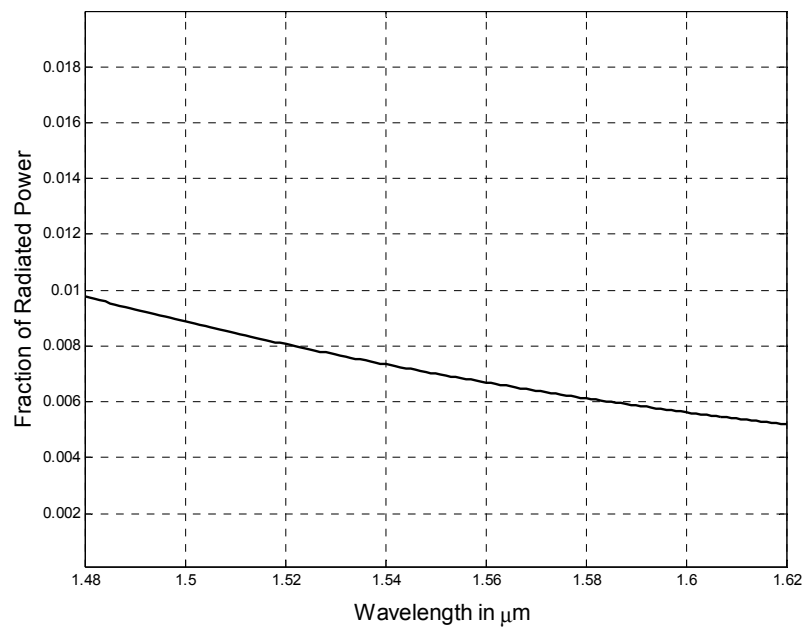
Figure 6-11 Variation of the fraction of radiated power with wavelength
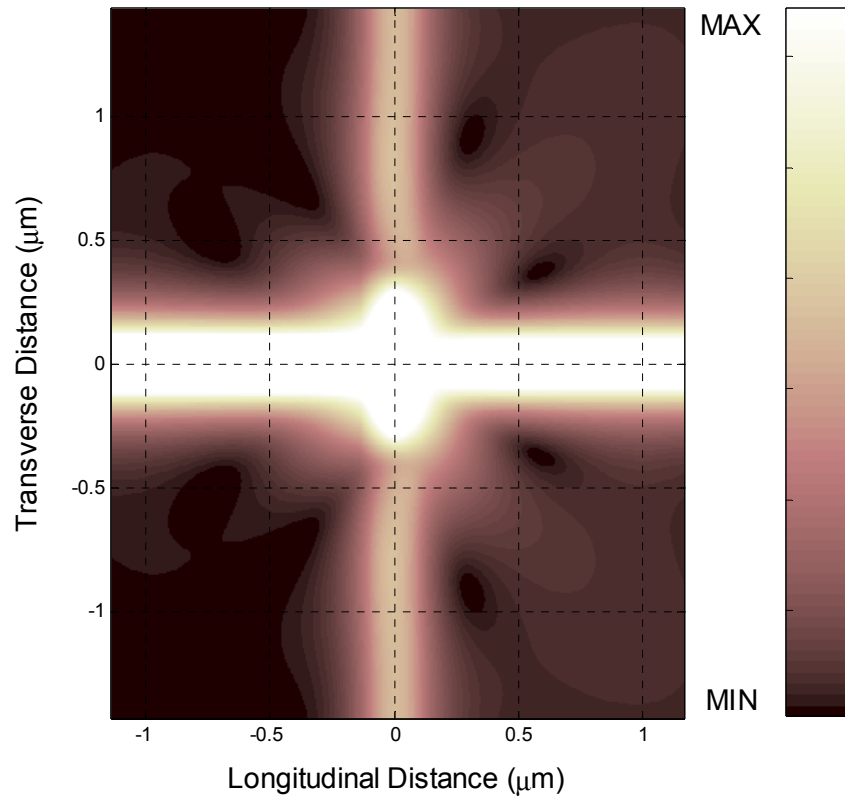
Figure 6-12 Field intensity image showing increased power coupling in the upper and lower arms

6.2.3. Case III Equal Power in all Arms

The third case considered is when nearly equal power is being coupled in the vertical and the forward arms. This can also be achieved in a similar manner as in case II by further increasing a_3. The set of parameters used in this case are $a_1 = 0.04$ μm, $a_3 = 0.19$ μm, $a_2 = a_4 = 0.3$ μm, $w = 0.06$ μm and $h = 0.53$ μm.

As can be seen in Figure 6-13, the modal reflectivity remains relatively low over the entire wavelength range considered. The modal transmissivities T_2 and T_3, are shown in Figure 6-14 and 6-15 respectively. It is clear from these two figures that $T_2 = T_4 \approx T_3$ over the entire range of wavelength. The fraction of radiated power has slightly increased when compared with the previous case to about 0.015-0.02 (see Figure 6-16).
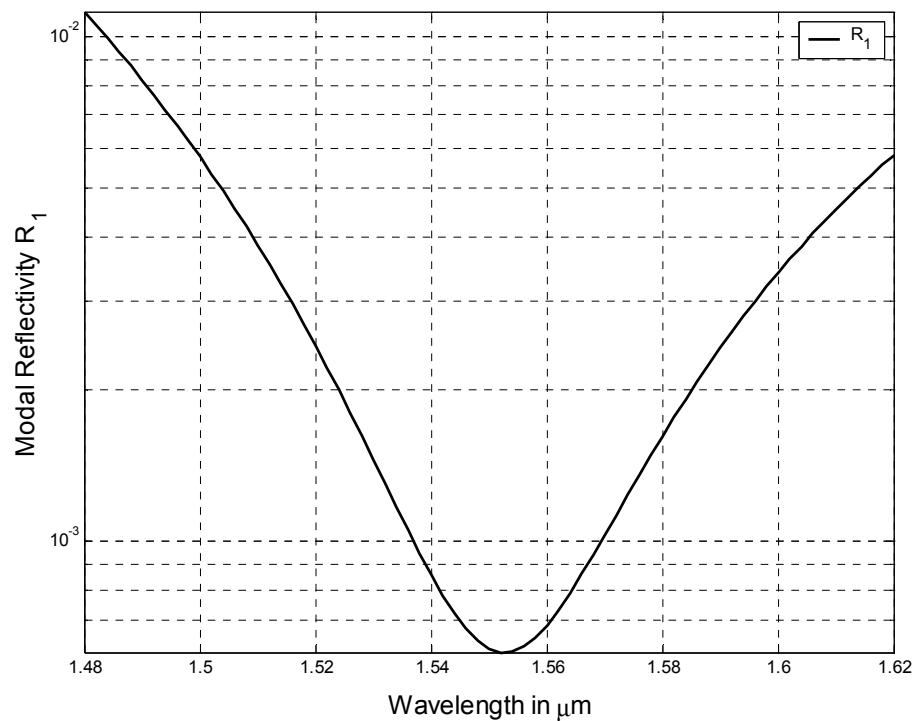
Figure 6-13 Modal reflectivity spectrum of the beam splitter
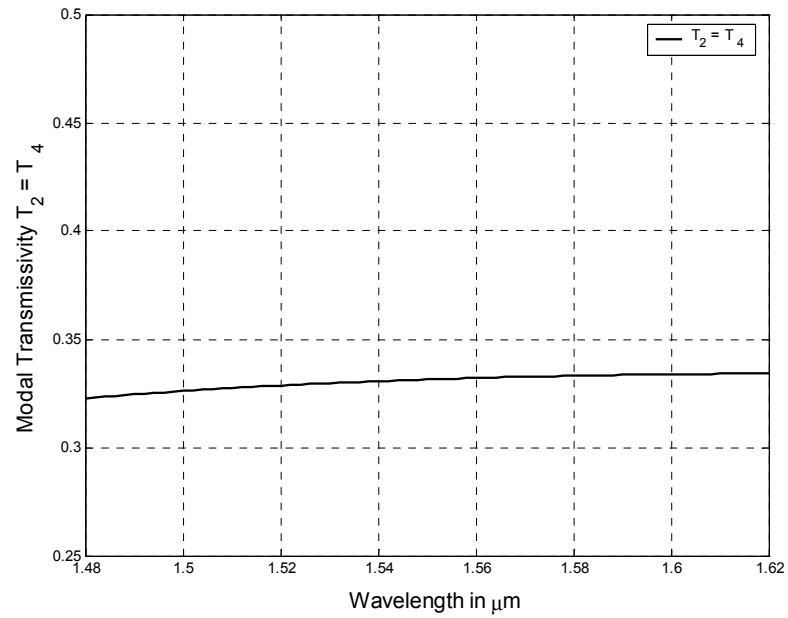
Figure 6-14 Variation of the modal transmissivity in the upper arm with wavelength
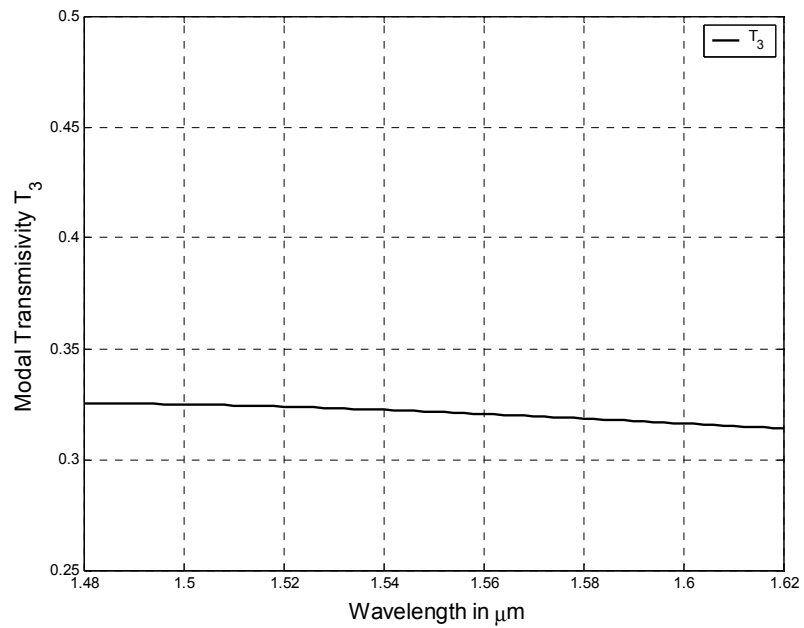
Figure 6-15 Variation of the modal transmissivity T_3 with wavelength
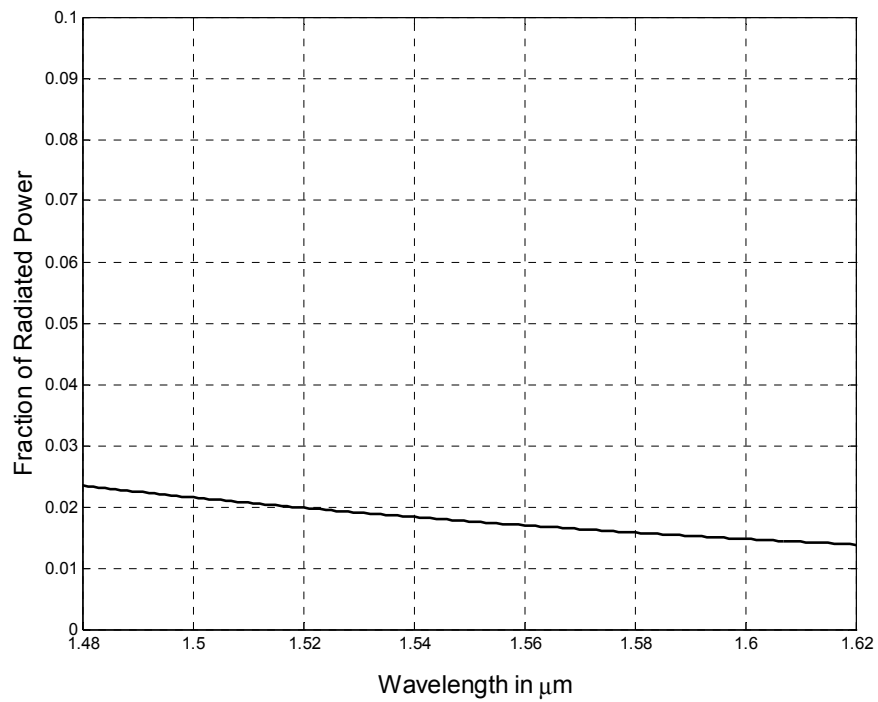
Figure 6-16 Variation of the fraction of radiated power with wavelength

Figure 6-17 shows an image of the field intensity around the beam splitter. The intensity in the three output arms, as suggested by the image, are nearly equal in this case.
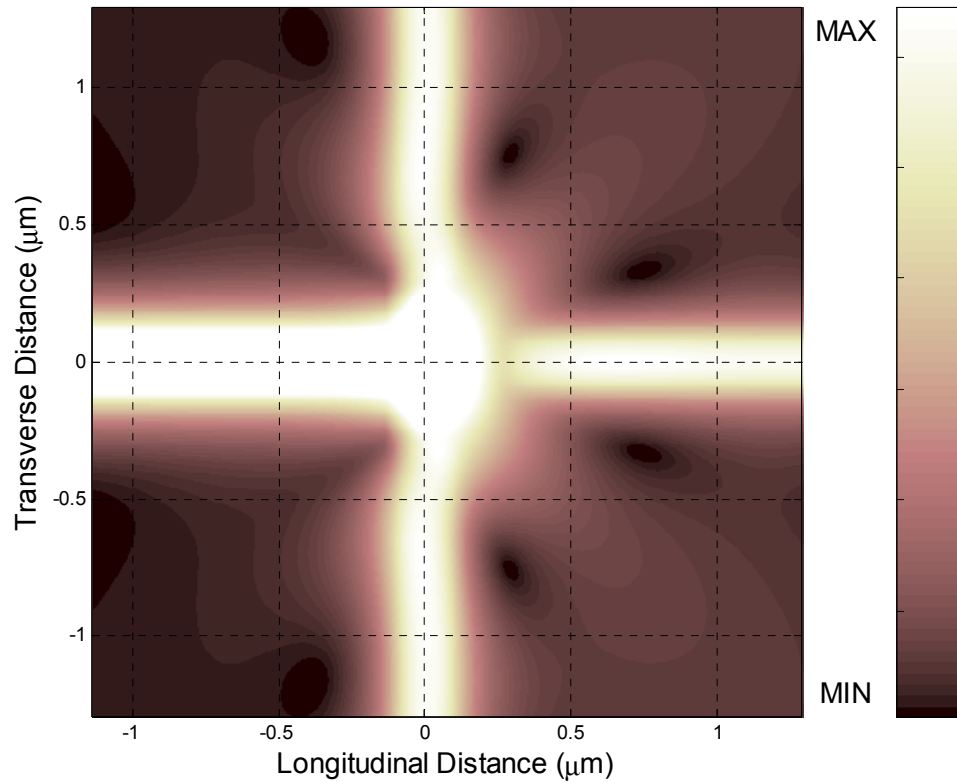
Figure 6-17 Field intensity image showing equal power coupling

6.2.4. <u>Case IV Higher Power in the Vertical Arms</u>

The fourth case we have considered is when the guided power coupled into the vertical arms (arms 2 and 4) is higher than the power in arm 3. In order to achieve this effect, the parameter a_3 is further increased and the vertical air gaps a_2 and a_4 are further reduced in value. The parameters are $a_1 = 0.00$ μm, $a_3 = 0.31$ μm, $a_2 = a_4 = 0.08$ μm, $w = 0.08$ μm and $h = 0.23$ μm.

Figure 6-18 shows the modal reflectivity spectrum corresponding to this case. The reflectivity remains to be extremely low over a wide range of wavelengths. The modal transmissivity in each vertical arm is in this case around 0.42 as shown in Figure 6-19 which is greater than the power being coupled to arm 3. The modal transmissivity T_3 is around 0.14 as seen in Figure 6-20. Figure 6-21 shows the fraction of radiated power which is generally less than 0.05 and decreases with wavelength.
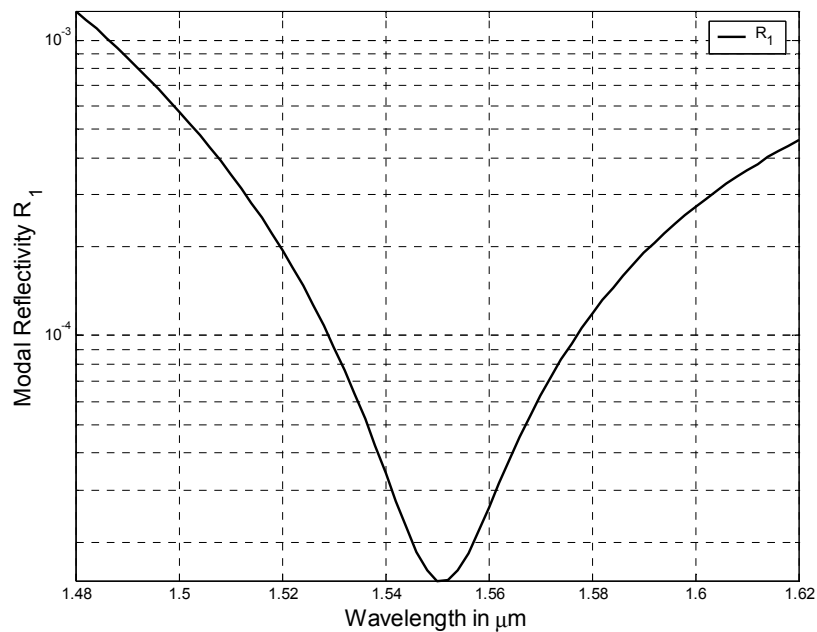
Figure 6-18 Modal reflectivity spectrum of the beam splitter
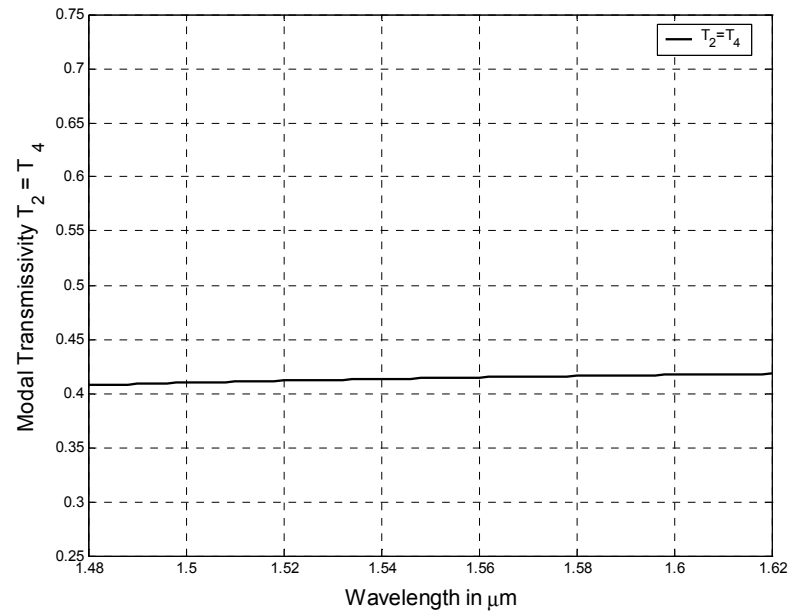
Figure 6-19 Modal transmissivity spectrum in the vertical arms
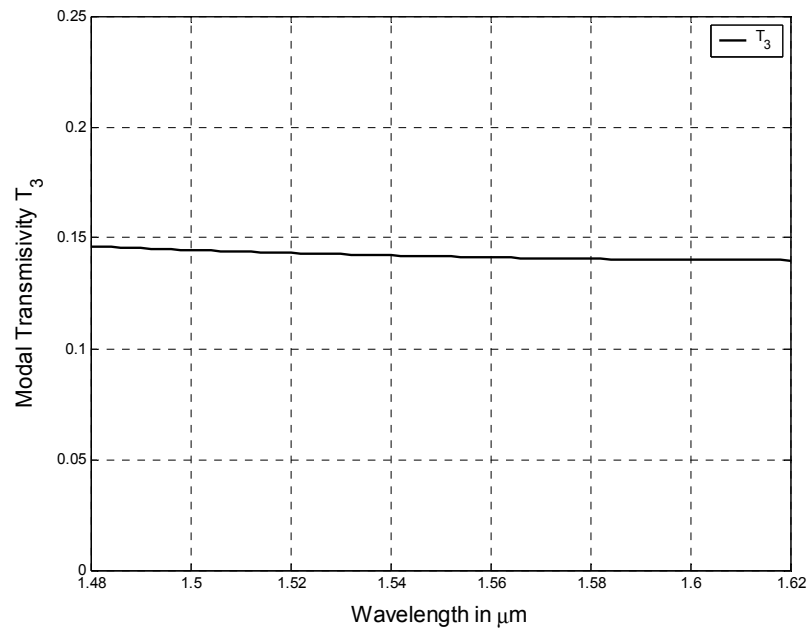
Figure 6-20 Modal Transmissivity spectrum in the output horizontal arm (T_3)
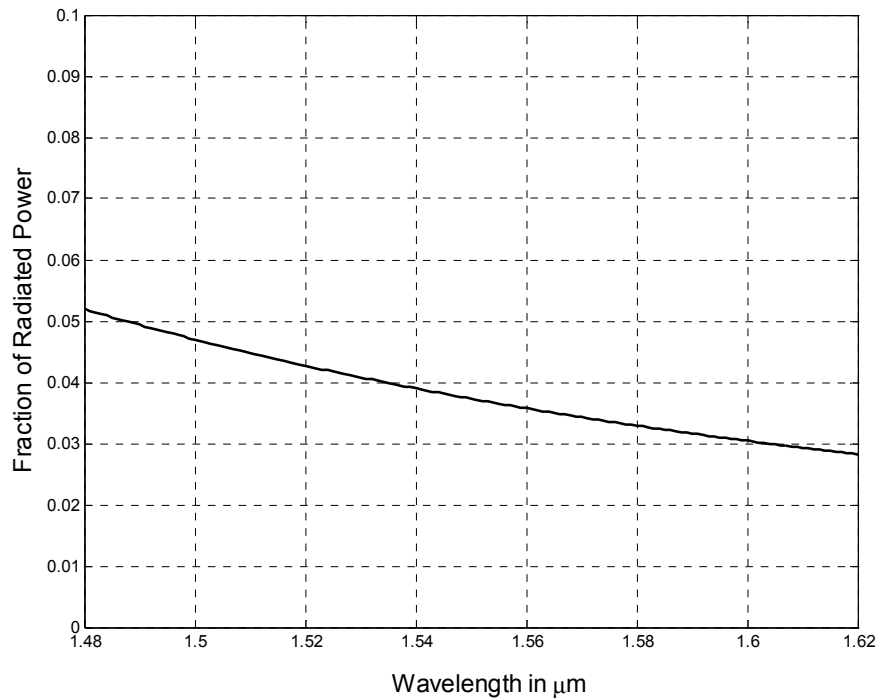
Figure 6-21 Fraction of radiated power associated with the beam splitter

As can be clearly seen from the field intensity image shown in Figure 6-22, higher field power is coupled to the vertical arms than to arm 3. This is the maximum power that we could achieve for symmetric power coupling in arms 2 and 4. It is also possible, by selecting a different set of parameters, to cause asymmetric power coupling between arms 2 and 4, making the power, for instance, higher in arm 2 with respect to arm 4. This case is presented in the next section.
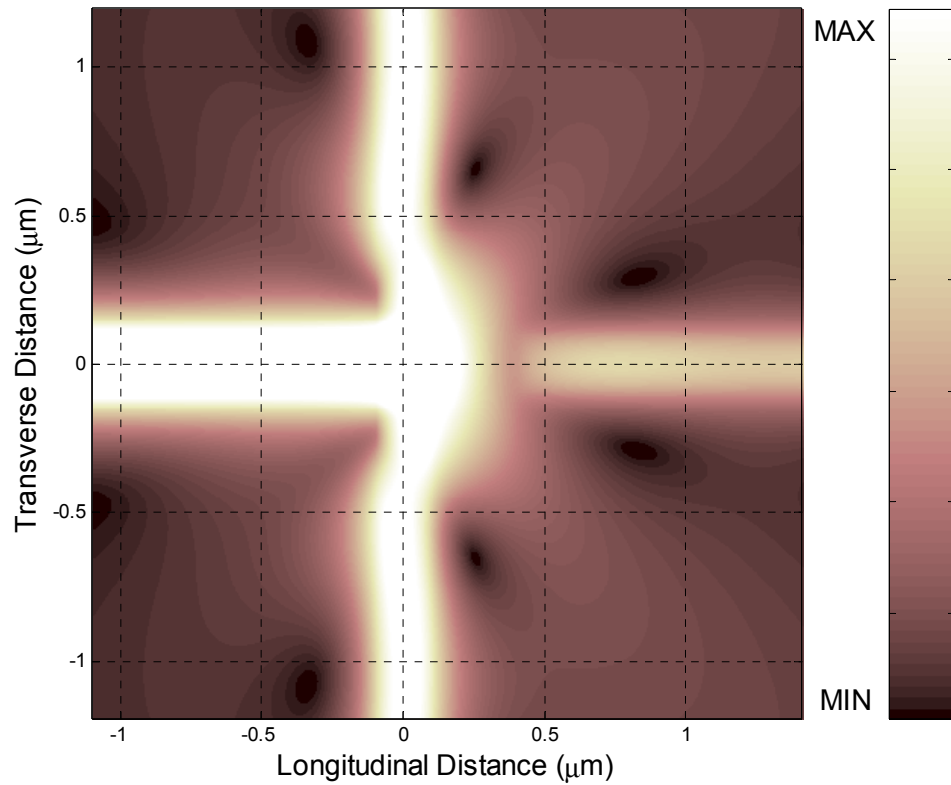
Figure 6-22 Field intensity image showing higher power being coupled to the vertical arms

6.2.5. Case V Maximum Power in the Upper Vertical Arm

The fifth and the final case to be considered is when maximum power is coupled to the upper vertical arm and comparatively less power being coupled to the lower vertical and the forward arms. The tuned parameters that give rise to this case are $a_1 = 0.00$ µm,

$a_3 = 0.25$ μm, $a_2 = 0.02$ μm, $a_4 = 0.23$ μm,, $w = 0.08$ μm and $h = 0.22$ μm. Note that

a_2 was reduced with respect to a_4 in order to achieve this effect.

As seen in Figure 6-23, the modal reflectivity is very low reaching a minimum of about 3×10^{-6} at λ=1.54 μm. The modal reflectivity remains below 10^{-3} for the entire wavelength range under consideration. Figure 6-24 shows the modal transmissivity T_2 and T_4 in the vertical arms. Since this is a vertically asymmetric case (since $a_2 \neq a_4$ and thus $T_2 \neq T_4$), both T_2 and T_4 are shown. T_2 is approximately 0.67, which is much higher than T_4 which is only 0.13 in this case. The modal transmissivity T_3 in the forward arm is around 0.17 as seen in Figure 6-25. As seen in Figure 6-26, the fraction of radiated power in this case ranges from $0.025 - 0.045$ which can be ascribed to the increase in the parameters a_3 and a_4. Figure 6-27 shows an image of the field intensity around the beam splitter corresponding to this case. It is clearly seen in the image that the power coupled to the upper vertical arm (T_2) is higher than the power coupled to the forward (T_3) and the lower vertical (T_4) arms.
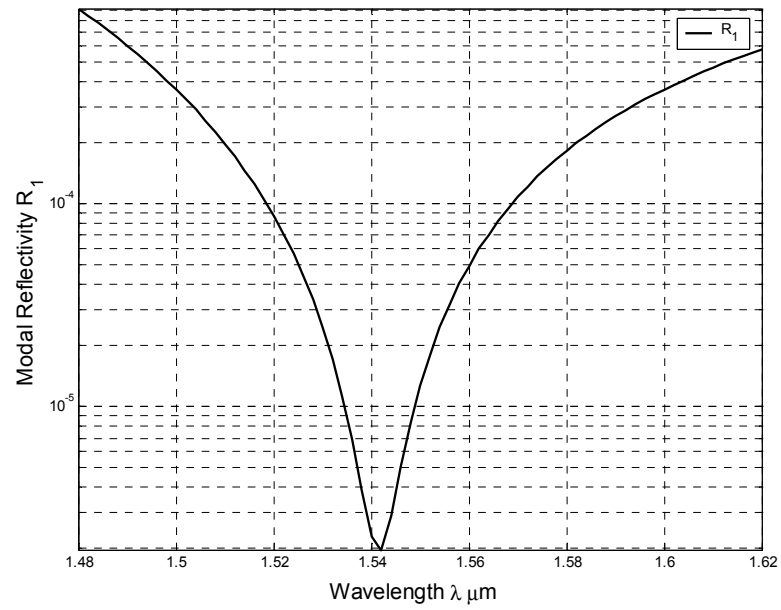
Figure 6-23 Modal reflectivity spectrum of the beam splitter
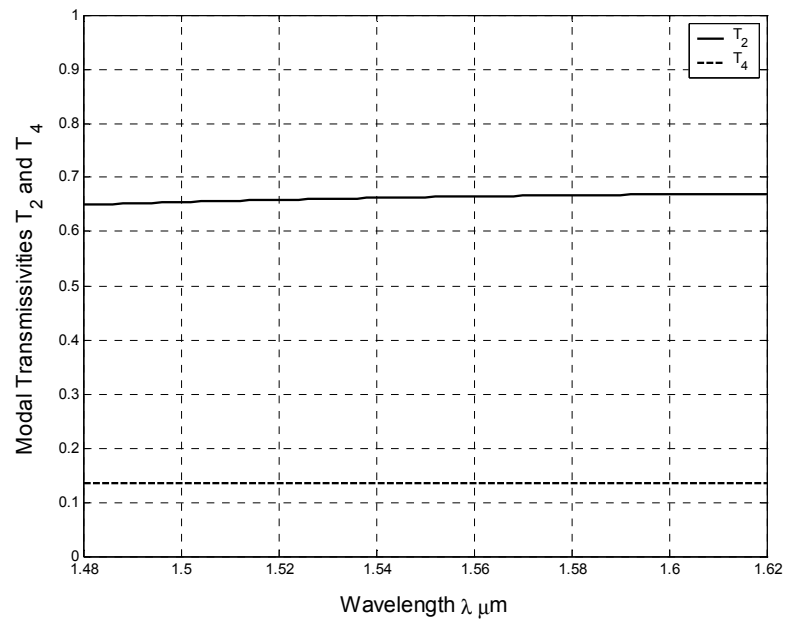
Figure 6-24 Modal transmissivity spectrum in the vertical arms
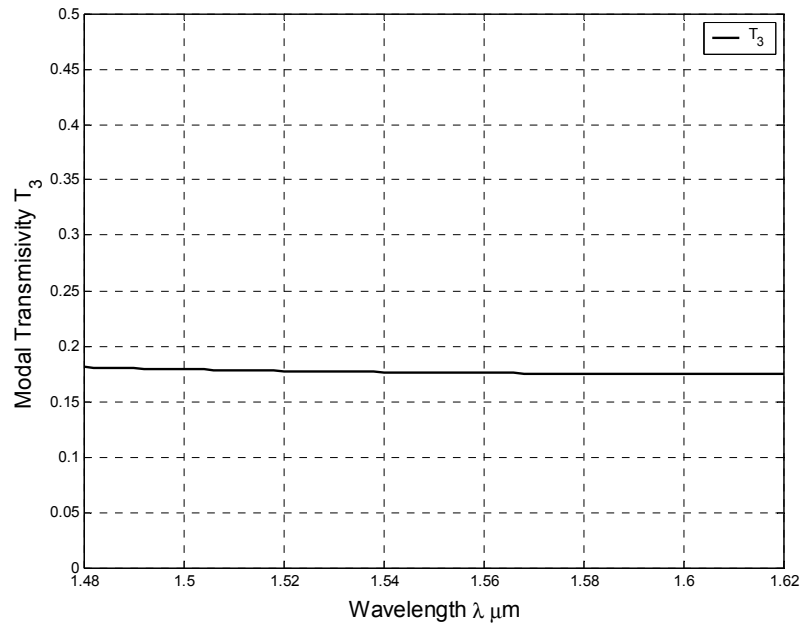
Figure 6-25 Modal transmissivity spectrum in the forward arm
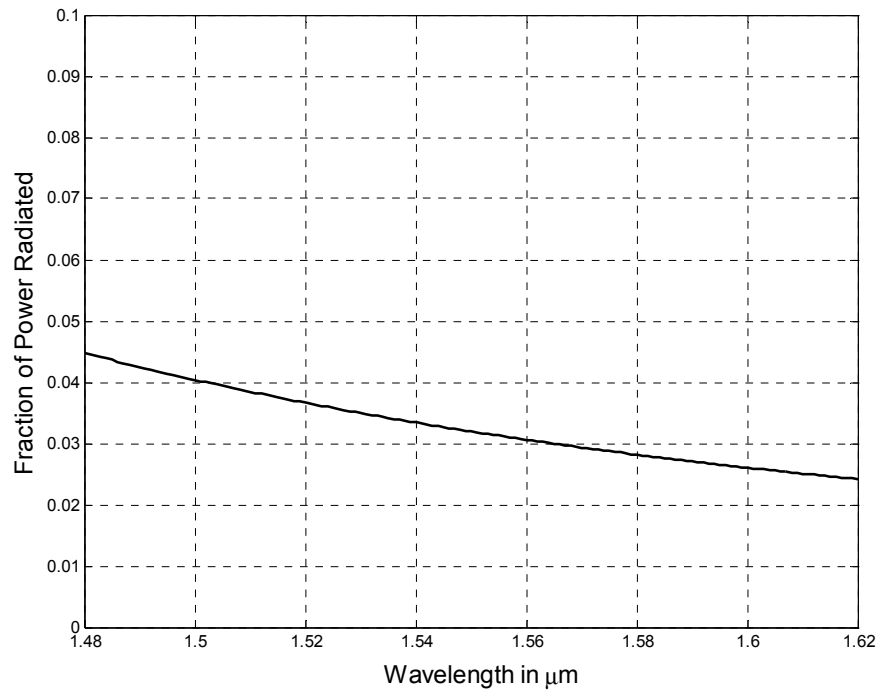
Figure 6-26 Variation of the fraction of radiated power with wavelength
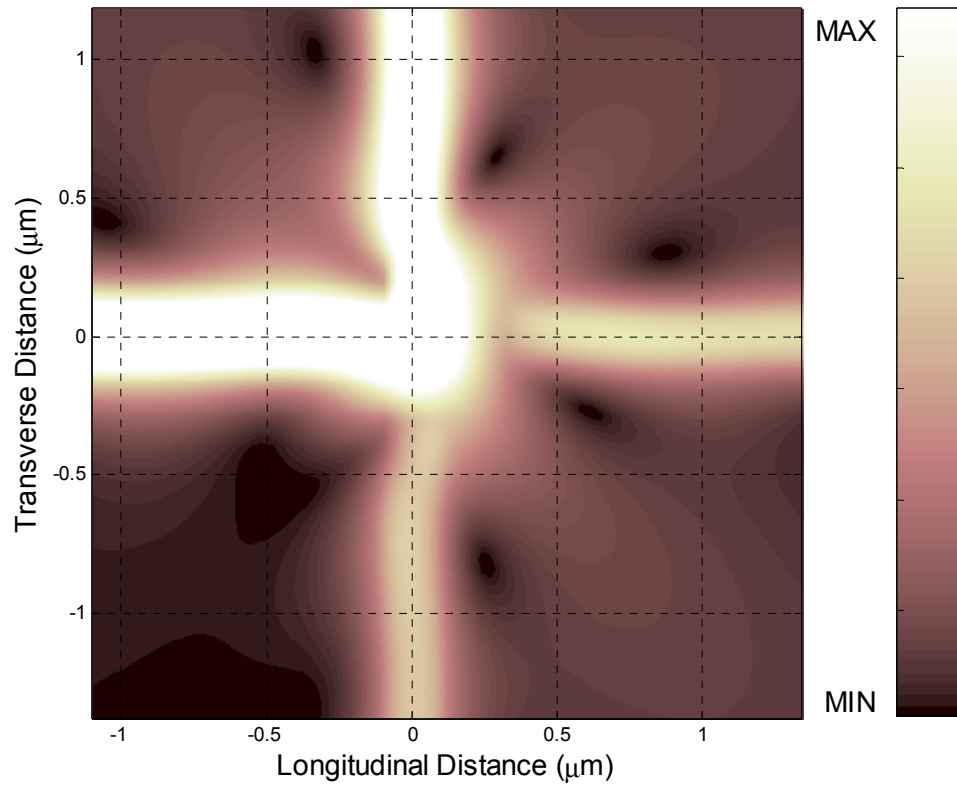
Figure 6-27 Field intensity image showing higher power coupling in the upper vertical arm

6.3. CONCLUSION

The proposed novel three way 90^0 beam splitter provides flexibility with regards to the coupling of power in all the three arms and has a wide controllability range. The spectral response of all the cases presented show relatively wide spectral responses, which is an important advantage of the proposed device. In addition, it is relatively easy to tune

the device for a certain power distribution. Finally, the radiation loss of the proposed beam splitter is relatively low.

CHAPTER 7

CONCLUSION AND FUTURE WORK

7.1. SUMMARY

In this thesis work we have presented an important extension to the Method of Lines, by use of Padé approximants. In addition, several types of waveguide junctions have been analyzed. A summary of the several key points covered in this thesis work is as follows:

- o Higher order approximation of $\dfrac{\partial^2}{\partial x^2}$ (transverse second derivative operator) was incorporated in the *MOL* and verified for accuracy.

- o A perfectly-matched layer using a non-uniform loss profile was incorporated into the *MOL* and verified for accuracy.

- o A general routine for obtaining Padé primes from Taylor series expansion of a given function was presented and tested for accuracy.

- o The implementation and verification of the square root operator using Padé approximants with branch cut rotation.

o Calculation and verification of the reflected field at a single longitudinal discontinuity using Padé approximants.

o The calculation and verification of the field propagation in longitudinally uniform media was implemented using Padé approximants.

o A general approach for implementing Padé approximants was presented in the *MOL* framework, which leads to the general *PBPM* approach. The general *PBPM* approach ability to account for multiple longitudinal discontinuities was tested and verified in various situations.

o We have utilized the BICGSTAB numerical routine for obtaining the reflected field from a single longitudinal discontinuity as well as in the general *PML* approach.

o We have studied in some details a high contrast linearly tapered symmetric beam expander as well as its asymmetric version.

o Waveguide crossings that utilize a resonant cavity were also studied for both the square and the octagonal cavity shapes.

o Finally, a novel three way 90^0 beam splitter that also utilizes a resonant cavity was analyzed in some detail.

7.2. CONCLUSION

o The general *PBPM* approach presented in this thesis produced accurate results in a variety of guided-wave problems.

o The general *PBPM* is generally much more memory efficient than the *MOL*. The CPU time requirement of the *MOL* is smaller than the requirement of the *PBPM* when the number of mesh points is relatively small ($M \leq 350$ points). However, the *PBPM* becomes much more time efficient for large values of M.

o The *MOL* and the *PBPM* time requirements are proportional to N^3 and N, respectively.

o The maximum longitudinal step size Δz in the *PBPM* is independent of the transverse mesh size Δx.

o It is necessary to use branch-cut rotation along with Padé approximants in the *PBPM* in order to account for the evanescent part of the field correctly. In addition, the complex factor $\gamma = \alpha e^{j\theta}$, which causes branch-cut rotation, has to have a low magnitude α for enhanced accuracy.

o Padé orders of $p = 4$ for the square root operator and $p = 10$ for the propagation operator were found to be sufficient for all the problems considered in this thesis.

o Generally speaking a branch-cut rotation angle of $\theta = -90^0$ is adequate for all the problems considered.

o From the analysis of the symmetric beam expander it can be concluded that, for efficient coupling of the input and the output waveguide cores, the distance joining them should not exceed a certain value. As the distance increases, the fraction of power transmitted to the output waveguide is reduced.

o A similar behavior was observed in the case of the asymmetric beam expander studied.

o For the two variants of beam expanders studied, as the output waveguide core width increases, the modal reflectivity increases and thus the fraction of power transmitted in the output waveguide decreases.

o The *WC* with octagonal cavity is observed to be superior to the *WC* with square cavity and the simple *WC*, in terms of lower modal reflectivity, lower fraction of power radiated and higher modal transmissivity. However, it gives a higher value of the crosstalk.

o A minimum modal reflectivity of about 2×10^{-5} at $\lambda = 1.564$ µm is achieved for the *WC* with octagonal cavity. Whereas, for the *WC* with square cavity the minimum modal reflectivity is about 1.5×10^{-4} at $\lambda = 1.57$ µm.

o The air gaps between the rectangular cavity and the four arms, and the width and the height of the cavity, in the three way beam splitter play an important role in deciding the amount of power flow to each arm.

o With, proper tuning of the parameters a_1, a_2, a_3, a_4, w and h, the power flow in any of the output arms of the three way beam splitter can be controlled over a wide range of values.

7.3.   FUTURE WORK

o The developed general *PBPM* method can be used to analyze complex 2-D problems which require higher number of discretization points.

o This method can be considered as an initial step forward in the analysis of 3-D problems, which require higher number of discretization points (in the order of thousands) and thus cannot be analyzed using the *MOL*.

o An alternate to the BICGSTAB subroutine can be developed which minimizes the computational time required, thereby making the general *PBPM* much more time efficient.

o The developed general *PBPM* can be formulated in order to compute just the reflected and the transmitted fields without actually computing the field inside the structure. This may lead to further reduction in the CPU time and memory requirements.

o Different types of Padé polynomials may be investigated, such as the mini-max polynomial and the chebychev polynomials. These special polynomials may extend the range of Padé approximants beyond the current range.

APPENDICES

MAIN PROGRAM

%% This is the main program which computes the entire field for a multiple
%% discontinuity structure.

clear all;close all;clc;
format long e;

global I whichpt TE lambda w d_x m Xp d exp_order sq_order bcr exp_a exp_b c0 sq_a
sq_b d_z;

whichpt=5; %% ORDER OF APPROXIMATION 3,5 OR 7.

w=[1 0.3 0.3 2.5]; %% w = WIDTH OF EACH LAYER

n=[1 1 3.6 3.4   %% REFRACTIVE INDEX PROFILE
    1 3.6 3.6 3.4
    1 1 3.6 3.4];

M=10*[2 2 2 4]; %% NUMBER OF DISCRETIZATION POINTS IN EACH LAYER

lambda=1.00;   %% WAVELENGTH
k0=2*pi/lambda; %% WAVE NUMBER
TE=1; %% 1 FOR TE AND 0 FOR TM MODE

pmlsup=10; %% NUMBER OF POINTS IN PML ABOVE SUPERSTRATE
etasup=1.2; %% VALUE OF ETA IN PML ABOVE SUPERSTRATE

pmlsub=10; %% NUMBER OF POINTS IN PML BELOW SUBSTRATE
etasub=1.2;   %%   VALUE   OF   ETA   IN   PML   BELOW   SUBSTRATE

d=[0.5]; %% DISCONTINUITIES

exp_order=10; sq_order=4;
%% EXPONENTIAL AND SQUARE ROOT FUNCTION ORDER

bcr=(1.5*k0)^-2*exp(-j*0.5*pi); %% COMMON BRANCH CUT ROTATION VALUE

[d_x,n,M,w]=pml(pmlsup,etasup,pmlsub,etasub,n,M,w);   %%   FUNCTION   FOR
ADDING THE PML LAYERS

N=[]; %% REFRACTIVE INDEX MATRIX
m=length(d_x); %% TOTAL MESH POINTS
I=speye(m,m); %% IDENTITY MATRIX
x=[];

%% CALCULATING THE Q AND N MATRIX AND STORING THE BRANCH CUT
%% ROTATED VALUE OF Q

for i=1:1:length(n(:,1))
    [qq,nn]=gensol(n(i,:),M,k0);
    X=bcr*qq-I;
    clear qq;
    Xp=[Xp;X]; %% STORING BRANCH CUT ROTATED VALUES OF Q
    clear X
    N=[N;nn];
    clear nn

end

%% FINDING THE FUNDAMENTAL MODE OF THE INPUT WAVEGUIDE

[U0,V0] = eigs(bcr.^-1*(Xp(1:m,1:m)+I),1,k0*k0*3.462^2);
A0=U0/max(abs(U0)); %% FUNDAMENTAL MODE
clear U0 V0;

%% EVALUATING THE PADE PRIMES FOR SQUARE ROOT FUNCTION

```
i=1:1:sq_order;
sq_a=(sin((i.*pi)/(2*sq_order+1))).^2;
sq_b=(cos((i.*pi)/(2*sq_order+1))).^2;
clear i;

d_z=0.1; %% PROPAGATION STEP

g=j*d_z*bcr^-0.5;
[exp_a,exp_b,c0]=exp_aandb(g);
%% FINDING THE PADE PRIMES FOR THE EXPONENTIAL FUNCTION

%% Kn REPRESENT THE CONSTANT MATRIX IN THE DERIVATION IN THE
%% THESIS

Kn=[-sq(A0,Xp(1:2*m,1:m),1,-1)
   spalloc(m*length(d),1,1)
   A0
   spalloc(m*length(d),1,1)];

%% THIS THE MAIN FUNCTION FOR COMPUTING THE FIELD

[Un,flag,relres,iter]=bicgstab(@muldisc,Kn,[],200);

if flag~=0; 'WARNING bicgstab did not converge',flag,end;

%% GENERATING THE X AXIS

x=x_axis(n(1,:),M);
```

PML

```
%% THIS FUNCTION ADDS THE PML LAYERS AT THE SUBSTRATE AND THE
%% SUPERSTRATE WITH THE CHOOSEN PML PROFILE. IN THIS THESIS
%% WORK ONLY THE TANGENT PROFILE IS USED
```

```
function [d_x,n,M,w]=pml(pmlsup,etasup,pmlsub,etasub,n,M,w);

h=w./M;        %% DELTA X IN EACH REGION
d_x=[];

%% DELTA X WITHOUT PML

for k=1:1:length(n(1,:))
   d_x=[d_x h(k)*ones(1,M(k))];
end

%% ADDING PML LAYER

if pmlsup~=0   %% JUST TO CHECK THAT THERE IS A PML LAYER
   M=[pmlsup M];h=[h(1) h];
   for i=1:1:length(n(:,1))
      n1(i,:)=[n(i,1)];
    end

   for i=1:1:pmlsup
      xi=(i*pi)/(2*(pmlsup+1));
      img(i)=(etasup/pmlsup)*tan(xi);
%% tan(xi) TANGENT PROFILE. CHANGE TO ANY APPROPRIATE FUNCTION
      invimg(pmlsup+1-i)=img(i);
   end
   d_x=[h(1)*(ones(size(invimg)))+invimg*j d_x];
   w=[h(1)*pmlsup w];
end

if pmlsub~=0    %% JUST TO CHECK THAT THERE IS A PML LAYER
   M=[M pmlsub];h=[h h(end)];
   for i=1:1:length(n(:,1))
      n2(i,:)=[n(i,end)];
   end
   for i=1:1:pmlsub
      xi=(i*pi)/(2*(pmlsub+1));
```

```
        imgt(i)=(etasub/pmlsub)*tan(xi);
    end


    d_x=[d_x h(end)*(ones(size(invimg)))+imgt*j];
    w=[w h(end)*pmlsub];
end

if length(n1)~=0
n=[n1 n];
end
if length(n2)~=0
    n=[n n2];
end
```

GENSOL

```
%% GENERATES THE Q MATRIX
%% GENERATES THE N MATRIX
%% ALL THE VARIABLES USED ARE ALREADY DEFINED IN THE MAIN
%% PROGRAM

function [Qs,Ns,xaxis]=gensol(n1,M,k0)

%% n_x = REFRACTIVE INDEX COLUMN VECTOR WITH PML

n_x=[];

for k=1:1:length(n1)
    n_x=[n_x n1(k)*ones(1,M(k))];
end

%% USING SPARSITY FOR N

nx=n_x.^2;
```

```
nx=nx.';
Ns=spdiags(nx,0,length(nx),length(nx));

[Dxx]=dxx(n_x,k0);
```

%% COMPUTING THE Q MATRIX

```
Qs=Dxx+k0^2*Ns;
```

Dxx

```
function [Dxx]=dxx(n_x,k0);
global whichpt TE lambda d_x;
m=length(n_x);
if whichpt==5
   a2=[0 0 (-1/12)*d_x(1:end-2).^-2];
   a1=[0 (16/12)*d_x(1:end-1).^-2];
   a0=(-30/12)*d_x.^-2;
   a_1=[(16/12)*d_x(2:end).^-2 0];
   a_2=[(-1/12)*d_x(3:end).^-2 0 0];
   t=[a_2.' a_1.' a0.' a1.' a2.'];
    clear a2 a1 a0 a_1 a_2;

   Dxx=spdiags(t,-2:2,m,m);
   clear t;

   for i=2:1:m-2
      Nn1=n_n(whichpt,d_x(i));
      Np1=n_p(whichpt,d_x(i+1));
      Mn1=m_n(whichpt,i-1,n_x,k0,TE);
      Mp1=m_p(whichpt,i,n_x,k0,TE);
      Mp2=m_p(whichpt,i+1,n_x,k0,TE);
      qn(1:2,:)=q_n(whichpt,d_x(i-1:i).');
```

```
        qp(1:2,:)=q_p(whichpt,d_x(i+1:i+2).');
        C=[qn(1,:)*Mn1*Nn1
            qn(2,:)
            1 0 0 0 0
            qp(1,:)*Mp1
            qp(2,:)*Mp2*Np1*Mp1];
        Cm=(C)^-1;
        if i>2
            Dxx(i,i-2:i+2)=Cm(3,:);
        end
    end

end

if whichpt==3
    a0=-2*d_x.^-2;
    a1=[0 d_x(1:end-1).^-2];
    a_1=[d_x(2:end).^-2 0];
    t=[a_1.' a0.' a1.'];
     clear a1 a0 a_1;
    Dxx=spdiags(t,-1:1,m,m);
     clear t;

    for i=1:1:m-1
        qn1=q_n(whichpt,d_x(i));
        qp1=q_p(whichpt,d_x(i+1));
        Mp1=m_p(whichpt,i,n_x,k0,TE);

        C=[qn1
            1 0 0
            qp1*Mp1];

        Cm=C^-1;
        if i>2
            Dxx(i,i-1:i+1)=Cm(3,:);
        end
```

```
      end
end

if whichpt==7
   e=(2/180)*d_x.^-2;
   c=(-490/180)*d_x.^-2;
   a=(-27/180)*d_x.^-2;
   b=(270/180)*d_x.^-2;

   a3=[0 0 0 e(1:end-3)];
   a2=[0 0 a(1:end-2)];
   a1=[0 b(1:end-1)];
   a0=[c];
   a_1=[b(2:end) 0];
   a_2=[a(3:end) 0 0];
   a_3=[e(4:end) 0 0 0];
   t=[a_3.' a_2.' a_1.' a0.' a1.' a2.' a3.'];
   Dxx=spdiags(t,-3:3,m,m);
   clear t;
   for i=3:1:m-3
      Nn1=n_n(whichpt,d_x(i-1));
      Nn2=n_n(whichpt,d_x(i));
      Np1=n_p(whichpt,d_x(i+1));
      Np2=n_p(whichpt,d_x(i+2));

      Mn1=m_n(whichpt,i-2,n_x,k0,TE);
      Mn2=m_n(whichpt,i-1,n_x,k0,TE);

      Mp1=m_p(whichpt,i,n_x,k0,TE);
      Mp2=m_p(whichpt,i+1,n_x,k0,TE);
      Mp3=m_p(whichpt,i+2,n_x,k0,TE);
      qn(1:3,:)=q_n(whichpt,d_x(i-2:i).');
      qp(1:3,:)=q_p(whichpt,d_x(i+1:i+3).');

      C=[qn(1,:)*Mn1*Nn1*Mn2*Nn2
```

```
        qn(2,:)*Mn2*Nn2
        qn(3,:)
        1 0 0 0 0 0 0
        qp(1,:)*Mp1
        qp(2,:)*Mp2*Np1*Mp1
        qp(3,:)*Mp3*Np2*Mp2*Np1*Mp1];


    Cm=C^-1;
    if i>4
        Dxx(i,i-3:i+3)=Cm(3,:);
    end


    end
end
```

M_P


```
%% This function computes M+

function [Mp]=m_p(whichpt,i,n_x,k0,TE);

if TE==1
   r=1;      %row
elseif i==length(n_x)
   r=1;
else
   r=n_x(i+1)^2/n_x(i)^2;
end

if i==length(n_x)
   sig=0;        %sigma
else
   sig=(k0^2)*(n_x(i+1)^2-n_x(i)^2);
end
```

```
if whichpt==5
   Mp=[1 0 0 0 0
      0 r 0 0 0
      -sig 0 1 0 0
      0 -sig*r 0 r 0
      sig^2 0 -2*sig 0 1];
elseif whichpt==3
   Mp=[1 0 0
      0 r 0
      -sig 0 1];
elseif whichpt==7
   Mp=[1 0 0 0 0 0 0
      0 r 0 0 0 0 0
      -sig 0 1 0 0 0 0
      0 -sig*r 0 r 0 0 0
      sig^2 0 -2*sig 0 1 0 0
      0 sig^2*r 0 -2*r*sig 0 r 0
      -sig^3 0 3*sig^2 0 -3*sig 0 1
   ];
end
```

M_N

```
%% This function computes M-

function [Mn]=m_n(whichpt,i,n_x,k0,TE);

if TE==1
   r=1;      %row
elseif i==length(n_x)
   r=1;
else
   r=n_x(i+1)^2/n_x(i)^2;
end
```

```
if i==length(n_x)
   sig=0;        %sigma
else
   sig=(k0^2)*(n_x(i+1)^2-n_x(i)^2);
end

if whichpt==5
   Mn=[1 0 0 0 0
      0 r^-1 0 0 0
      sig 0 1 0 0
      0 sig*r^-1 0 r^-1 0
      sig^2 0 2*sig 0 1];

elseif whichpt==3
   Mn=[1 0 0
      0 r^-1 0
      sig 0 1];

elseif whichpt==7
   Mn=[1 0 0 0 0 0 0
      0 r^-1 0 0 0 0 0
      sig 0 1 0 0 0 0
      0 sig*r^-1 0 r^-1 0 0 0
      sig^2 0 2*sig 0 1 0 0
      0 sig^2*r^-1 0 2*r^-1*sig 0 r^-1 0
      sig^3 0 3*sig^2 0 3*sig 0 1];
end
```

N_P

```
%% This function computes N+

function [Np]=n_p(whichpt,h);
```

```
if whichpt==5
   Np=[1 h h^2/2 h^3/6 h^4/24
       0 1 h h^2/2 h^3/6
       0 0 1 h h^2/2
       0 0 0 1 h
       0 0 0 0 1];

elseif whichpt==7
   Np=[1 h h^2/2 h^3/6 h^4/24 h^5/120 h^6/720
       0 1 h h^2/2 h^3/6 h^4/24 h^5/120
       0 0 1 h h^2/2 h^3/6 h^4/24
       0 0 0 1 h h^2/2 h^3/6
       0 0 0 0 1 h h^2/2
       0 0 0 0 0 1 h
       0 0 0 0 0 0 1];
end
```

N_N

```
%% This function computes N-

function [Nn]=n_n(whichpt,h);
if whichpt==5
   Nn=[1 -h h^2/2 -h^3/6 h^4/24
       0 1 -h h^2/2 -h^3/6
       0 0 1 -h h^2/2
       0 0 0 1 -h
       0 0 0 0 1];

elseif whichpt==7
   Nn=[1 -h h^2/2 -h^3/6 h^4/24 -h^5/120 h^6/720
       0 1 -h h^2/2 -h^3/6 h^4/24 -h^5/120
       0 0 1 -h h^2/2 -h^3/6 h^4/24
       0 0 0 1 -h h^2/2 -h^3/6
```

```
        0 0 0 0 1 -h h^2/2
        0 0 0 0 0 1 -h
        0 0 0 0 0 0 1];
end
```

Q_P

```
%% Computes Q+

function qp=q_p(whichpt,h);
if whichpt==5
    qp(:,1:whichpt)=[ones(length(h),1) h h.^2/2 h.^3/6 h.^4/24];
elseif whichpt==3
    qp(:,1:whichpt)=[ones(length(h),1) h h.^2/2];
elseif whichpt==7
    qp(:,1:whichpt)=[ones(length(h),1) h h.^2/2 h.^3/6 h.^4/24 h.^5/120 h.^6/720];
end
```

Q_N

```
%% Computes Q-

function qn=q_n(whichpt,h);
if whichpt==5
    qn(:,1:whichpt)=[ones(length(h),1) -h h.^2/2 -h.^3/6 h.^4/24];
elseif whichpt==3
    qn(:,1:whichpt)=[ones(length(h),1) -h h.^2/2];
elseif whichpt==7
    qn(:,1:whichpt)=[ones(length(h),1) -h h.^2/2 -h.^3/6 h.^4/24 -h.^5/120 h.^6/720];
end
```

EXP_AANDB

```
%% COMPUTES THE PADE PRIMES FOR THE EXPONENTIAL FUNCTION
%% RETURNS THE PADE PRIMES FOR THE NUMERATOR AND THE
%% DENOMINATOR WITH THE CONSTANT AT ZERO

function [aa,bb,c0]=exp_aandb(g);

global exp_order

c=expcoeff(g);
%% TAYLOR SERIES EXPANSION COEFFICIENTS OF EXPONENTIAL
%% FUNCTION

C=zeros(exp_order,exp_order);
%% INITIALIZATION INORDER TO SAVE MEMORY

%% CHECK THE THESIS FOR THE BELOW IMPLEMENTED STEPS.

for i=exp_order:-1:1
   C=C+diag((c(i+1)*ones(i,1)).',-exp_order+i);
end

for i=1:1:exp_order-1
   C=C+diag((c(exp_order+i+1)*ones(exp_order-i,1)).',i);
end

CC=rot90(-c(1,exp_order+2:2*exp_order+1));

b=C\CC;
clear C;

C1=zeros(exp_order,exp_order);

for i=1:1:exp_order
```

```
    C1=C1+diag((c(i)*ones(1,exp_order-i+1)).',i-1);
end

CC1=rot90(c(2:exp_order+1));

a=C1*b+CC1;
clear C1 CC1;

a=flipud(a);
a=[c(1) a.'];

b=flipud(b);
b=[1 b.'];

a=fliplr(a);
b=fliplr(b);
c0=a(end);
aa=roots(a);
bb=roots(b);
aa=-1./aa;
bb=-1./bb;
```

EXPCOEFF

```
%% THIS FUNCTION COMPUTES THE TAYLOR SERIES COEFFICIENTS OF THE
EXPONENTIAL
%% FUNCTION USING BUILT IN SYMBOLIC FUNCTIONS IN MATLAB

function c=expcoeff(g);

global exp_order;

c=exp(g)*[1
    1/2*g
```

(-1/8*g+1/8*g^2)

(1/16*g-1/16*g^2+1/48*g^3)

(-5/128*g+5/128*g^2-1/64*g^3+1/384*g^4)

(7/256*g-7/256*g^2+3/256*g^3-1/384*g^4+1/3840*g^5)

(-21/1024*g+21/1024*g^2-7/768*g^3+7/3072*g^4-1/3072*g^5+1/46080*g^6)

(33/2048*g-33/2048*g^2+15/2048*g^3-1/512*g^4+1/3072*g^5-1/30720*g^6+1/645120*g^7)

(-429/32768*g+429/32768*g^2-99/16384*g^3+55/32768*g^4-5/16384*g^5+3/81920*g^6-1/368640*g^7+1/10321920*g^8)

(715/65536*g-715/65536*g^2+1001/196608*g^3-143/98304*g^4+55/196608*g^5-11/294912*g^6+1/294912*g^7-1/5160960*g^8+1/185794560*g^9)

(-2431/262144*g+2431/262144*g^2-143/32768*g^3+1001/786432*g^4-1001/3932160*g^5+143/3932160*g^6-11/2949120*g^7+11/41287680*g^8-1/82575360*g^9+1/3715891200*g^10)

(4199/524288*g-4199/524288*g^2+1989/524288*g^3-221/196608*g^4+91/393216*g^5-91/2621440*g^6+91/23592960*g^7-13/41287680*g^8+1/55050240*g^9-1/1486356480*g^10+1/81749606400*g^11)

(-29393/4194304*g+29393/4194304*g^2-20995/6291456*g^3+4199/4194304*g^4-221/1048576*g^5+1547/47185920*g^6-91/23592960*g^7+13/37748736*g^8-13/566231040*g^9+13/11890851840*g^10-1/29727129600*g^11+1/1961990553600*g^12)

(52003/8388608*g-52003/8388608*g^2+24871/8388608*g^3-11305/12582912*g^4+1615/8388608*g^5-323/10485760*g^6+119/31457280*g^7-17/47185920*g^8+1/37748736*g^9-1/679477248*g^10+1/16986931200*g^11-1/653996851200*g^12+1/51011754393600*g^13)

(-185725/33554432*g+185725/33554432*g^2-22287/8388608*g^3+81719/100663296*g^4-17765/100663296*g^5+969/33554432*g^6-323/88080384*g^7+323/880803840*g^8-17/587202560*g^9+17/9512681472*g^10-1/11890851840*g^11+1/348798320640*g^12-1/15695924428800*g^13+1/1428329123020800*g^14)

(334305/67108864*g-334305/67108864*g^2+482885/201326592*g^3-37145/50331648*g^4+81719/503316480*g^5-81719/3019898880*g^6+3553/1006632960*g^7-323/880803840*g^8+323/10569646080*g^9-323/158544691200*g^10+17/158544691200*g^11-17/3923981107200*g^12+1/42849873690624000*g^15+1/7847962214400*g^13-1/408094035148800*g^14)

(-9694845/2147483648*g+1/13711959580999968000*g^16+9694845/2147483648*g^2-2340135/1073741824*g^3+1448655/2147483648*g^4-

482885/3221225472*g^5+81719/3221225472*g^6-
81719/24159191040*g^7+81719/225485783040*g^8-
3553/112742891520*g^9+323/144955146240*g^10-
323/2536715059200*g^11+323/55807731302400*g^12-1/11426632984166400*g^15-
17/83711596953600*g^13+17/3264752281190400*g^14)

(1/46620662575398912000*g^17+17678835/4294967296*g-
1/342798989524992000*g^16-17678835/4294967296*g^2+8554275/4294967296*g^3-
1330665/2147483648*g^4+596505/4294967296*g^5-
51129/2147483648*g^6+62491/19327352832*g^7-
24035/67645734912*g^8+4807/150323855360*g^9-
4807/2029372047360*g^10+209/1449551462400*g^11-
19/2657511014400*g^12+1/5078503548518400*g^15+19/66969277562880*g^13-
19/2176501520793600*g^14)

(-1/10969567664799744000*g^17-
64822395/17179869184*g+1/1678343852714360832000*g^18+19/27423919161999360
00*g^16+64822395/17179869184*g^2-
1964315/1073741824*g^3+9821575/17179869184*g^4-
2217775/17179869184*g^5+1153243/51539607552*g^6-
39767/12884901888*g^7+62491/180388626432*g^8-
312455/9740985827328*g^9+24035/9740985827328*g^10-
4807/30440580710400*g^11+437/52183852646400*g^12-
19/54847838323998720*g^15-19/52183852646400*g^13+19/1492458185687040*g^14)

(1/4387827065919897600*g^17+119409675/34359738368*g-
1/372965300603191296000*g^18-
1/78354054748569600*g^16+1/63777066403145711616000*g^19-
119409675/34359738368*g^2+57998985/34359738368*g^3-
1137235/2147483648*g^4+516925/4294967296*g^5-
723695/34359738368*g^6+303485/103079215104*g^7-
8671/25769803776*g^8+3289/103079215104*g^9-
16445/6493990551552*g^10+3289/19481971654656*g^11-
23/2435246456832*g^12+1/1899492236328960*g^15+23/52183852646400*g^13-
23/1356780168806400*g^14)

(-1/2279390683594752000*g^17-
883631595/274877906944*g+1/142082019277406208000*g^18+23/1139695341797376
000*g^16-1/13426750821714886656000*g^19+883631595/274877906944*g^2-
214937415/137438953472*g^3+135330965/274877906944*g^4-
3866599/34359738368*g^5+682341/34359738368*g^6-
144739/51539607552*g^7+268801/824633720832*g^8-
8671/274877906944*g^9+95381/37108517437440*g^10+1/25510826561258284646400
000*g^20-3289/18554258718720*g^11+299/28862180229120*g^12-
23/31658203938816000*g^15-
299/584459149639680*g^13+23/1085424135045120*g^14)

(1/10714547155728479551488000*g^21+23/31911469570326528000*g^17+1641030105/549755813888*g-23/1627484948086652928000*g^18-23/797786739258163200*g^16+1/4882454844259958784000*g^19-1641030105/549755813888*g^2+799476205/549755813888*g^3-126233085/274877906944*g^4+57998985/549755813888*g^5-3866599/206158430208*g^6+3866599/1443109011456*g^7-227447/721554505728*g^8+268801/8658654068736*g^9-268801/103903848824832*g^10-1/5102165312251656692928000*g^20+95381/519519244124160*g^11-8671/779278866186240*g^12+23/24547284284866560*g^15+299/519519244124160*g^13-23/909158677217280*g^14)

(-1/20408661249006627717120000*g^21-23/21601610170682572800*g^17-6116566755/2199023255552*g+23/954791169544169717760*g^18+1/4714400748520531002654720000*g^22+23/600044726963404800*g^16-23/53707003286859546624000*g^19+6116566755/2199023255552*g^2-745922775/549755813888*g^3+944835515/2199023255552*g^4-218038965/2199023255552*g^5+39017499/2199023255552*g^6-351509/137438953472*g^7+1757545/5772436045824*g^8-351509/11544872091648*g^9+268801/103903848824832*g^10+23/4081732249801325543424000*g^20-268801/1428677921341440*g^11+268801/22858846741463040*g^12-23/20001490898780160*g^15-8671/13715308044877824*g^13+667/22858846741463040*g^14)

(1/6802887083002209239040000*g^21+1/685765402243891200*g^17+11435320455/4398046511104*g-1/27202027622341017600*g^18-1/85716377245827836411904000*g^22-29/600044726963404800*g^16+1/13220185424457734555360*g^19-11435320455/4398046511104*g^2+5584691385/4398046511104*g^3-443229475/1099511627776*g^4+205399025/2199023255552*g^5-73943649/4398046511104*g^6+10743949/4398046511104*g^7-565471/1924145348608*g^8+229245/7696581394432*g^9-76415/29686813949952*g^10-1/8163464499602651086848000*g^20+198679/1039038488248320*g^11-11687/952451947560960*g^12+29/21334923625365504*g^15+11687/17144135056097280*g^13-899/27430616089755648*g^14+1/216862434431944426122117120000*g^23)

(-1/30142022767763634782208000*g^21-29/15361145010263162880*g^17-171529806825/70368744177664*g+29/5595845682310152192000*g^18+1/274292407186649076518092800*g^22+899/15361145010263162880*g^16-1/839376852346522828800*g^19+171529806825/70368744177664*g^2-41929508335/35184372088832*g^3+26682414395/70368744177664*g^4-3102606325/35184372088832*g^5+1684272005/105553116266496*g^6-41079805/17592186044416*g^7+139671337/492581209243648*g^8-

10743949/369435906932736*g^9+2827355/1108307720798208*g^10+1/44654848544835014492160*g^20-15283/79164837199872*g^11+198679/15674637765574656*g^12-899/576042937884868608*g^15-198679/274306160897556480*g^13+899/24936923717959680*g^14-1/37715205988164248021237760000*g^23+1/1040939685273332453861621760000*g^24)

(1/1594816019458393374720000*g^21+899/384028625256579072000*g^17+322476036831/140737488355328*g-899/130569732587236884480000*g^18-1/1172189774301919130419200000*g^22-899/130918849519288320000*g^16+29/16787537046930456576000*g^19-322476036831/140737488355328*g^2+157807422279/140737488355328*g^3-25157705001/70368744177664*g^4+58701311669/703687441776640*g^5-5336482879/351843720888320*g^6+2357980807/1055531162664960*g^7-336854401/1231453023109120*g^8+139671337/4925812092436480*g^9-139671337/55415386039910400*g^10-29/7974080097291966687360000*g^20+10743949/55415386039910400*g^11-565471/43540660459929600*g^12+15283/8727923301285888000*g^15+198679/261243962759577600*g^13-15283/391865944139366400*g^14+1/1160467876558899939115008000000*g^23-1/173489947545555540897693696000*g^24+1/52046984263666662269308108800000*g^25)

   (-29/2764347767061215182848000*g^21-15283/5446224140002394112000*g^17-1215486600363/562949953421312*g+899/1028731226444896665600000*g^18+29/174153909324856556519424000*g^22+15283/1945080050000855040000*g^16-899/3819164678176678871040000*g^19+1215486600363/562949953421312*g^2-74417546961/70368744177664*g^3+190178175567/562949953421312*g^4-44509785771/562949953421312*g^5+40639369617/2814749767106560*g^6-4515485513/2111062325329920*g^7+1114210711/4222124650659840*g^8-77735631/2814749767106560*g^9+440501909/1773292353277132800*g^10+899/16586086602367291097088000*g^20-10743949/55415386039910400*g^11+10743949/812758995252019200*g^12-15283/7924400203707187200*g^15-10743949/1358468606349803520000*g^13+565471/13584686063498035200*g^14-1/4789232506433555304284160000*g^23+1/514044289023868269326499840000*g^24-1/832751748218666596308929740800000*g^25+1/2706443181710666438004021657600000*g^26)

(899/5597804228298960745267200000*g^21+15283/466819212000205209600000*g^17+2295919134019/1125899906842624*g-899/8402745816003693772800*g^18-899/3134770367847418017349632000000*g^22-565471/6418764165002821632000*g^16+899/29409610356012928204800000*g^19-

2295919134019/1125899906842624*g^2+3376351667675/3377699720527872*g^3-
135054066707/422212465065984*g^4+63392725189/844424930131968*g^5-
697319977079/50665495807918080*g^6+103856166799/50665495807918080*g^7-
645069359/2533274790395904*g^8+12256317821/455989462271262720*g^9-
1114210711/455989462271262720*g^10-
899/1187413018124021976268800*g^20+440501909/2279947311356313600*g^11-
440501909/32916739307706777600*g^12+10743949/5135011332002257305600*g^15+
10743949/13166695723082711040*g^13-
10743949/244524349142964633600*g^14+29/689649480926431963816919040000*g^23
-
29/5948226772990475687920926720000*g^24+1/23792907091961902751683706880000
0*g^25-
1/4163758741093332981544648704000000*g^26+1/146147931812375987652217169510
4000000*g^27)

   (-899/391147817734971945123840000*g^21-
10743949/287560634592126409113600*g^17-
17383387729001/9007199254740992*g+33263/261418758720114917376000*g^18+899
/1994853870448356920131584000*g^22+10743949/1106002440738947727360000*g^1
6-899/2352768828481034256384000*g^19+17383387729001/9007199254740992*g^2-
4263849820321/4503599627370496*g^3+8199711192925/27021597764222976*g^4-
482335952525/6755399441055744*g^5+443749076323/3377699720527872*g^6-
697319977079/354658470655426560*g^7+697319977079/283726776524341248*g^8-
14836595257/567453553048682496*g^9+12256317821/5107081977438142464*g^10+8
99/8940521548227930174259200*g^20-
12256317821/638385247179767808*g^11+18941582087/14044475437954891776000*
g^12-10743949/4792677243202106818560*g^15-
440501909/52666782892330844160*g^13+440501909/95853544864042136371200*g^1
4-
899/120688659162125593667960832000*g^23+899/888268531433244369396191723520
00*g^24-
29/2664805594299733108188575170560000*g^25+29/333100699287466638523571896 3
2000000*g^26-
1/2165154545368533150403217326080000000*g^27+1/818428418149305530852416149
25824000000*g^28)

(31/993391283136436686028800000*g^21+370481/88480195259115818188800*g^17+32
968493968795/18014398509481984*g-21793/14746699209852636364800*g^18-
31/46937738128196633414860800000*g^22-
15189721/1437803172960632045568000*g^16+21793/470553765696206851276800000*g^
19-
32968493968795/18014398509481984*g^2+16184533402863/18014398509481984*g^3
-7792553119897/27021597764222976*g^4+3675732603725/54043195528445952*g^5-
56549732365/4503599627370496*g^6+76508461435/40532396646334464*g^7-

24045516451/101330991615836160*g^8+24045516451/945755921747804160*g^9-24045516451/10214163954876284928*g^10-1147/89405215482279301742592 00*g^20+9720527927/51070819774381424640*g^11-38421059/2837267765243412480*g^12+15189721/639023632426947 5758080*g^15+653158003/7660622966157213696 00*g^13-653158003/136933635520060194816 00*g^14+31/25815755970508148378173440000*g^23-31/16823267640781143359776358400 00*g^24+31/1332402797149866554094287585 28000*g^25-31/13324027971498665540942875852800000*g^26+1/57737454543160884010752462 028800000*g^27-1/116918345449900790121773735608320 00000*g^28+1/474688482526597207894401 3665697792000000*g^29)

(-1147/28233225941772411076608 0000*g^21-15189721/3286407252481444675584 000*g^17-125280277081421/72057594037927936*g+893513/530881171554694909132800 0*g^18+1/2848130895159583247366408199 41867520000000*g^30+1147/125167301675191 02243962880000*g^22+653158003/575121269184252818227 2000*g^16-21793/3981608786660211818496 000*g^19+125280277081421/72057594037927936*g^2-46155891556313/54043195528445952*g^3+19781096381277/72057594037927936*g^4-23377659359691/360287970189639680*g^5+7792553119897/648518346341351424*g^6-147029304149/81064793292668928*g^7+37161252697/162129586585337856*g^8-24045516451/972777519512027136*g^9+168318615157/729583139634020352 00*g^10+1147/72392887030185669427 20000*g^20-24045516451/127677049435953561 600*g^11+41533164779/3064249186462885478400*g^12-653158003/2614187587201149173760 00*g^15-883684357/10214163954876284928 00*g^13+653158003/1327841314133917040 6400*g^14-31/17210503980338765585448960 000*g^23+31/101787837826574985033940992 0000*g^24-31/71251486478602489523758694 400000*g^25+31/6056376350681211609519489024 000 00*g^26-31/6495463636105599451209651978 24000000*g^27+31/9353467635992063209741898 8486656000000*g^28-1/654742734519444424681932919 406592000000*g^29)

(37/7239288703018566942720000*g^21+1/176584115499894161336717308363957862 40000000*g^31+21069613/41827001395218386780 16000*g^17+238436656380769/144 115188075855872*g-1239389/6572814504962889351168000*g^18-1/379750786021277766315521093255823 36000000*g^30-37/30405012552677981159424 0000*g^22-21069613/17427917248007661158 4000*g^16+28823/455041004189738493542 4000*g^

19-238436656380769/144115188075855872*g^2+117197678560039/144115188075855872*g^3-28289094824837/108086391056891904*g^4+4466699182869/72057594037927936*g^5-8295298482471/720575940379279360*g^6+251372681287/144115188075855872*g^7-35910383041/162129586585337856*g^8+15583751131/648518346341351424*g^9-13186250957/583665117072162816*g^10-1517/79632175733204236369920000*g^20+5429632747/29183325585360814080*g^11-493602977/36479156981701017600*g^12+484601099/185897783978748385689600*g^15+1339779509/153212459323144273920 0*g^13-1339779509/2655682628267834081 2800*g^14+37/1449305598344317101932544 0000*g^23-37/7916831830955832169306521 60000*g^24+1/13571711710209998004525465 60000*g^25-1/101787837826574985033940992 000000*g^26+1/926269324221832363808863027200 0000*g^27-1/106289404954455263747067032371 2000000*g^28+1/1636856836298611061704832229851648000000*g^29)

   (-1517/2426885355678605298892800 00*g^21-1/22785047161276665978931265 59534940160000000*g^31-484601099/89230936309799225131008000*g^17-14544636039226909/9223372036854775808*g+1239389/5948729087319948342067200*g^18+1/92060796611218852440126325637775 36000000*g^30+1517/97296040168569 53971015680000*g^22+22776251653/17846187261959845026201 6000*g^16-1239389/17208823431175564846694 4000*g^19+14544636039226909/92233720368547 75808*g^2-3576549845711535/461168601842738790 4*g^3+6914663035042301/276701161105643 27424*g^4-820383749920273/13835058055282163712*g^5+254601853423533/23058430092136939 9520*g^6-19355696459099/11529215046068469760*g^7+1975071067255/9223372036854775808 *g^8-107731149123/4611686018427387904*g^9+825938809943/37354656749261842 0224*g^10+65231/291226242681432635867136000*g^20-171421262441/9338664187315460 50560*g^11+8391250609/622577612487697367040* g^12-1339779509/4957274239433290285056 00*g^15-493602977/560319851238927630336*g^13+9378456563/18210395165265147985 9200*g^14-37/107025644185426493681172480 00*g^23+1/113013833919932263255499077352933 0319360000000*g^32+37/54701995916995763437043712 0000*g^24-37/320006676114425216106705715 20000*g^25+37/21714738736335996807240744960 00000*g^26-1/470486005953946597490216140 8000000*g^27+1/45731239778723609276049008885 7600000*g^28-1/5602076872893642136316003588 5056000*g^29)

(65231/8736787280442979076014080000*g^21+1/536118756735921552445441543419985920000000*g^31+22776251653/392616119763116590576 4352000*g^17+27767032438524099/18446744073709551616*g-1339779509/58892417964467488586 46528000*g^18-1/3063535752776694585402523105257062400000*g^30-65231/3363663102970546944265420 80000*g^22-1339779509/10015717340895831392256000*g^16+28505947/353354507786804931518 7916800*g^19-27767032438524099/18446744073709551616*g^2+40989428837821289/553402322211 28654848*g^3-6611198199648595/27670116110564327424*g^4+3143028652291955/55340232221128 654848*g^5-4400240113208737/41505174165846491136 0*g^6+74580340901843/46116860184273879040*g^7-4776080944453/23058430092136939520*g^8+1256863406435/55340232221128654848 *g^9-179551915205/83010348331692982272*g^10-65231/25239607699057495108485120 0*g^20+825938809943/46565569158243114024960*g^11-825938809943/6163518363628203933696 0*g^12+1339779509/4807544323629999068288*g^15+109086257917/12327036727256407867 3920*g^13-8391250609/1602514774543333022 76096*g^14+1517/33636631029705469442654208 0000*g^23-1/14126729239991532906937384669116628992000000 0*g^32-1517/16246492787347741740801982464000*g^24+37/216619903831303223210693099 52000*g^25-37/13538743989454514506683187200000 0*g^26+37/9805918860934886979269767987 2000000*g^27-37/838406062609932836727565162905600000 0*g^28+1/2347536975307811942837182 4561356800000*g^29+1/74589130387155293748629391052935801077760000000*g^33)

  (-1500313/1716293323535909667376988160 00*g^21-1/17360035932401269317280964263123353600000 0*g^31-1339779509/21794200933789329109549056 0*g^17-106168065206121555/73786976294838206464*g+1339779509/544855023344733227737387264000*g^18+37/46293429153070051512749238034995609600000 0*g^30+65231/27724738303272386934551347200 0*g^22+1339779509/9615088647259998136565760*g^16-1339779509/15017566580939209589548646400 0*g^19+106168065206121555/73786976294838206464*g^2-1633354849324947/2305843009213693952*g^3+16878000109691119/73786976294838 206464*g^4-12055714364065085/221360928884514619392*g^5+2255585268115403/221360928884514619392*g^6-2588837653718161/16602069666338596454 4*g^7+36976807674023/184467440737095 5

16160*g^8-8147432199361/368934881474191032320*g^9+1404729689545/664082786653543858176*g^10+70514711/240281065295027353432778342400*g^20-14786628311/83010348331692982272*g^11+48584635879/3652455326594491219968*g^12-70514711/24654073454512815734784*g^15-48584635879/5478682989891736829952 0*g^13+26160957781/493081469090256314695680*g^14-65231/114364545500998596105024307200 00*g^23+1/322896668342663609301425935294094376 96000000*g^32+65231/5260769093045935420831118131 20000*g^24-1517/6312922911655122504997341757440 00*g^25+1517/368253836513215479458178269184000 00*g^26+1/50720608663265599749067985159963447328 7680000000*g^34-37/598412484333975154119539687424 00000*g^27+37/4616324879147808331779306160128000 000*g^28-37/42008556400245055819191686057164800 0000*g^29-1/904110671359458106043992618823464255488 0000000*g^33)

(70514711/7008197737716311417893683200 00*g^21+37/255832108477492389938877368088133632000 0000*g^31+1339779509/2070942170179076521721856 00*g^17+203236010537432691/147573952589676412928*g-1339779509/5085313551217510125561446400*g^18-37/2186599217756345213152798017847296000 0000*g^30-70514711/2522951185597787211044172595 20000*g^22-3737279683/25886777127238456521523 200*g^16+1339779509/13730346588287277339015905 2800*g^19-203236010537432691/147573952589676 412928*g^2+100101318622914609/147573952589676 412928*g^3-1011124430534491/461168601842738790 4*g^4+2411142872813017/46116860184273879040*g^5-7233428618439051/737869762948382064640*g^6+9989020473082499/6640827866535438581760*g^7-322226466873629/16602069666338596454 40*g^8+15847203288867/737869762948382064640*g^9-68671214251757/3320413933267719290880 0*g^10-70514711/21453666544198870842212352 0000*g^20+1163918885623/66408278665354385817 60*g^11-40135133987/30437127721620760166 40*g^12+3737279683/12783593643080719269888 00*g^15+48584635879/54786829898917368299520*g^13-3737279683/6972869259862210510848 0*g^14+1500313/213480848493519737939604537 3440000*g^23-37/376712779733107544184996924509776773120000000*g^32-65231/40917092945912831050908696576 0000*g^24+65231/20086572900720844334082 451046400000*g^25-65231/11047615095396464383 74534807552000000*g^26-1/59671304309724234998 903512842348640862208000 0000*g^34+1517/1595766624890600410985 439166464000000*g^27-1517/113099959539121304 12859300092313 6000000*g^28+37/22619991907824260825

7186001846272000000*g^29+1/200913482524324023565331693071880945664000000
0*g^33+1/35504426064285919824375901411974413130137600000000*g^35)

   (-70514711/617865596472927480255715737600 0*g^21-
37/11807635775884264151025109296375398400000 00*g^31-
3737279683/552251245381087072459161600*g^17-
1558142747453650631/11805916207174113034 24*g+71008313977/2534833216299189
6625875517440 0*g^18+1517/472305431035370566041004371855015936000000*g^30
+70514711/21625295876552461808950050816000 0*g^22+3737279683/2510232933550
3957839052800*g^16-
1339779509/126741660814959483129377587200*g^19+1/2556318676628586227353 02
6490166215774536990720000000 0*g^36+1558142747453650631/11805916207174113
03424*g^2-
1151670726378785249/17708874310761169551 36*g^3+745198705303919867/3541774
862152233910272*g^4-
11122368735879401/221360928884514619392*g^5+31344857346569221/33204139332
6771929088 0*g^6-
2411142872813017/16602069666338596454 40*g^7+9989020473082499/531266229322
8350865408 0*g^8-
9989020473082499/478139606390551577886720*g^9+322226466873629/15937986879
6850525962240*g^10+70514711/1938401871287615624331657216 00*g^20-
68671214251757/3984496719921263149056 00*g^11+68671214251757/5259535670296
067356753920*g^12-3737279683/125511646677519789195264 0*g^15-
1163918885623/13148839175740168391884 80*g^13+71008313977/1314883917574016
839188480*g^14-
70514711/832573891247269779644576956416000 0*g^23+37/146414683620964875472
71135527505494016000000 0*g^32+3065857/1537059491533421131651526688768000
0*g^24-
65231/153705949153342113165152668876800 00*g^25+65231/80346291602883377336
3298041856000000*g^26+37/47737043447779387999122810273878912689766400000
00*g^34-
65231/4700258058768677574175293544857600 0000*g^27+65231/31021703187873271
9895569373960601600000 0*g^28-
1517/542879805787782259817246404431052800 0000*g^29-
37/2284069064487052057374297142290857066496000000 0*g^33-
1/405764869306124797992543887327970757863014400000 00*g^35)

(1905803/14910783625289350956397363200 0*g^21+41/67472204433624366577286 33
88364308480000000*g^31+101007559/14344188191716547336601600*g^17+2989949
596465113373/236118324143482260684 8*g-
101007559/341391678962853826611118080*g^18-
1763/3148702873569137106940029145700106240000 00*g^30-
1905803/50883049121299910138706001920 00*g^22-
1919143621/125511646677519789195264 00*g^16+1919143621/168988881086612644 1

72503449600*g^19-1/2840354085142873585947807211295795305041100800000000*g^36-2989949596465113373/236118324143482260 6848*g^2+1473918815158858705/236118 3241434822606848*g^3-7159034245057 31371/354177486215223391 0272*g^4+34238859432882 8047/70835497 24304467820544*g^5-20140505548754591/22136092888451 46193920*g^6+9318741373304363/6640827866535438581760*g^7-121022615237719/6640827866535438 58176*g^8+269973526299527/132816557330708 77163520*g^9-1889814684096689/956279212781103155773440*g^10-101007559/2534833216299189662587551 74400*g^20+269973526299527/15937986879 68505259622400*g^11-113214704577221/8765892783826778927923200*g^12+55655165009/18408374846036 235748638720*g^15+1855978763561/2103814268118426942701568*g^13-142767597197/26297678351480336 78376960*g^14+1905803/190302603713661663918 760447180800*g^23-41/73207341810482437736355677637527470080000000*g^32-82861/33982607806011011414 0643655680000*g^24+82861/1537059491533421131651 5266887680000*g^25-82861/768529745766710565825763344384000000*g^26-1/3865347647593472712479579779261450420224000 0000*g^34+1763/9082624268152 03395975902134272000000*g^27-1763/56403096705224130890103522538291200000*g^28+1/189167582070515380824 123960272299967315737313 2800000000*g^37+1763/39482167693656891623072465 77 680384000000*g^29+1/2342634937935438007563381684400879042 56000000*g^33+1/8542418301181574694579871312167805428695040000000*g^35)

(-101007559/7135086090323644976172367872000*g^21-1763/163160057994037104632346964822641 86880000000*g^31-2929219211/40163726936806332542484 4800*g^17-11487701081155435591/944473296573929042 7392*g+101007559/325134932345575070 2962969600*g^18+1763/1933748835484884 20305003810160168140800000*g^30+101 007559/23797610665961804126401916672000*g^22+172823933449/1104502490 7621 74144918323200*g^16-101007559/8339711014664000621500170240*g^19+1/58263673541392278686108865 8 727342626675097600000000*g^36+11487701081155435591/9444732965739290427 39 2*g^2-1416291914115053703/236118324143482 2606848*g^3+5507801888225208845/28334 1 98897217871282176*g^4-1318769466194768315/28334198897217871282176*g^5+414470403661212899/472236 64828696452136960*g^6-18020452333096213/132816557 33070877163520*g^7+4694403548957837/2656331146 6141754327040*g^8-70065724611311/354177486215223391 0272*g^9+184718728520729/956279212781103 15577344*g^10+101007559/23351190841059201 7402004766720*g^20-99463930741931/597674507988189 472358400*g^11+99463930741931/7791904696734 914602598400*g^12-7514084063/24544997947 1498099818496*g^15-

184718728520729/21038142681184269427015 6800*g^13+458359127843/84152570724 73707770806272*g^14-
1905803/16360857332848740336907006 7712000*g^23+1763/158964513645619007656 0866142986310778880000000*g^32+82861/28358819376937816583972 1450700800*g^24-
82861/12396855327632816963850680559206400*g^25+82861/596002659982346969 415898103808000000*g^26+41/58753284243420785229689612644774046387404800000 0*g^34-
82861/316378078673962516264939243438 08000000*g^27+82861/18637544998247973 6854255117952 6144000000*g^28-
1/20450549413028689818824211921329726 1962959257600000000*g^37-
1763/26092562997547163159595716513366 01600000*g^29+1/14376736237359168942 63342098069479751599603580928 00000000*g^38-
41/42390536972165068 7082897638129682874368 0000000*g^33-
1/24970145803453833722618085374028 96971464704000000*g^35)

(101007559/65049745914379204847701327872 00*g^21+1763/98368962500752805111 67585125538988032000000*g^31+172823933449/2297365180785322221 4301122560* g^17+22091732848375837675/18889465931478580854784*g- 172823933449/532571019182051969513344204800*g^18- 82861/590213775004516830670055107 5323392819200000*g^30- 101007559/2124958366536387358358 24337715200*g^22- 458359127843/2871706475981652776787640320*g^16+2929219211/228244722506593 701220004659200*g^19- 41/68168498043428966062747373071099087320986419 20000000*g^36- 22091732848375837675/18889465931478580854784*g^2+32695764615596239759/566 68397794435742564352*g^3- 883669313935033507/47223664828696452 13696*g^4+4236770683250160 65/94447329 65739290427392*g^5- 1440502032305054621/17000519338330722 7693056*g^6+223176371202191561/17000 5193383307227693056*g^7- 4554619820452889/265633114661417 54327040*g^8+6138835410175633/31875973759 3701051924480*g^9-361107965304449/191255842556220631154688*g^10- 101007559/21683248638126401 6159004426240*g^20+156300462594463/95627921278 1103155773440*g^11- 99463930741931/788930350544410 1035130880*g^12+14209132963133/459473036157 0644442860224512*g^15+99463930741931/11395 660618974812606 3001600*g^13- 99463930741931/18233056990359700170080 25600*g^14+101007559/75623518338500 84422392572018688000*g^23- 1763/876713378287959375557811024 3136623 08352000000*g^32- 4391633/127614687196220174627874 65281536000*g^24+82861/1020917497569761 39 70229972225228800*g^25-82861/47399740958596064861 7820139028480000*g^26- 1763/109113242166352886855137852 0545803718 6232320000000*g^34+82861/241738 6788888399307950882709 0452480000*g^27-

82861/135978006874972461072237152383795200000*g^28+1/11213854265140151775254068364941942062476907931238400000000*g^39+1/409010988260573796376484238426594523925918515200000000*g^37+82861/8480082974202828026868607866843955200000*g^29-1/1513340656564123046592991682178399738525898506240000000*g^38+1763/9017623319533296434308913392940526600192000000*g^33+41/3709850233655998153074686969855732643318988800000*g^35)

(-2929219211/173465989105011212927203540992000*g^21-82861/29510688750225841533502755376616964096000000*g^31-14209132963133/18378921446282577714408980480*g^17-340212685864987900195/30223145490365729367654*g+10542259940389/3124416645868038221144952668160*g^18+82861/40150596939082777596602388267506073600000000*g^30+101007559/191725566905538709024803913728000*g^22+14209132963133/875186735537265608163852288800*g^16-172823933449/12781704460369247268320260915200*g^19+1763/1038758065423679482860912351559605140129316864000000000*g^36+340212685864987900195/3022314549036572936765544*g^2-83948584823828183165/15111572745182864683827200000000*g^3+163478823077981198795/9066943647109718810296320000000*g^4-32695764615596239759/75557863725914323419136000000*g^5+6185685197545234549/75557863725914323419136000000*g^6-1440502032305054621/113336795588871485128704000000*g^7+2263646050765085833/136004154706645782154444800000*g^8-31882338743170223/1700051933833072276930560*g^9+141193214434039559/76502337022488252461875200*g^10+172823933449/3469319782100224258544070819840000*g^20-6138835410175633/38251168511244126230937600*g^11+1/89710834121121214202032546919535536499815263449907200000000000*g^40+952011908529911/7650233702248252461875200*g^12-14209132963133/45582642475899250425200640000*g^15-99463930741931/1147535055337323786928128000*g^13+99463930741931/1823305699035970017008025600*g^14-101007559/66784405805429316976973363281920000*g^23+82861/2439550270018669566769561111133669031936000000000*g^32+4391633/109997844485600122796207377481728000*g^24-4391633/453741110031005065343554321121280000*g^25+4391633/20418349951395227940459944450457600000*g^26+1763/529033901412620057479456252385844227211264000000000*g^34-82861/18959896383438425944712805561139200000*g^27+82861/102383440470567500101449150030151680000*g^28-1/115013889898873351541067367845558380127968286474240000000*g^39-41/46744112944065576728741055820182231305819258880000000000*g^37-82861/609181470799876625603622442679402496000000*g^29+41/121067252525129843727439334574271979082071880499200000000*g^38-

1763/4879100540037339133539122222267338063872000000*g^33-
1763/6745182243010905732863067217919513896943616000000000*g^35)];

c=c(1:2*exp_order+1).';

MULDISC

```
%% IMPLEMENTS THE DERIVED MATRIX FORMULATION FOR THE
%% MULTIPLE LONGITUDINAL DISCONTINUITY CASE
%% sq AND tt ARE BOTH FUNCTIONS

function [Un]=muldisc(An);
global m Xp d;

ndis=length(d);  %% TOTAL NUMBER OF DISCONTINUITIES


A=An(1:(ndis+1)*m,1);
B=An((ndis+1)*m+1:end,1);


Un=[A(1:m,1)+sq(B(1:m,1),Xp(1:2*m,1:m),1,1)];
   for i=1:1:ndis
      Un=[Un; tt(A(m*(i-1)+1:m*i,1),Xp(m*i+1:m*(i+2),1:m),d(i),1,-
1)+A(m*i+1:m*(i+1),1)+sq(B(m*i+1:m*(i+1),1),Xp(m*i+1:m*(i+2),1:m),1,1)];
   end


Un=[Un; sq(A(1:m,1),Xp(1:m*2,1:m),-1,0)+B(1:m,1)-
tt(B(m+1:2*m,1),Xp(1:m*2,1:m),d(1),-1,0)];

   for i=1:1:ndis-1
```

```
    Un=[Un; sq(A(m*i+1:m*(i+1),1),Xp(m*i+1:m*(i+2),1:m),-
1,1)+B(m*i+1:m*(i+1),1)+tt(B(m*(i+1)+1:m*(i+2),1),Xp(m*i+1:m*(i+2),1:m),d(i+1),-
1,-1)];
  end
```

```
Un=[Un; sq(A(m*ndis+1:end,1),Xp(m*ndis+1:end,1:m),-1,1)+B(m*ndis+1:end,1)];
```

X_AXIS

%% THIS FUNCTION EVALUATES THE X AXIS FOR THE STRUCTURE

```
function xaxis=x_axis(n1,M)

global d_x

[dummy core]=max(n1);

x=cumsum(d_x);
x0=sum(d_x(1:sum(M(1:core-1))));
xaxis=x-x0;
xaxis=real(xaxis);
```

SQ

```
%% sq(field,X,K,L)
%% K controls the order of inverse K=1 for S1^-1*S0 and K=-1 for S0^-1*S1
%% L controls the sign L=1 is 0.5*(S1^-1*S0-I)*field and L=-1 is
%% -0.5*(I+S1^- 1*S0)*field
%% and if L=0 then it just returns S0^-1*S1*field
```

```
function R=sq(field,X,K,L);

global I m sq_a sq_b;

%% USING DIFFERENT VARIABLES FOR DIFFERENT LAYERS

X1=X(1:m,1:m);
X2=X(m+1:2*m,1:m);
clear X;

R=field;

if K==1
   for i=1:1:length(sq_a)
      R=(I+sq_a(i)*X1)*R;
      R=(I+sq_b(i)*X1)\R;
   end

   for i=1:1:length(sq_a)
      R=(I+sq_b(i)*X2)*R;
      R=(I+sq_a(i)*X2)\R;
   end

elseif K==-1
   for i=1:1:length(sq_a)
      R=(I+sq_a(i)*X2)*R;
      R=(I+sq_b(i)*X2)\R;
   end

   for i=1:1:length(sq_a)
      R=(I+sq_b(i)*X1)*R;
      R=(I+sq_a(i)*X1)\R;
   end
end

if L==0
```

```
      return;
elseif L==1
      R=0.5*(R-field);
elseif L==-1
      R=-0.5*(field+R);
end
```

Tт

```
%% E=tt(A,X,Z,K,L);
%% dont specify K,L to evaluate exp()*field==Pm*field
%% K controls the order of evaluation of the inverses
%% K=1 gives S1^-1*S0 and K=-1 gives S0^-1*S1
%% and L controls the sign L=1 is 0.5*(S1^-1*S0-I)*field
%% and L=-1 is -0.5*(I+S1^-1*S0)*field
%% and if L=0 then it just returns S0^-1*S1*P1*field

function E=tt(A,X,Z,K,L);

global I m exp_a exp_b c0 d_z;

field=A;

k1=floor(Z/d_z); %% TOTAL NUMBER OF STEPS
k2=rem(Z,d_z);  %% THE RESIDUE LESS THAN THE STEP

if nargin==3
    for i=1:1:k1
        field=trans_field(field,X);
    end
    if k2~=0
        field=trans_field(field,X,k2);
    end
end
```

```
if nargin>=4
   if K==1
     for i=1:1:k1
        field=trans_field(field,X(1:m,:));
     end
     if k2~=0
        field=trans_field(field,X(1:m,:),k2);
     end
   elseif K==-1
     for i=1:1:k1
        field=trans_field(field,X(m+1:end,:));
     end
     if k2~=0
        field=trans_field(field,X(m+1:end,:),k2);
     end
   end
end

if nargin==5
   E=sq(field,X,K,L);
else
   E=field;
End
```

TRANS_FIELD

```
%% This function computes the field (A) transmitted by a distance of d_z in
%% region defined by X

function field=trans_field(A,X,d_z);
global I bcr exp_order exp_a exp_b c0;
if nargin==2
   a=exp_a;
```

```
   b=exp_b;
   c1=c0;
end
if nargin==3
   g=j*d_z*bcr^-0.5;
   [a,b,c1]=exp_aandb(g);
end
field=c1*A;
clear A;

for k=1:1:length(a)
   field=field+a(k)*X*field;
   field=(I+b(k)*X)\field;
end
```

PROP

```
%% This function evaluates the propagated field after a distance Z.

function field=prop(A,Q,Z);

global I bcr d_z;



Xp=bcr*(Q)-I;
clear Q;
field=A;

k=floor(Z/d_z);
kk=rem(Z,d_z);
for i=1:1:k
   field=trans_field(field,Xp);
end
if kk~=0
```

```
   field=trans_field(field,Xp,kk);
end
```

SQ_FIELD

```
%%computes S*field;

function R=sq_field(field,X,bcr);
global I sq_a sq_b;

R=field;

for i=1:1:length(sq_a)
   R=(I+sq_a(i)*X)*R;
   R=(I+sq_b(i)*X)\R;
end
R=(bcr.^-0.5)*R;
```

SQRT_PROD

```
%computes the product S2^-1*S1*A

function [A]=sqrt_prod(A,Q2,Q1)


global I sq_a sq_b bcr;
Xp2=bcr*(Q2)-I;
Xp1=bcr*(Q1)-I;
clear Q1 Q2;
for i=1:1:length(sq_a)
   A=A+sq_a(i)*Xp1*A;
   A=(I+sq_b(i)*Xp1)\A;
end
```

```
for i=1:1:length(sq_a)
    A=A+sq_b(i)*Xp2*A;
    A=(I+sq_a(i)*Xp2)\A;
End
```

REFERENCES

[1] N. Hairston., "Lithography Aids Integration of Optics," *Laser Focus World*, vol. 37, pp. 93–98, November 2001.

[2] S. E. Miller, "Integrated optics: An introduction," *Bell Syst. Tech. Journal*, vol. 48, pp. 2059-2069, 1969.

[3] H. Kogelnik, "An Introduction to Integrated Optics," *Microwave Theory and Techniques, IEEE Transactions on*, vol. 23, pp. 2-16, 1975.

[4] V. Evtuhov and A. Yariv, "GaAs and GaAlAs Devices for Integrated Optics ." *Microwave Theory and Techniques, IEEE Transactions on*, vol. 23, pp. 44-57, 1975.

[5] J. Farina, "Integrated optics: Theory and technology," *Quantum Electronics, IEEE Journal of*, vol. 19, pp. 770, 1983.

[6] H. A. Jamid and M. N. Akram, "A new higher order finite-difference approximation scheme for the Method of lines," *Journal of Lightwave Technology*, vol. 19, 2001.

[7] W. D. Yang and R. Pregla, "Method of lines for analysis of waveguide structures with multidiscontinuities," *Electronics Letters*, vol. 31, pp. 892, May 1995.

[8] R. Pregla and W. Yang, "Method of lines for analysis of multilayered dielectric wavegides with bragg gratings," *Electronics Letters*, vol. 29, pp. 1962, October 1993.

[9]   S. J. Al-Bader and H. A. Jamid, "Method of lines applied to non-linear guided waves," *Electronics Letters*, vol. 31, pp. 79-85, February 1995.

[10]   J. Gerdes and R. Pregla, "Beam-propagation algorithm based on the Method of lines," *Optical Society of America (B)*, vol. 8, pp. 389-394, Feb. 1991.

[11]   S. J. Al-Bader and H. A. Jamid, "Perfectly matched layer absorbing boundary conditions for the Method of lines modeling scheme," *IEEE Microwave and Guided Waves Letters*, vol. 8, pp. 357-359, November 1998.

[12]   M. N. Akram, "Analysis of anti-resonant reflecting optical waveguide(ARROW) grating using the Method of lines," in *Electrical Engineering*. Dhahran: King Fahd university of petroleum and minerals: Saudi Arabia, April 2000.

[13]   H. A. Jamid and M. N. Akram, "Analysis of Deep Waveguide Gratings: An efficient Cascading and Doubling Algorithm in the Method of Lines Framework," *Journal of Lightwave Technology*, vol. 20, pp. 1204-1208, July 2002.

[14]   E. Ahlers and R. Pregla, "3-D modeling of concatenations of straight and curved waveguides by MOL-BPM," *Optical and Quantum Electronics*, pp. 151-156, 1997.

[15]   W. D. Yang and R. Pregla, "The method of lines for analysis of integrated optical waveguide structures with arbitrary curved interfaces," *Journal of Lightwave Technology*, vol. 14, pp. 879-884, May 1996.

[16] F. H. Al-Harbi, "Implementation of a full vectorial method of lines analysis in the study of metal clad rib waveguide," in *Electrical Engineering*: King Fahd University of Petroleum and Minerals, Saudi Arabia, Dec 2000.

[17] M. Z. M. Khan, "Analysis of one and two diamensional bandgap structures using automated method of lines with arbitrary longitudinal discontinuities," in *Electrical Engineering*. Dhahran: King Fahd University of Petroleum and Minerals, Saudi Arabia, 2004.

[18] F. J. Schmuckle and R. Pregla, "The method of lines for the analysis of lossy planar waveguides," *Microwave Theory and Techniques*, vol. 38, pp. 1473 - 1479, Oct. 1990.

[19] M. Thorburn, A. Biswas, and V. K. Tripathi, "Application of the method of lines to cylindrical inhomogeneous propagation structures," *Electronics Letters*, vol. 26, pp. 170 - 171, Feb. 1990.

[20] A. Dreher, "The method of lines as special moment method," *AFRICON*, vol. 2, pp. 1049 - 1052, Oct. 1999.

[21] R. Pregla and E. Ahlers, "Method of lines for analysis of arbitrarily curved waveguide bends," *Electronics Letters*, vol. 30, pp. 1478 - 1479, Sept. 1994.

[22] A. Barcz, S. F. Helfert, and R. Pregla, "The method of lines applied to numerical simulation of 2D and 3D bandgap structures," *Transparent Optical Networks*, vol. 1, pp. 126 - 129, July 2003.

[23] A. A. Shittu, "Study of periodic waveguides by the finite-difference time-domain method and the Method of Lines," in *Electrical Engineering*: King Fahd University of Petroleum and Minerals, Saudi Arabia, Dhahran 31261, Sep 1994.

[24] K. L. Shlager and J. B. Schneider, "A selective survey of the finite-difference time-domain literature," *Antennas and Propagation Magazine, IEEE*, vol. 37, pp. 39-57, 1995.

[25] S. T. Chu and S. K. Chaudhrui, *Finite-Difference-Time-Domain Methods for Optical Waveguide Analysis*, vol. 11: Elsevier Science Publishing Co., Inc.,, 1995.

[26] S. T. Chu and S. K. Chaudhuri, "A finite-difference time-domain method for the design and analysis of guided-wave optical structures," *Journal of Lightwave Technology*, vol. 7, pp. 2033-2038, Dec. 1989.

[27] S. T. Chu, S. K. Chaudhuri, and W. P. Huang, "Analysis of optical guided-wave devices with the finite-difference time-domain method," *Antennas and Propagation Society International Symposium*, vol. 1, pp. 257 - 260, July 1992.

[28] R. J. Hawkins and R. McLeod, "Finite-difference time-domain simulations of linear integrated photonic devices," *Antennas and Propagation Society International Symposium*, vol. 1, pp. 261, July 1992.

[29] B. Rahman and J. Davies, "Finite-element solution of integrated optical waveguides," *Journal of Lightwave Technology*, vol. 2, pp. 682 - 688, Oct 1984.

[30] J. P. Webb and J. B. Davies, "Finite Element Analysis of Long Optical structures," presented at Electromagnetic Field Computation, 1992. Digest of the Fifth Biennial IEEE Conference on, 1992.

[31] N. Mabaya and P. E. Lagasse, "Finite Element Analysis of Optical Waveguides," presented at Microwave Symposium Digest, 1980 MTT-S International, 1980.

[32] T. P. Young, "Design of integrated optical circuits using finite elements," *Science, Measurement and Technology, IEE Proceedings A*, vol. 135, pp. 135-144, 1988.

[33] Y. Chung and N. Dagli, "An assessment of finite difference beam propagation method," *Quantum Electronics, IEEE Journal of*, vol. 26, pp. 1335-1339, 1990.

[34] H. El-Refaei, D. Yevick, and I. Betty, "Stable and noniterative bidirectional beam propagation method," *IEEE Photonics Technology Letters*, vol. 12, pp. 389-391, April 2000.

[35] R. S. Flamino, A. C. Cesar, and B.-H. V. Borges, "Improved wide-angle finite-difference beam propagation method for the analysis of nonlinear optical waveguides," *Magnetics, IEEE Transactions on*, vol. 38, pp. 589-592, 2002.

[36] L. R. Gomaa, "Beam propagation method applied to a step discontinuity in dielectric planar waveguides," *Microwave Theory and Techniques, IEEE Transactions on*, vol. 36, pp. 791-792, 1988.

[37] J. J. Gribble and J. M. Arnold, "Beam propagation method and geometrical optics," *Optoelectronics [see also IEE Proceedings-Optoelectronics], IEE Proceedings J*, vol. 135, pp. 343-348, 1988.

[38] I. Ilic, R. Scarmozzino, and R. M. Osgood, Jr., "Investigation of the Pade approximant-based wide-angle beam propagation method for accurate modeling of waveguiding circuits," *Lightwave Technology, Journal of*, vol. 14, pp. 2813-2822, 1996.

[39] D. Jimenez and F. Perez-Murano, "Improved boundary conditions for the beam propagation method," *Photonics Technology Letters, IEEE*, vol. 11, pp. 1000-1002, 1999.

[40] I. Kim, P. J. Harshman, and T. K. Gustafson, "The Beam Propagation Method Applied To Nonlinear Optical Microstructures," presented at Nonlinear Optics: Materials, Phenomena and Devices, 1990. Digest. NLO '90., 1990.

[41] Y. Y. Lu and S. H. Wei, "A New Iterative Bidirectional Beam Propagation Method," *IEEE Photonics Technology Letters*, vol. 14, pp. 1533-1535, November 2002.

[42] B. M. Nyman and P. R. Prucnal, "The modified beam propagation method," *Lightwave Technology, Journal of*, vol. 7, pp. 931-936, 1989.

[43] H. Rao, M. J. Steel, R. Scarmozzino, and R. M. Osgood, Jr., "Complex propagators for evanescent waves in bidirectional beam propagation method," *Lightwave Technology, Journal of*, vol. 18, pp. 1155-1160, 2000.

[44] H. Rao, R. Scarmozzino, and J. Richard M. Osgood, Fellow, IEEE, "A bidirectional beam propagation method for multiple dielectric interfaces," *IEEE Photonics Technology Letters*, vol. 11, pp. 830-832, July 1999.

[45] S. Sujecki, T. M. Benson, P. Sewell, and P. C. Kendall, "Efficient 3D-BPM method for semiconductor integrated optics," presented at Transparent Optical Networks, 1999. International Conference on, 1999.

[46] V.Vemuri and W. J. Karplus, "Digital computer treatment of partial differential equations," *Series in Computational Mathematics*, 1981.

[47] J. C. W. Jiang and M. Fontaine, "Analysis of ARROW waveguides," *Optics Communications*, vol. 72, pp. 180-186, July 1989.

[48] Miyagi and Nishida, "A proposal for low loss leaky waveguide for submillimeter waves transmission," *IEEE Trans.*, vol. 28, pp. 398, 1980.

[49] F. A. Milinazzo, C. A. Zala, and G. H. Brooke, "Rational square-root approximations for parabolic equation algorithms," *J. Acoust. Soc. Amer.*, vol. 101, pp. 760-766, Feb. 1997.

[50] Y.-P. Chiou and H.-C. Chang, "Analysis of optical waveguide discontinuities using the Pade approximants," *Photonics Technology Letters, IEEE*, vol. 9, pp. 964-966, 1997.

[51] J. Fang and Z. Wu, "Generalized perfectly matched layer-an extension of Berenger's perfectly matched layer boundary condition," *Microwave and Guided Wave Letters, IEEE [see also IEEE Microwave and Wireless Components Letters]*, vol. 5, pp. 451-453, 1995.

[52] H. A. Jamid, "Frequency-Domain PML layer based on the complex mapping of space boundary condition treatment," *IEEE Microwave and Guided Wave Letters*, vol. 10, pp. 356-358, Sep. 2000.

[53] A. T. de Hoop, P. M. van den Berg, and R. F. Remis, "Absorbing boundary conditions and perfectly matched layers - an analytic time-domain performance analysis," *Magnetics, IEEE Transactions on*, vol. 38, pp. 657-660, 2002.

[54] H. A. Jamid, "Enhanced PML Performance Using Higher Order Approximation," *IEEE Transactions on Microwave Theory and Techniques*, vol. 52, pp. 1-9, April 2004.

[55] H. A. Jamid, "Generalized finite-difference higher order approach for the solution of the wave equation," *Personal Notes*.

[56] A. A. Shittu, S. Al-Bader, and H. Jamid, "Mode Reflectivity of Finitely-Periodic Dielectric Waveguides," *Optics Communications*, vol. 114, pp. 242-246, September 1994.

[57] Y. P. Chiou and H. C. Chang, "Analysis of optical waveguide discontinuities using Padé approximation," *IEEE Photonics Technology Letters*, vol. 9, pp. 964-966, July 1997.

[58] J. George A. Baker, "Essentials of Padé approximants." New York: Academic Press, 1975.

[59] J. Yamauchi, Y. Akimoto, M. Nibe, and H. Nakano, "Wide-angle propagating beam analysis for circularly symmetric waveguides: comparison between FD-BPM and FD-TDM," *Photonics Technology Letters, IEEE*, vol. 8, pp. 236-238, 1996.

[60] P. L. Ho and Y. Y. Lu, "A stable bidirectional propagation method based on scattering operators," *IEEE Photonics Technology Letters*, vol. 13, pp. 1316-1318, December 2001.

[61] S. H. Wei and Y. Y. Lu, "Application of Bi-CGSTAB to Waveguide Discontinuity Problems," *IEEE Photonics Technology Letters*, vol. 14, pp. 645-647, May 2002.

[62] C. Manolatou, S. G. Johnson, S. Fan, P. R. Villeneuve, H. A. Haus, and J. D. Joannopoulos, "High-Density Integrated Optics," *Journal of Lightwave Technology*, vol. 17, pp. 1682-1692, September 1999.

[63] S. G. Johnson, C. Manolatou, S. Fan, P. R. Villeneuve, J. D. Joannopoulos, and W. A. Haus, "Elimination of crosstalk in waveguide intersections," *Optics Letters*, vol. 25, no. 25, pp. 1855-1857, Dec 1998.

VITA

Mohammed Ameeruddin

❖ Born on 11-11-1980 in Hyderabad, India.

❖ 2002-2004 M.S. in Electrical Engineering with specialization in Communication Systems at King Fahd University of Petroleum and Minerals, Dhahran, KSA.

    o Full Fee Waiver.

    o Held Research Assistantship during the period of study.

    o GPA 3.65/4.0.

❖ 2001-2002 Database Administrator (Oracle 8i), Kedia Infotech Ltd. Hyderabad, India.

❖ 1997-2001 B.E. Electronics and Communications Engineering at Osmania University, Hyderabad, India.

    o First Division with Distinction.

❖ Distinction in Intermediate (Class 12), Shadan Junior College, Hyderabad, India.

❖ Distinction in Class 10, Bright High School, Hyderabad, India.

❖ Diverse knowledge of Telecommunication Systems.

❖ Oracle Certified Professional (Database Administration).

❖ Windows Administration and Networking.

❖ Quick Learner, Oral, interpersonal, and teamwork skills.